Investigation of Primary Blast Injury and Protection using Sagittal and Transverse Finite Element Head Models

by: Dilaver Singh

A thesis
presented to the University of Waterloo
in fulfillment of the
thesis requirement for the degree of

Master of Applied Science

in

Mechanical Engineering

Waterloo, Ontario, Canada, 2015

Author's Declaration

I hereby declare that I am the sole author of this thesis. This is a true copy of the thesis, including any required final revisions, as accepted by my examiners

I understand that my thesis may be made electronically available to the public.

Abstract

The prevalence of blast related mild traumatic brain injury (mTBI) in recent military conflicts, attributed in part to an increased exposure to improvised explosive devices (IEDs), requires further understanding to develop methods to mitigate the effects of primary blast exposure. Although general blast injury has been studied extensively since the 1950's, many aspects of mTBI remain unclear, including specific injury mechanisms and injury criteria. The purpose of this work was to develop finite element models to investigate primary blast injury to the head in the loading regimes relevant to mTBI, to use the models to determine the response of the brain tissue, and ultimately to investigate the effectiveness of helmets on response mitigation.

Since blast is inherently a wave dominated phenomena, finite element models require relatively small elements to resolve complex pressure wave transmission and reflections in order to accurately predict tissue response. Furthermore, mesh continuity between the tissue structures is necessary to ensure accurate wave transmission. The computational limitations present in analyzing a full three dimensional blast head model led to the development of sagittal and transverse planar models, which provide a fully coupled analysis with the required mesh resolution while remaining computationally feasible. The models consist of a single layer of solid hexahedral elements, and include all of the relevant tissues in the head including the skin, muscle, skull, cerebrospinal fluid, and brain.

The sagittal and transverse models were validated using head kinematics against experimental data on Hybrid III head-forms exposed to free-field blast. The peak head accelerations of the models was in close agreement to the experimental data, and the HIC_{15} predictions were in reasonable

agreement. In addition, the models were validated for intracranial pressure using experimental data from cadaveric heads exposed to shock tube loading. The intracranial pressures predicted by the sagittal and transverse models was in good agreement at the frontal, temporal, and parietal locations, and in fair agreement at the occipital location. A simplified three dimensional ellipsoid study was undertaken to verify that sagittal and transverse planar models are capable of representing a three dimensional shape. This investigation confirmed that the pressures predicted by the planar models are accurate at the frontal, temporal, and parietal locations, although underpredicted at the occipital location due to three dimensional wave superposition that becomes significant at the occipital region.

The sagittal and transverse models were run at three representative blast load cases, corresponding to 5 kg of C4 at 3, 3.5, and 4 m standoff distances, and the resulting intracranial strains and pressures were investigated. The sagittal and transverse models report peak principal strains of 0.035 – 0.062 and 0.053 – 0.087 respectively. In comparison to the available threshold values of principal strain in the literature, the strains predicted by the models are generally low. While the strains reported by the models in primary blast are small, the strain rates are significantly greater (ranging from 226 – 571 s^{-1}) than those seen in typical automotive or blunt impact scenarios. Furthermore, the models report that significant levels of intracranial pressure, on the order of several atmospheres, can be generated in the brain tissue during primary blast exposure. The peak pressures in the brain tissue for both models typically exceeded the existing injury thresholds for intracranial that are available in the literature. However, these existing criteria were generally developed for automotive crash scenarios, so may not be suitable for the short durations inherent to blast. The magnitudes of intracranial pressure increased significantly with increasing blast load severity, while changes in principal strain were relatively small, and peak strains were low in all

three load cases, suggesting that pressure may be a more appropriate injury response metric for blast injury.

The sagittal and transverse models were outfitted with various military helmet configurations and materials to investigate the influence of helmet visors, foam lining presence and density, and Kevlar material stiffness on the protective properties of the helmet. The peak head accelerations and intracranial pressures were compared for low and high intensity blast loads. In general, the presence of a helmet resulted in reduced peak head accelerations, and a greater reduction was reported with the addition of a half-visor and full-visor. The presence of a visor significantly reduced positive intracranial pressures in all cases, although increased the maximum negative pressures in some cases. The effects of the foam lining material was not as significant to the model response as the helmet visor configurations, but in general, a lower density foam provided better load mitigation. In cases where there was no foam lining, pressure wave reflections in the air gap between the helmet and head were found to cause greater intracranial pressures in adjacent brain tissue, although the magnitudes of these increased pressures were generally lower than the incident compressive pressures caused by the initial wave impact.

Acknowledgements

I would like to foremost acknowledge the help and guidance of my supervisor, Duane Cronin. I feel very fortunate to have worked with such a great engineer and person.

I would also like to acknowledge the support of Amal Bouamoul at DRDC Valcartier, and Jean-Philippe Dionne at Med-Eng, for their invaluable assistance on this project.

Finally, I would like to thank my friends and family, especially my parents, to whom I dedicate this work.

Table of Contents

List of Figures

List of Tables

1. Introduction

In the field of impact biomechanics, the highest objective is surely the prevention and protection of the human body from injury. It is ultimately for this purpose that the work presented herein is dedicated. Specifically, this work uses numerical models to investigate the nature of blast loading to the human head and response of the brain, and potential mitigation strategies that reduce the effects of such loading.

In recent conflicts, there has been a marked increase in the amount of injuries caused by non-lethal exposure to blast events. This is due in part to the increased use of improvised explosive devices (IEDs) in these conflicts. The US Joint Theater Trauma Registry reported that IEDs were the cause of approximately 80% of casualties from 2001 to 2005 [Owens et al. 2008]. Furthermore, reviews of US Army casualties in Iraq and Afghanistan have found that between 52 – 63% of traumatic brain injury (TBI) cases were a result of exposure to explosive detonations [Galarneau et al. 2008, Wojcik et al. 2010]. And various studies have reported that between 19 – 22% of returning service personnel have been diagnosed with TBI [Tanielian 2008, Connoly 2010, Terrio et al. 2009], underscoring the prevalence of this type of injury. The implications of these statistics are that improved protection against blast related TBI is needed.

The increased number of blast-related injuries to the head are due in part to recent advances in ballistic protection to the head and torso, which allow soldiers to survive injurious situations that previously may have been life-threatening. One of the characteristics of TBI caused by blast is often the lack of penetrating wounds or noticeable trauma to the head. This is known as mild traumatic brain injury (mTBI), and is hypothesized to be caused by the interaction of the blast shock wave with the brain, which causes subtle injuries to the tissues.

There are four general categorizations of blast injury. Primary blast injury is defined as any injury that is a result of the direct interaction of the blast pressure wave with the body. Primary blast injury typically manifests in the air containing organs such as the lungs, gastrointestinal tract, and inner ear, as has recently been linked to brain injury. Secondary blast injuries are caused by impact from fragmentation and debris propelled by the blast. Tertiary blast injuries are due to the impact of the body itself with the ground or surrounding walls, and quaternary injuries are any other injuries caused by the blast including but not limited to burning, blindness, and smoke inhalation. Of these four types of injury, primary blast injury is most unique to blast loads, as it is directly caused by the blast pressure wave, and not by traditional ballistic or blunt impact injury mechanisms as in secondary or tertiary blast injuries.

Finite element modeling, which uses discretized elements to model complex geometries and loading conditions, has been used extensively in recent decades to simulate real world environments and situations in an effort to better understand a particular problem. In applications that are challenging to investigate experimentally, such as blast injury, numerical models can be of great use. The purpose of the current work was to develop finite element models to model primary blast injury to the head in the loading regimes relevant to mTBI, to use the models to determine the resulting loading to the brain tissue, and ultimately to investigate the effectiveness of helmets on load mitigation.

The following chapters provide a background review of the important subjects in understanding primary blast injury and finite element modeling. This includes the physics of blast, relevant anatomy, mechanisms of injury relevant to blast injury, a brief history of helmet protection, and existing models and modeling techniques. Once the background knowledge is established, the

finite element methodology and model development are discussed. The results of the models are separated in terms of general brain tissue response to primary blast, and the effects of helmet protection. Finally, the results are discussed in detail, and conclusions and recommendations are provided.

2. Review of Blast Physics

This chapter will focus on the physics of a pressure wave resulting from an explosive detonation, as that is the phenomenon responsible for primary blast injury. The detonation itself will be briefly explained. Some ground and structure interaction will be discussed, but the emphasis will be on free field blast, the focus of the current study.

2.1 Blast Characterization

A blast wave occurs when an explosive material is detonated and rapidly releases energy in the form of light, heat, sound, and pressure. Explosive materials are characterized by their high potential energy, which can be chemical or nuclear in nature [Smith & Hetherington 1994]. Explosions can be divided into three groups: physical, nuclear, or chemical events. Physical explosions are generally any explosions that are not caused by nuclear or chemical reactions, these include volcanic eruptions or catastrophic failure of pressurized structures. Nuclear explosions are caused by the release of energy from the formation of different atomic nuclei by the redistribution of protons and neutrons in the reacting atomic nuclei. Nuclear explosions can result from splitting heavy atoms into lighter ones (fission), or by joining lighter atoms into heavier ones (fusion). Nuclear explosions utilize the extremely strong subatomic forces that hold atoms together, rather than the interatomic forces associated with conventional or chemical reactions. Nuclear explosions are not considered in detail in this study, as the primary source of mTBI is through exposure to the relatively small explosions caused by chemical explosions, such as those experienced from the detonation of IEDs. [Smith & Hetherington 1994]

A chemical explosion is caused by the rapid oxidation of an explosive compound. No air is

necessary, since the compound contains the oxygen needed to sustain the reaction. Explosive compounds are generally condensed into solids or liquids, to speed up the reaction rate, and for practicality. When the reaction occurs, the solid or liquid explosive is decomposed rapidly into highly pressurized gases, which expand into the surrounding medium producing shock waves in the surrounding solid, fluid, or gas. For explosive materials, if the velocity of detonation is lower than the speed of sound in the material, the process is called deflagration. If the velocity of detonation is faster than the speed of sound, it is called detonation. High explosives are characterized by their ability to undergo rapid detonation, which occurs for common explosives such as TNT and C4 [Kingery 1984]. The detonation velocity is generally between 1500 – 9000 m/s. In blast physics, TNT is widely used as a reference explosive, and other explosive materials are analyzed by using a TNT equivalence factor, which is the ratio of specific energies for the desired explosive material to TNT. For example, the TNT equivalence factor for C4 is 1.34 for converting pressures. [Smith & Hetherington 1994]

The detonation of a high explosive is typically initiated by a detonator at a single point within the explosive, where the explosive compound begins to react. The chemical reaction propagates spherically from this point at the detonation wave speed, and rapidly converts the solid or liquid explosive material into a highly pressured, high temperature gas. The detonation of a high explosive results in a fireball comprising the combustion products and preceded by a blast pressure wave in the surrounding medium.

The pressures resulting from blast events are generally measured in two different ways: static pressure and dynamic pressure. Static pressure, also called incident or side-on pressure, is the pressure that would be experienced by a particle moving within the blast flow at the same velocity

of the blast flow, and is commonly used in experimental testing as a reference. Dynamic pressure includes the static pressure and describes the interaction of the gas with a structure, and therefore also depends on the size, shape, and compliance of the structure. Dynamic pressure is also called reflected pressure. [Bulson 1997]

2.2 Fundamental Blast Physics in Air

For the purposes of the current study, the physics of the blast wave after the explosive charge has been detonated in free air is of particular interest. After detonation occurs, the resulting high pressure and high temperature gases expand rapidly into the surrounding air, and force the air to be displaced and compressed. Since air is a compressible material, the acoustic wave speed in the pre-compressed air behind the wavefront will increase, allowing succeeding waves to travel faster through it, and 'catch up' with the wavefront. This creates a layer of compressed air at the blast wavefront in front of the expansion gases, which is known as the blast pressure wave, or shock wave. As the reaction gases expand further, they eventually reach atmospheric pressure, and finally their pressure falls slightly below atmospheric pressure, caused by the momentum of the gaseous molecules. This creates a small negative pressure zone later in time, which results in a negative pressure phase in the blast wave. As the expansion gases and air is pushed away from the detonation point, the air pressure returns to equilibrium. [Smith & Hetherington 1994]

A blast wave in free air is typically described by pressure as a function of time using the Friedlander equation (Equation 2.1) [Smith & Hetherington 1994].

Friedlander equation $$p = p_0(1 - {}^{t}/_{t_o})e^{-kt/t_o}$$ *Equation 2.1*

where p_o is the ambient pressure, t_o is the time at which the positive phase duration begins, and k is an experimental constant called the waveform parameter that describes the rate of decrease of pressure following the peak overpressure.

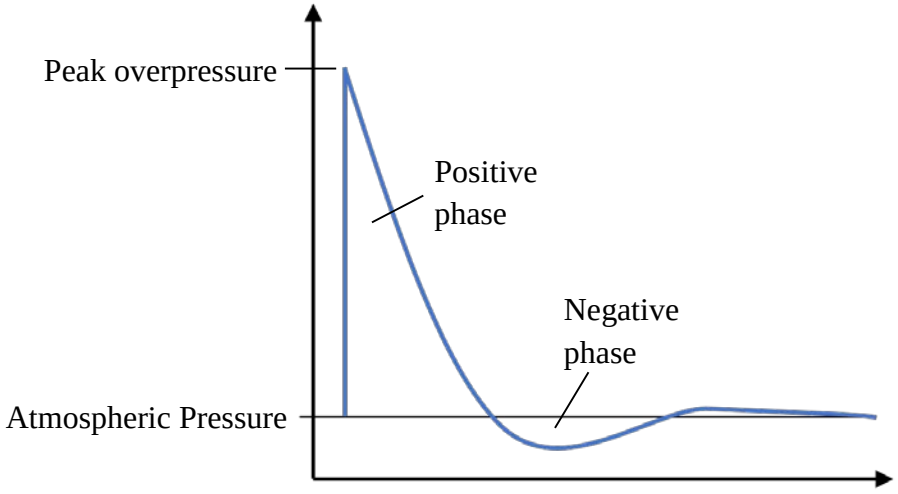

Figure 2.1: Typical Friedlander curve

The idealized blast waveform pictured above (Figure 2.1) using the Friedlander equation is characterized by an instantaneous increase in pressure representing the blast shock front. This is followed by an exponentially decaying curve with a negative pressure phase where the pressure falls below the ambient pressure. This is essentially an idealized version of an actual blast wave in free air and neglects interactions with the ground or other objects. Some important parameters of a blast wave are the peak overpressure, the arrival time, the positive phase duration, and the impulse. The impulse is the area under the pressure-time curve, and is an important parameter related to the momentum of the wave.

Generally, blast wave overpressures can be scaled with a cube root scaling law based on the mass of the explosive (Equation 2.2) [Smith & Hetherington 1994].

Blast overpressure scaling law $$\frac{R_1}{R_3} = \left(\frac{W_1}{W_2}\right)^{1/3}$$ *Equation 2.2*

where R_1 is the range at which an overpressure is generated by charge mass W_1, and R_2 is the range at which the same overpressure is generated by charge mass W_2. However, the reflected pressure cannot be scaled with this method, because reflected pressures are dependent on the interaction of the blast wave with a structure and the resulting wave reflections, which depend on the strength of the incident wave. [Smith & Hetherington 1994]

Rankine and Hugoniot developed equations for normal shocks in ideal gases (Equations 2.3 - 2.5) [Smith & Hetherington 1994].

Blast wavefront velocity $$U_s = \sqrt{\frac{6p_s + 7p_o}{7p_o}}\, a_o$$ *Equation 2.3*

Air density behind wavefront $$\rho_s = \frac{6p_s + 7p_o}{p_s + 7p_o}\rho_o$$ *Equation 2.4*

Maximum dynamic pressure $$q_s = \frac{5{p_s}^2}{2(p_s + 7p_o)}$$ *Equation 2.5*

where U_s is blast wavefront velocity, p_s is peak static overpressure, p_o is the ambient air pressure, and a_o is the speed of sound in air at ambient pressure. Looking at Equations 2.3 and 2.4, it is clear that as the peak static overpressure increases, both the blast wavefront velocity and the air density behind the wavefront increase. Thus, as the charge size of the explosive increases, the resultant blast wave will be both faster and have a more intense shock front. Brode developed equations

that predict the peak static overpressure in the near field where static pressure is greater than 10 bar, and in the medium or far field where the static pressure is between 0.1 and 10 bar (Equation 2.6). [Smith & Hetherington 1994]

Peak static overpressure

$$p_s = \frac{6.7}{Z^3} + 1\ bar\ (p_s > 10\ bar)$$

$$p_s = \frac{0.975}{Z} + \frac{1.455}{Z^2} + \frac{5.85}{Z^3} - 0.019\ bar\ (0.1 <\ p_s < 10\ bar) \qquad \textit{Equation 2.6}$$

$$Z = R/W^{1/3}$$

where *R* is the distance from the charge centre in metres and *W* is the charge mass in kg of TNT. Other equations also exist to describe these relationships, such as the Henrych equations below (Equation 2.7). [Smith & Hetherington 1994]

$$p_s = \frac{14.072}{Z} + \frac{5.540}{Z^2} + \frac{0.357}{Z^3} + \frac{0.00625}{Z^4}\ bar \qquad (0.05 \le Z < 0.3)$$

$$p_s = \frac{6.194}{Z} + \frac{0.326}{Z^2} + \frac{2.132}{Z^3}\ bar \qquad (0.3 \le Z < 1) \qquad \textit{Equation 2.7}$$

$$p_s = \frac{0.662}{Z} + \frac{4.05}{Z^2} + \frac{3.288}{Z^3}\ bar \qquad (1 \le Z < 10)$$

The accuracy of these free-field equations is generally greater in the mid to far field, likely because of the complexity of the physics in the near field, where there may be interactions from the fireball and reaction gases that affect the pressures.

The pressure in a shock wave can also be converted to temperature and specific volume through the Rankine-Hugoniot relations for air (Equations 2.8 – 2.9). [Needham 2009] These relationships

are important in numerical modeling of blast waves because many finite element codes can use internal energy (temperature) and specific volume as boundary conditions as a method of modeling a blast pressure wave numerically.

Temperature $$T = T_{atm}\left(\frac{7+\frac{P-P_{atm}}{P_{atm}}}{7+6\frac{P-P_{atm}}{P_{atm}}}\right)\left(1+\frac{P-P_{atm}}{P_{atm}}\right)$$ *Equation 2.8*

Specific Volume $$v = v_{atm}\left(\frac{7+\frac{P-P_{atm}}{P_{atm}}}{7+6\frac{P-P_{atm}}{P_{atm}}}\right)$$ *Equation 2.9*

2.3 Blast Wave Interaction

When a blast wave interacts with a solid structure, the wave will reflect off the surface, and the compressed air in the wave will become further compressed by the remainder of the incoming wave. This creates a region of higher pressure near the structure, called the reflected pressure. For an infinitely large rigid wall in air, the reflected pressure can be described by Equation 2.10. [Smith & Hetherington 1994]

Reflected Pressure $$p_r = 2p_s\left[\frac{7p_o+4p_s}{7p_o+p_s}\right]$$ *Equation 2.10*

where p_r is the reflected pressure, p_s is the static overpressure, and p_o is the atmospheric pressure. From Equation 2.10, the reflected pressure depends nonlinearly on the strength of the incident pressure (p_s), so reflected pressures cannot be scaled directly with static overpressures. Typically,

the ratio of reflected pressure to static pressure is between 2 and 8. [Smith & Hetherington 1994]

Blast waves can also diffract around structures, if the structure has a geometry such that the incoming blast wave area is larger than the exposed area of the structure. This is important in blast injury to the human head, where the wave has the potential to wrap around the curvature of the head and create high pressure zones at the posterior of the head through wave superposition. It is also important to consider the stress wave reflections in materials. When a blast wave reaches a structure, it creates a compressive stress wave in the material of the structure, which generally propagates at the acoustic wave speed of the material. Contrary to popular terminology, solid materials that are impacted by blast waves generally do not experience shock, as the pressures required to induce shock waves in solid materials are very large. The compressive stress waves caused by the blast impact can also undergo reflections and transmissions in the structure material where the density or geometry changes. These relationships are expressed in Equations 2.11 and 2.12.

Transmitted wave $$\frac{\sigma_T}{\sigma_I} = \frac{2\rho_1 c_1}{\rho_1 c_1 + \rho_2 c_2}$$ *Equation 2.11*

Reflected wave $$\frac{\sigma_R}{\sigma_I} = \frac{\rho_1 c_1 - \rho_2 c_2}{\rho_1 c_1 + \rho_2 c_2}$$ *Equation 2.12*

where σ_T is the transmitted stress, σ_I is the incident stress, σ_R is the reflected stress, ρ_1 and c_1 are the density and elastic wave speed in material 1, and ρ_2 and c_2 are the density and elastic wave speed in material 2. The product of density and elastic wave speed is called the characteristic acoustic impedance, which is the material property that governs wave reflection and transmission.

Acoustic impedance is essentially a measure of the resistance of a material to carrying an elastic wave.

From the equations of wave reflection and transmission, the behaviour of a stress wave through an interface is different depending on the relative impedance mismatch of the materials. When a wave travels from a high impedance to a low impedance material, it reflects in the opposite mode (i.e. a compressive wave will reflect in tension), and transmits in the same mode. When a wave travels from a low impedance to a high impedance material, it both reflects and transmits in the same mode. This has important implications to blast wave phenomena, where these principles of wave transmission behaviour should guide the analysis of a blast wave interacting with the head.

2.3.1: Ground Interaction

Whereas free air detonations consider the blast wave to propagate spherically from the charge centre, surface detonations must consider the interaction with the ground. If the ground was assumed to be a perfect reflector of energy, then theoretically a surface detonation would produce a blast wave with 2 times the energy of an equally sized free air detonation. In practice however, this enhancement factor is generally 1.8 or less [Smith & Hetherington 1994]. The height of detonation, or height of burst, is defined as the height of the charge mass centre from the ground. In the current work, the simulated blast waves are assumed to be free air detonations, and ground interaction is not considered, but has been evaluated in other related research [Haladuick et al. 2012].

Another important phenomenon that occurs in near surface blasts is the Mach stem. This is when the incident blast wave reflects off the ground and, since it is travelling through previously

compressed air with a higher acoustic wave speed, catches up with the incident wavefront (Figure 2.2). This creates a region of higher pressures where the reflected and incident waves interact. Mach stems can also be created by explosions inside structures, where the presence of walls creates the potential for various reflections.

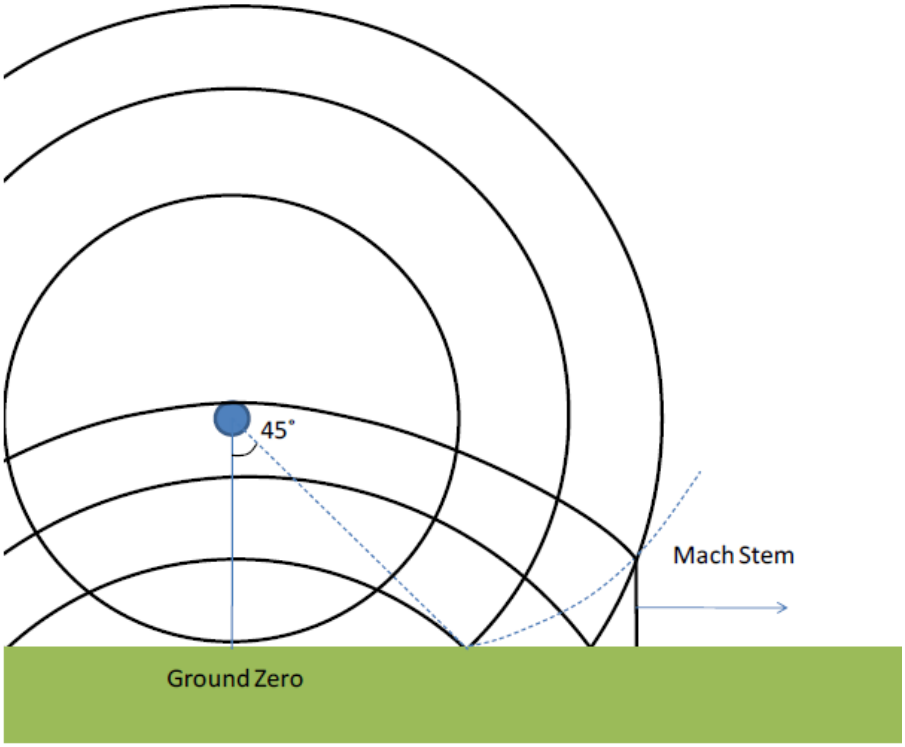

Figure 2.2: Mach stem effect in surface blast with ground reflection (adapted from Thom 2009)

The interaction of blast waves with the ground as well as structures in the real world creates deviations in actual blast waves from the theoretical curve. These deviations produce 'complex' blast waves, which are not easily characterized mathematically, and are dependent on variables such as the presence of walls or other obstacles that interfere with the wave propagation. Real world blast waves that do not interact significantly with external structures are called 'simple' blast waves, and are shaped similar to the idealized Friedlander curve (Figure 2.3).

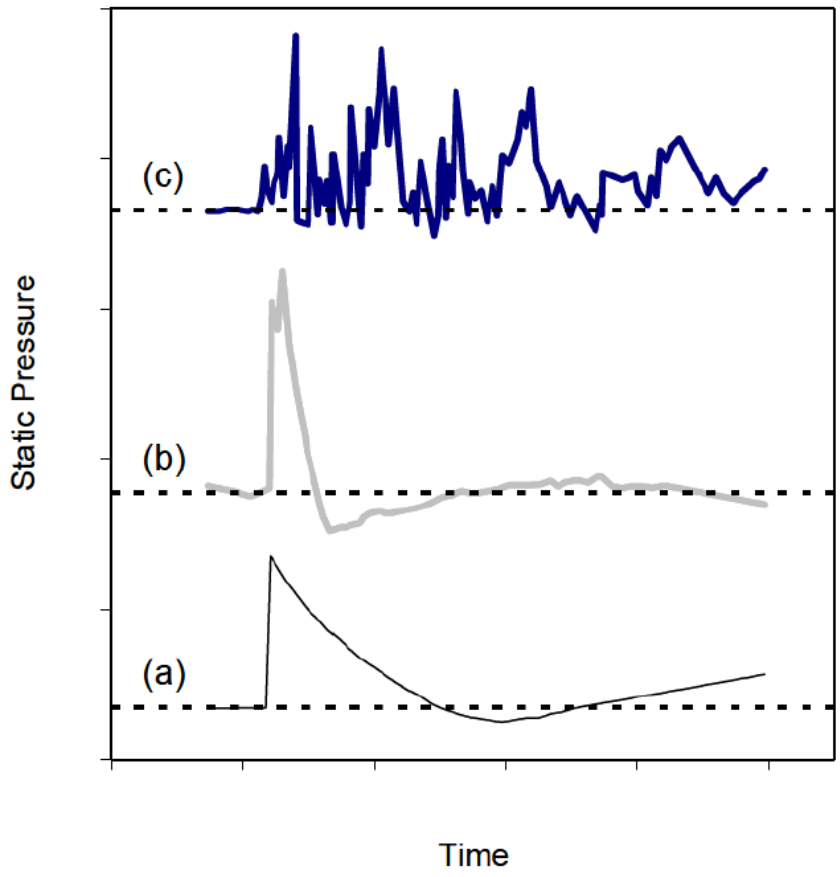

Figure 2.3: Pressure time profiles of (a) idealized (Friedlander) wave, (b) simple blast wave, and (c) complex blast wave (adapted from Thom 2009)

Blast events can be broadly categorized by static overpressure into three ranges, called the near, mid, and far fields (Figure 2.4). The near field, where the static overpressure is typically greater than 10 atm, is close enough to the blast centre to result in severe or immediately life-threatening injuries, including effects from the fireball of the explosion. The mid field, where the static overpressure is typically between 0.1 and 10 atm, is far enough away to escape the immediate and severe injuries in the near field, but still results in exposure to a significant blast pressure wave. And the far field, with static overpressures less than 0.1 atm, is far enough away from the blast centre to escape any primary effects of the blast, where the most significant threat is from fragmentation propelled by the blast event. The typical injuries seen in each of these ranges are

summarized in Table 2.1. In investigating mild Traumatic Brain Injury, the mid field regime of loading is most relevant, where the primary effects of the blast pressure wave are most prominent.

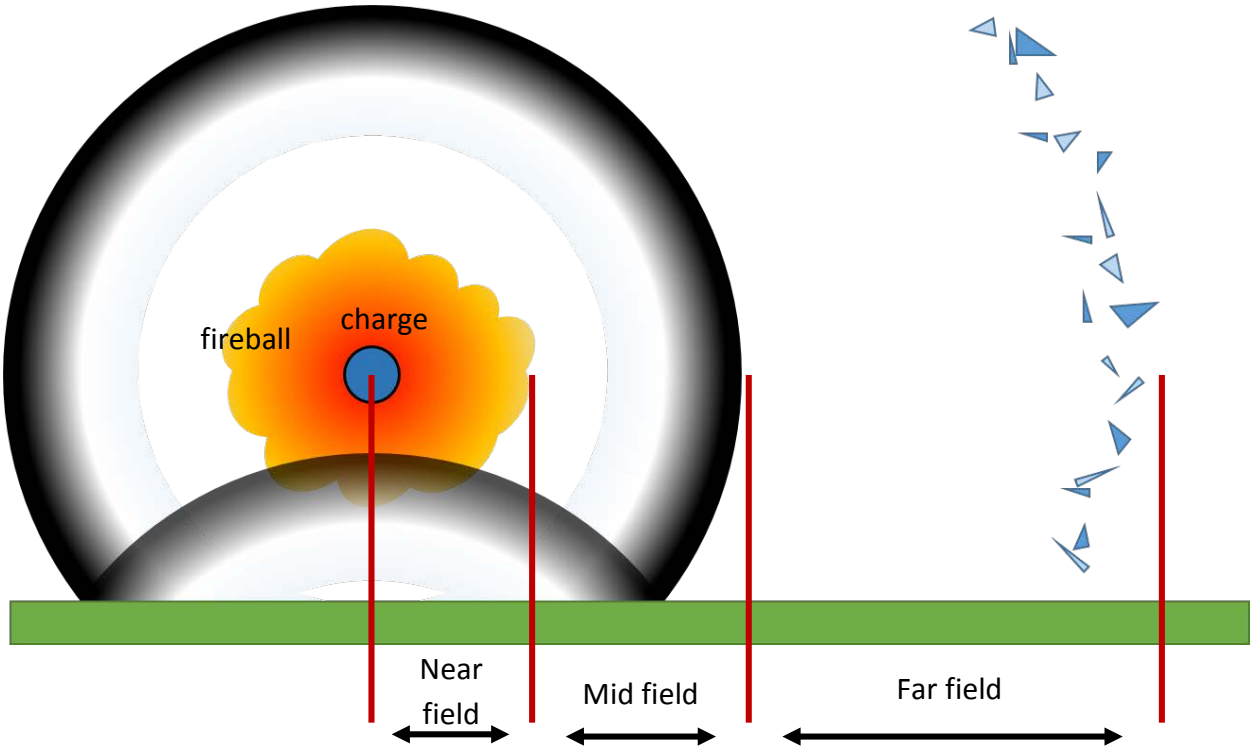

Figure 2.4: Schematic of regimes of loading in blast exposure

Table 2.1: Typical injuries seen in blast exposure for different ranges of standoff (adapted from Wightman 2001)

Injury Type	Distance relative to explosive							
	Near	→						Far
Total body disruption	X							
Burns and inhalation injury	X	X						
Toxic inhalations	X	X	X					
Traumatic amputation	X	X	X	X				
PBI of the lungs and bowels	X	X	X	X	X			
Tertiary blast injury	X	X	X	X	X	X		
Ear drum rupture	X	X	X	X	X	X	X	
Fragmentation injury	X	X	X	X	X	X	X	X

3. Review of Head and Brain Anatomy

In order to understand the potential injury mechanisms, the pathophysiology of blast head injury, and to make informed conclusions about injury criteria, a sound understanding of the relevant anatomy is essential. This chapter describes the anatomy of the structures of the human head, focusing on the brain. The basic biological functions of the tissues will be covered, as well as the physical properties.

3.1 Basic Head Anatomy

In addition to containing the primary sensory organs (eyes, ears, nose, and mouth), the human head is the home of the core of the central nervous system, the brain. The brain is contained within the skull, which is itself surrounded by the soft tissues that make up the head, including the scalp and facial muscles. The head is joined to the body through the neck, which contains the cervical vertebrae, and numerous ligaments, muscles, and connective tissues to control the movement of the head and protect the spinal cord. The mass of an adult human head varies from 4 – 5 kg, or approximately 8% of the total mass of the body, although this varies depending on body types [Gekhman 2006].

The skull is the structural foundation of the head, and has been shaped by natural selection to protect the brain from mild impacts. The thickness of the skull varies according to age, gender, region of the skull, and genetic variables. Skull thicknesses of adult human males have been measured to be between 3.9 – 9.61 mm in various studies, depending on individual and the measurement location [Mahinda 2009, Ruan 2001]. The portion of the skull that surrounds the

brain is made up of several thin curved bones that fuse together during childhood creating interfaces called sutures (Figure 3.1). Although skull sutures can allow a small amount of movement in adolescence, they typically harden to relative rigidity in middle age, and contribute minimally to the structural integrity of the skull. The skin that surrounds the skull is referred to as the scalp. The scalp thickness is typically 5 – 7 mm, although again, this varies depending on age, gender, location, and genetic variables [Parsons 1929, Hori et al. 1972].

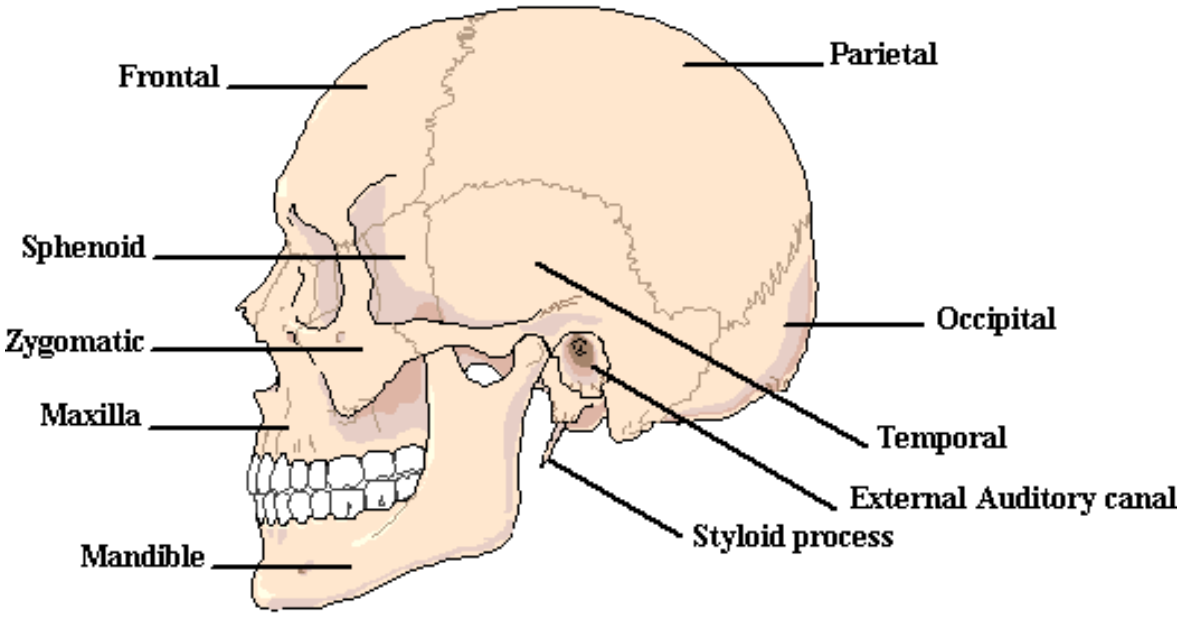

Figure 3.1: Human Skull Bones [Wollaston]

The geometrical planes of the head are commonly defined using a convention called the Frankfurt reference coordinate plane convention (Figure 3.2). In the Frankfurt reference plane coordinate system, the sagittal plane is defined normal to the side view of body, the transverse plane normal to the top view, and coronal plane normal to the front view. For the sake of consistency, this is the convention that will be used throughout this work.

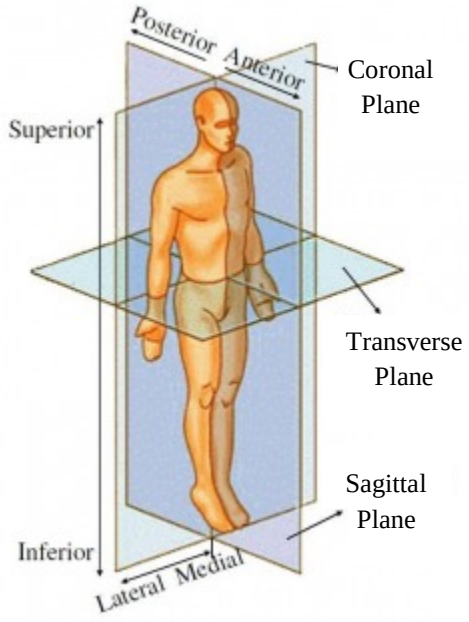

Figure 3.2: Frankfurt reference planes [Saikat 2008]

3.2 Brain Anatomy

The brain is the control centre of the central nervous system, and one of the vital organs of the human body. A typical adult human brain has a mass of approximately 1350 – 1500 g for males, and slightly less for females [Nelson 1982, Hartmann et al. 1994]. The brain regulates numerous bodily functions, controls the release of chemicals and hormones throughout the body, controls the sensory functions of the body, and contains the mind and personality of the person. Although many aspects of the nature and function of the brain remain mysterious, significant strides have been made in recent years, and continue to be made, to improve our understanding.

3.2.1 Cellular Makeup of the Brain

The brain is primarily composed of two types of cells - neurons, and neuroglia, as well as containing blood vessels throughout. Neurons serve the primary function of the brain by transmitting electrochemical signals to connected cells, while the neuroglia provide supporting functions including maintenance of neurons. Neurons are highly specialized cells that are able to form complex networks with surrounding neurons and tissues, and transmit information through electrochemical pathways. A typical neuron is composed of the cell body (also called the soma), dendrites, and an axon (Figure 3.3). The neuronal cell body contains the nucleus, mitochondria, ribosomes, and various other intracellular components.

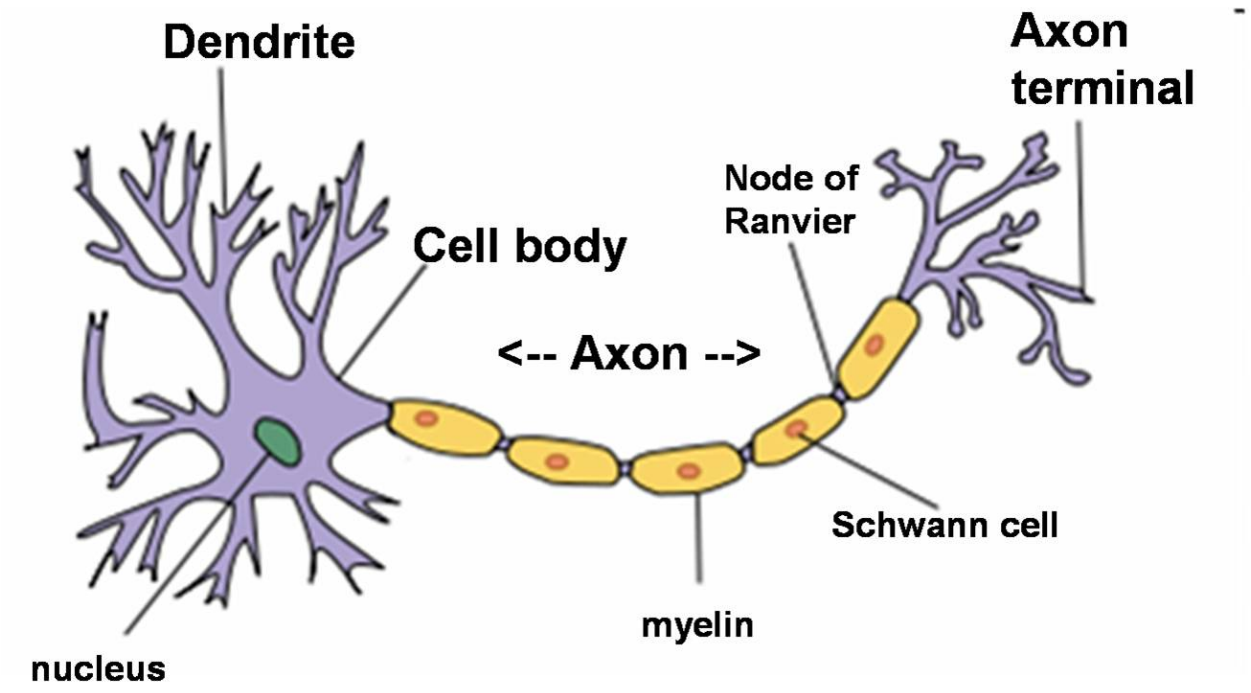

Figure 3.3: Schematic of Neuron [Creative Commons]

The dendrites that surround the cell body can extend up to hundreds of micrometres, and generally form a great number of branches, forming what is called the dendritic tree. The network of dendrites on a neuron acts as a field of receptors for surrounding neurons to attach to and communicate with. The axon is a part of a neuron that extends far past the cell body, up to 1 metre in humans and more in other species. Axons are covered in a substance called myelin which protects and speeds up the electrical signals. Each neuronal cell body can create only one axon, although axons can branch many times outside of the cell body. The end of an axon is called the axon terminal, which is made up of synaptic vesicles that can connect to dendrites on other neurons or cells and form electrochemical connections, called synapses. [Hole 1984]

A neuron can have many dendrites, but no more than one axon. Furthermore, some neurons have no dendrites and others have no axon. Neurons communicate through voltage gradients driven by ion exchange, which can send electrical signals across the axons, in a process called neurotransmission or synaptic transmission. There are three types of neurons: sensory neurons which transmit and process information from the sensory organs, motor neurons which send and receive signals to activate muscles, and interneurons which make up the majority of the neuronal mass and form the fundamental neural networks in the brain and spinal cord. In humans, neurons have an average of 7000 synaptic connections, and there are approximately 10^{11} neurons in the brain. Neurons do not undergo cell division in the typical manner; they are typically formed by certain stem cells. [McKinley 2008]

In addition to the neurons themselves, brain tissue is also composed of neuroglia, or glial cells. Neuroglia outnumber neurons by five to ten times in total, and make up approximately half of the volume of the brain. These are non-neuronal cells that provide support and maintenance to

the neurons in the brain. There are four main functions of neuroglia. Firstly, to provide structural support and hold the neurons in place within the brain. Secondly, to provide neurons with nutrients and oxygen. Thirdly, to separate neurons from each other. And fourthly, to eliminate harmful pathogens and dispose of dead neurons. Neuroglia can also assist neurons in the formation of synaptic connections in certain cases [McKinley 2008]. There are many types of neuroglial cells that, combined, provide these functions, the specifics of which are not detailed in this work. Brain tissue is commonly referred to as either grey matter or white matter, depending on the cell type that comprises the tissue. Grey matter is generally composed of neuronal cell nuclei, while white matter is predominantly axons and neuroglia.

3.2.2 Sections of the Brain

The brain is divided into two main parts, the cerebrum and the cerebellum. The cerebrum, or the cerebral cortex, is the largest part of the brain, typically associated with higher brain function including thinking and problem solving. The cerebrum is divided in several sections, generally called lobes which are named after the bones of the skull to which they are adjacent. The cerebrum consists of the frontal, parietal, occipital, and temporal lobes (Figure 3.4). Although specific functions of these lobes have been postulated by various authors and have some basis in evidence, such as through the Brodmann areas, these remain mostly conjecture and not very well understood. The cerebellum is a smaller section of the brain located on the bottom of the brain, and is typically associated with more primitive functions [NIH 2012]. The cerebellum contains approximately 80% of the neurons in the brain while only contributing about 10% of the mass [Azevedo et al. 2009]. Recent studies have demonstrated that there is a high degree

of individuality in the neuronal architecture of the brain, which further complicates regional associations with function [Freund et al. 2013].

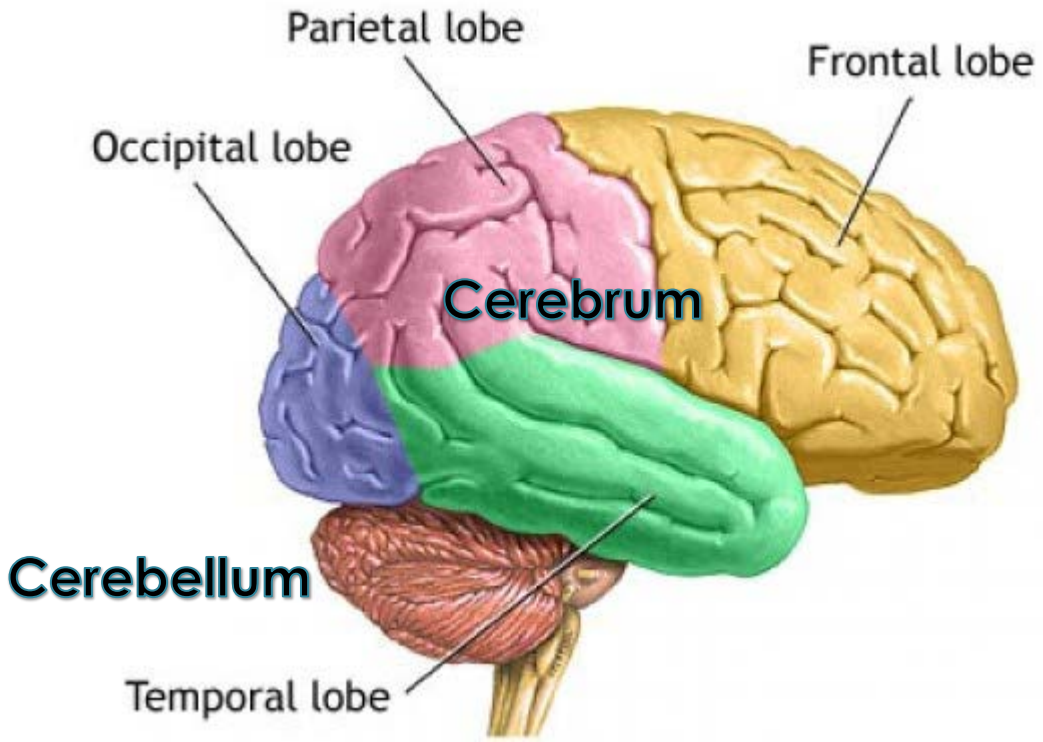

Figure 3.4: The lobes of the brain [MDhealth]

3.2.3 Surrounding Structures of the Brain

The brain is held inside the skull by a series of soft tissue membranes called the meninges, and surrounded by cerebrospinal fluid (CSF). The meninges are made up of three layers which starting from the skull, are called the dura mater, the arachnoid mater, and the pia mater (Figure 3.5).

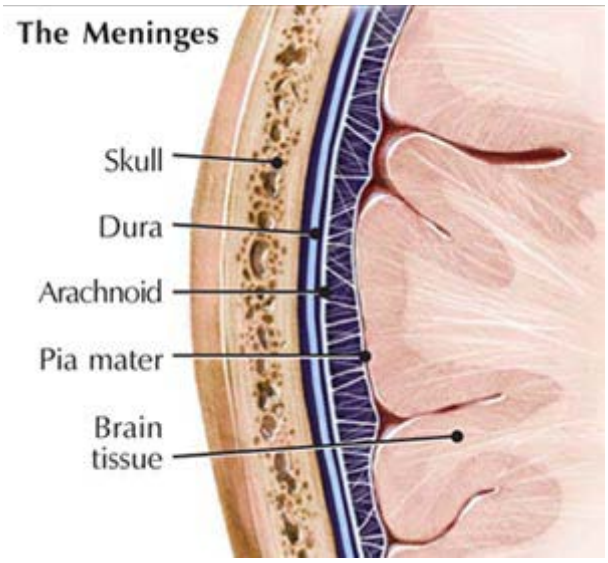

Figure 3.5: The meninges of the brain [Brainmind]

The dura mater is the membrane closest to the skull, and is relatively thick and durable. It is composed of two sublayers, a thin membrane near the skull called the periosteal layer, and a thicker fibrous layer called the meningeal layer, which makes up the bulk of the dura mater. In addition to providing mechanical support to the inner meninges and brain, the dura mater also serves to carry blood supply to and from the brain through a series of bridging veins. [McKinley 2008]

The dura mater also exhibits a significant degree of folding between various sections of the brain. These folds create distinct features in the brain called dural folds. The two main dural folds are the tentorium cerebelli which separates the cerebellum and the brainstem from the occipital lobe, and the falx cerebri which separates the two hemispheres of the brain (Figure 3.6). The space between the dura mater and the skull is called the epidural space.

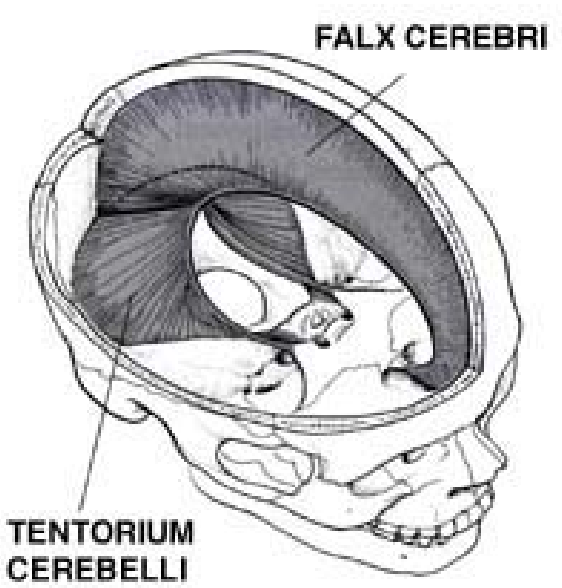

Figure 3.6: The primary dural folds in the human brain [Rosen 2000]

In between the dura mater and the next layer of the meninges, the arachnoid mater, is the subdural space. Typically, the subdural space is filled due the presence of cerebrospinal fluid which pushes the arachnoid mater in contact with the dura mater. However, the subdural space can open up as a result of trauma to the head, most notably in cases where tearing of bridging veins results in blood pooling, causing subdural haematomas. Mechanically, the arachnoid mater is soft and thin compared to the dura mater. [Moore 1999]

The subarachnoid space is between the arachnoid mater and the final layer of the meninges, the pia mater. The subarachnoid space is where the cerebrospinal fluid is generated and circulated. For this reason, the pia mater is impermeable to fluid. Mechanically, the pia mater is the most delicate of the meninges, and appears as a thin and translucent membrane.

Cerebrospinal fluid (CSF) is a clear and colourless fluid and serves as mechanical and immunological protection for the brain and nervous system. Cerebrospinal fluid is constantly

being produced and reabsorbed in the body, with approximately 150 mL of the fluid being circulated at once. Chemically, the CSF is composed of mainly water, with various biological components. The CSF has also been shown to play an important role in clearing waste materials generated by the brain tissue. Another function of the CSF is to maintain the brain mass at a neutral buoyancy, so that the weight of the brain does not impair its function. [McKinley 2008]

3.3 Mechanical Properties of Relevant Tissues in the Head

For the purpose of modeling and understanding the effects of blast injury, an accurate assessment of the mechanical properties of the tissues is of vital important. Biological tissues are inherently heterogeneous, with various components intermingled and interacting with each other at the cellular level. Thus, when investigating the mechanical properties of such materials using full-scale finite element models, a continuum assumption must be made. That is, at a large enough length scale, and at small deformations, it is assumed that the material behaves homogeneously.

3.3.1 Brain Tissue

In vivo studies of human brain tissue are inherently limited in terms of feasibility, so much of the database of experimental values of brain tissue properties are from animal tests or post mortem human subjects. Consequently, there have been studies conducted specifically to evaluate the validity of scaling animal test data to humans [Zhu et al. 2013a, Jean et al. 2014], and to characterize the effects of tissue degradation on measured properties [Hrapko et al. 2008, Prevost et al. 2011, Zhang et al. 2011a, Rashid et al. 2013]. Both of these factors can significantly affect the results of a study, and should be recognized as important caveats.

Brain tissue has been shown to exhibit nearly incompressible, non-linear, anisotropic, hyperelastic, and viscoelastic behaviour [Prange 2002, Abolfathi et al. 2009]. Furthermore, the brain has also been shown to exhibit regional variation in mechanical properties [van Dommelen et al. 2010, Elkin et al. 2011, Finan et al. 2011, Lee et al. 2014]. Although brain tissue has been widely characterized in numerous experimental studies in the literature, the complexity and heterogeneity of the tissue and differing experimental methods has resulted in significantly large variance in measured properties.

One technique that allows for some measurement of tissue response in vivo, is magnetic resonance elastography, which can be performed on human volunteers. This technique uses low amplitude shear waves that are imaged using magnetic resonance imaging and is capable of measuring viscoelastic properties, although the loading regimes are necessarily limited to low deformations. One recent study that performed tests on excised post mortem human subject brain tissue reported the tissue response of various regions of the brain in tension, compression, and shear loadings [Jin et al. 2013]. This comprehensive study found that there was a statistically significant difference between white matter and grey matter in compression and shear, with white matter exhibiting marginally greater stiffness in compression and shear. Furthermore, regional variation (between the corona radiata, thalamus, corpus callosum, and cerebral cortex) was reported to exist in compression and tension with the corona radiata showing marginally greater stiffness than the other three regions. The material properties of brain tissue from a variety of literature sources are summarized in Table 3.1, and viscoelastic properties of brain tissue are summarized in Table 3.2.

Table 3.1: Material properties of brain tissue

Literature Source	Density (kg/m3)	Poisson's Ratio	Elastic Modulus (kPa)	Notes
[Alley et al. 2011]	1060	0.5	30 37	Grey matter White matter
[Kaster et al. 2011]			1.195 1.787	Grey matter White matter
[Christ et al. 2010]			0.384-0.546 0.152-0.508	Grey matter White matter
[Zhu et al. 2010a]			9.3 12.3	Thalamus Corona Radiata
[Taylor 2004]		0.35 – 0.5	3.15 0.58	High strain rate Low strain rate
*[Kumaresan 1996]	1040	0.48	66.7	
*[Ruan 1996]	1040	0.499	558	
*[Bandak et al. 1995]	1220	0.48	68 000	
*[Zhou et al. 1995]	1040	0.499	500 800	Grey matter White matter

*not experimentally derived values

Table 3.2: Viscoelastic properties of brain tissue

Literature Source	Storage Modulus (kPa)	Loss Modulus (kPa)	Location
[Zhang et al. 2011b]	1.77±0.24 1.85±0.18 2.34±0.22 2.41±0.23	0.94±0.17 1.10±0.23 1.11±0.03 1.21±0.21	Cerebellum (grey) Cerebellum (white) Cerebrum (grey) Cerebrum (white)
[Zhu et al. 2010a]	10.8 21.0	3.1 4.1	Thalamus Corona Radiata
[Sack et al. 2009]	2.01±0.23	0.80±0.13	Grey and white
[Green et al. 2008]	3.01±0.10 2.70±0.1	2.50±0.20 2.50±0.20	Grey matter White matter
[Hamhaber et al. 2007]	3.50±1.33		Grey and white
[Klatt et al. 2006]	0.84 – 2.28	0.57 – 2.96	Grey and white

Many of the existing studies that have characterized brain tissue properties have done so in the context of automotive, blunt impact, or surgical modeling. More recently, some groups have

conducted studies at high strain rates to understand the high rate behaviour of brain tissue in the context of blast [Pervin 2009, Pervin 2011, Shafieien et al. 2011, Sista 2011]. This work has demonstrated a significant strain-rate dependence on the stiffness of brain tissue at high rates (Figure 3.7).

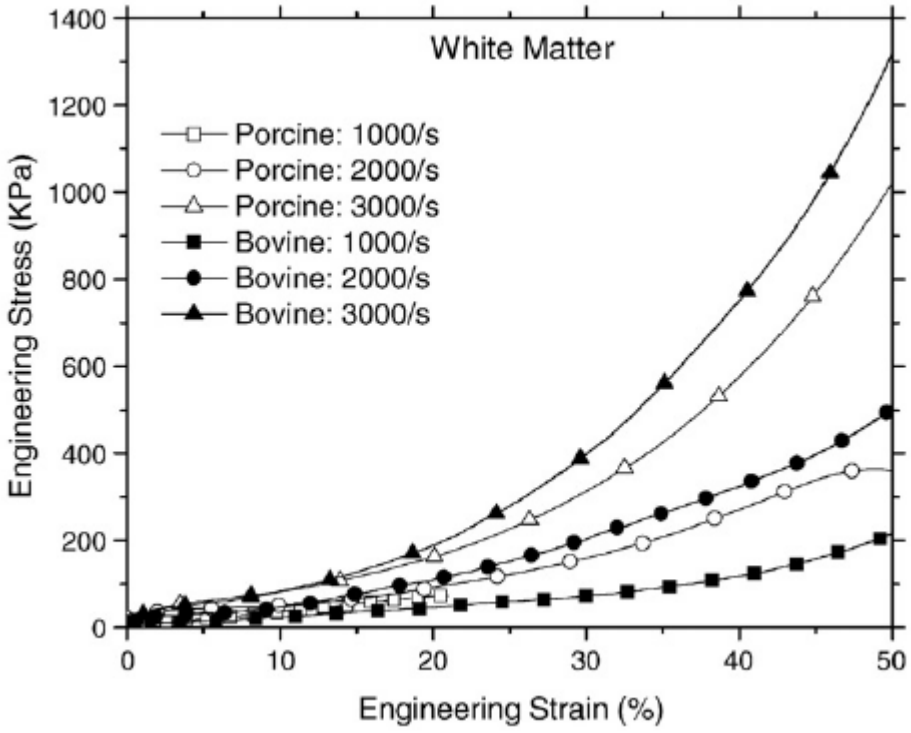

Figure 3.7: Brain tissue stress-strain response at high strain rates (adapted from Pervin et al. 2011)

3.3.2 Skull Tissue

The human skull is made up of a cancellous bone layer called the diploe, surrounded by two cortical bone layers called the inner and outer tables. Cortical bone is dense and compact, while the cancellous bone is relatively soft and porous [McKinley 2008]. This sandwich structure allows the skull to have some degree of deformability while maintaining enough rigidity to

provide physical protection to the brain. Numerous studies in the literature have undertaken physical tests on human bones to characterize the material properties, and the properties of the skull bones from various sources are summarized in Table 3.3. As with many biological tissues, the properties of the skull demonstrate significant variability, which may be due to different regions of the skull tested, individual-specific variables, and different experimental methodologies.

Table 3.3: Material properties of the skull

Literature Source	Density (kg/m^3)	Poisson's Ratio	Elastic Modulus (MPa)
[Ruan 1994]	1410	0.22	6 650
[Baumgartner et al. 2009]	1800	0.21	15 000
[Chafi et al. 2011]	2100	0.23	15 000
[Ganpule et al. 2009]	1710	0.19	5 370
[Roberts et al. 2012]	2080	0.22	8 000

3.3.3 Cerebrospinal Fluid

The cerebrospinal fluid (CSF), even more so than other biological soft tissues, is predominantly composed of water (approximately 99% water by volume). Cerebrospinal fluid is a Newtonian fluid, with dynamic viscosity and density similar to blood plasma [Loth et al. 2001]. The mechanical characterization of CSF is quite limited in the literature, and most numerical models assume bulk properties to be those of water. The properties of cerebrospinal fluid used in various numerical models in the literature are summarized in Table 3.4. The values in Table 3.4 are not experimentally derived values, but rather are assumed values based on the similarity of CSF with water.

Table 3.4: Mechanical properties of CSF used in numerical models in the literature

Literature Source	Bulk Modulus (GPa)	Density (kg/m^3)	Poisson's Ratio
[Kleiven 2008]	2.1	1000	0.5
[Sayed et al. 2008]	2.19	1004	0.5
[Chafi et al. 2011]	2.19	1000	0.5
[Ruan 1994]		1040	0.499

3.4 Visible Human Project

The Visible Human Project (VHP) is a scientific venture conducted by the National Institutes of Health of the United States of America, to enhance the understanding of human anatomy through improved visualization. The VHP used donated cadavers which were embalmed and cryogenically frozen, and then thinly sliced to create a sequence of highly detailed section views throughout the body in all three planes of reference (Figure 3.8, sagittal plane shown).

The VHP consists of sections from both a male and a female subject. Only the geometry from the male anatomy was used in this work. The male dataset consists of a combination of MRI, CT, and anatomical slices in each of the anatomical planes of the body, providing a comprehensive database of images. The resolution of the images of the VHP male dataset is 0.33 mm. The VHP male was a donor who was 38 years of age at the time of his death, and was 1.8 m (71") tall with a body weight of 90.2 kg (199 lb) [Spitzer et al. 1996]. It is important to note that these measurements do not represent the 50^{th} percentile male, as the VHP male was heavier than the traditional 50^{th} percentile male definition. The sagittal and transverse sections of the head from the Visible Human Project have sufficient resolution to distinguish between different tissues in the head, and thus are well suited to guide the anatomical geometry of numerical models of the head (Figure 3.9).

Figure 3.8: Visible Human Project (mid-sagittal slice) [VHP]

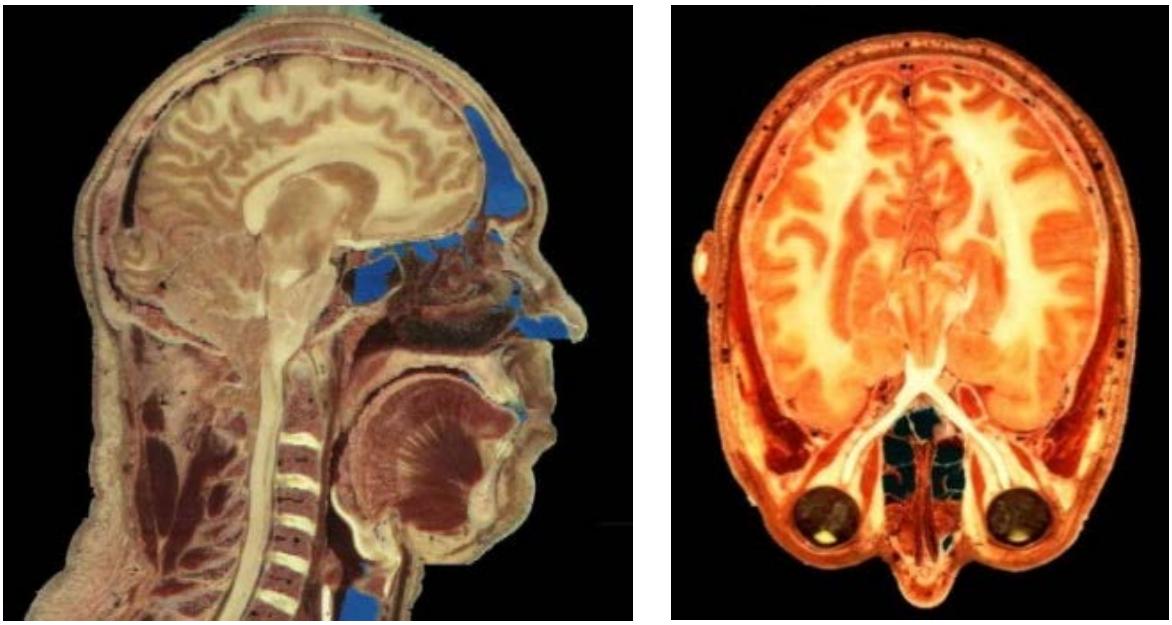

Figure 3.9: Sagittal and Transverse sections of the VHP male [VHP]

4. Overview of Blast Injury

In recent primary blast injury research, there has been a significant effort to understand and mitigate mild Traumatic Brain Injury (mTBI) caused by the blast pressure wave interacting with the head, which has been identified as a clinically significant issue. Although there is no universally accepted definition of mTBI, it is generally considered to result in some combination of a loss of consciousness, post-traumatic amnesia, and general confusion or headaches following exposure to an injurious loading condition. The US Department of Veteran's Affairs defines mTBI to be a closed head impact where structural imaging of the brain is normal, loss of consciousness is for no more than 30 minutes, and post-traumatic amnesia is present for no longer than 1 day [Kay et al. 1993]. Mild TBI is generally thought to be a contributing factor in the historical diagnosis of 'shell shock', which was first observed during WWI, where soldiers operating in trench warfare were routinely exposed to blasts from artillery shells. Due to the similarity in both causes and symptoms, there is a significant diagnostic overlap between mTBI and Post Traumatic Stress Disorder (PTSD), which is a psychological disorder. [Elder 2009]

In this chapter, a brief history of blast injury characterization will be covered, predominantly in the context of head injury. The mechanisms of primary blast injury, as well as injury criteria, will also be discussed.

4.1 A Brief History of Blast Injury

The earliest investigations into primary blast injury were focused on pulmonary or auditory injuries. This was due to the relative lack of protection provided to the torso in the battlefield

resulting in the most noticeable symptoms of PBI manifesting in the lungs rather than the brain. Only with the more recent advances in protective equipment to the torso, has the prevalence of mTBI due to blast exposure been brought to light. The first instances of research into the direct effects of blast exposure were following WWI, where the predominance of artillery was first demonstrated on a large scale [Sellier 1994]. Studies typically exposed animals to varying levels of blasts and observed the effects on the animal behaviour. These experiments primarily resulted in pulmonary injuries, and brain tissue injuries were not observed [Hooker 1924]. Further testing on pulmonary injuries resulting from blast was conducted in the 1940s and 1950s, which lead to the discovery that the primary blast overpressure can transfer energy directly into the body, and the importance of impedance mismatches in governing tissue stresses [Zuckerman 1940, Clemedson 1956].

One of the first attempts to correlate specific blast loadings with injury was by Bowen [Bowen et al. 1968], who used animal test data to predict the likelihood of lung injury with various blast overpressures and durations. This research generated the Bowen curves, which establish thresholds for the probability of lethal lung injury for a 70 kg human male in various prone and upright positions, as a function of blast overpressure and duration (Figure 4.1). Although the Bowen curves only depend on incident pressure and duration, they do report lower thresholds in situations where the person is standing in front of a wall, due to the reflected pressures caused by the wall. The survivability thresholds in the Bowen curves correspond to scaled values of the survival of the animals 24 hours after blast exposure [Bowen et al. 1968].

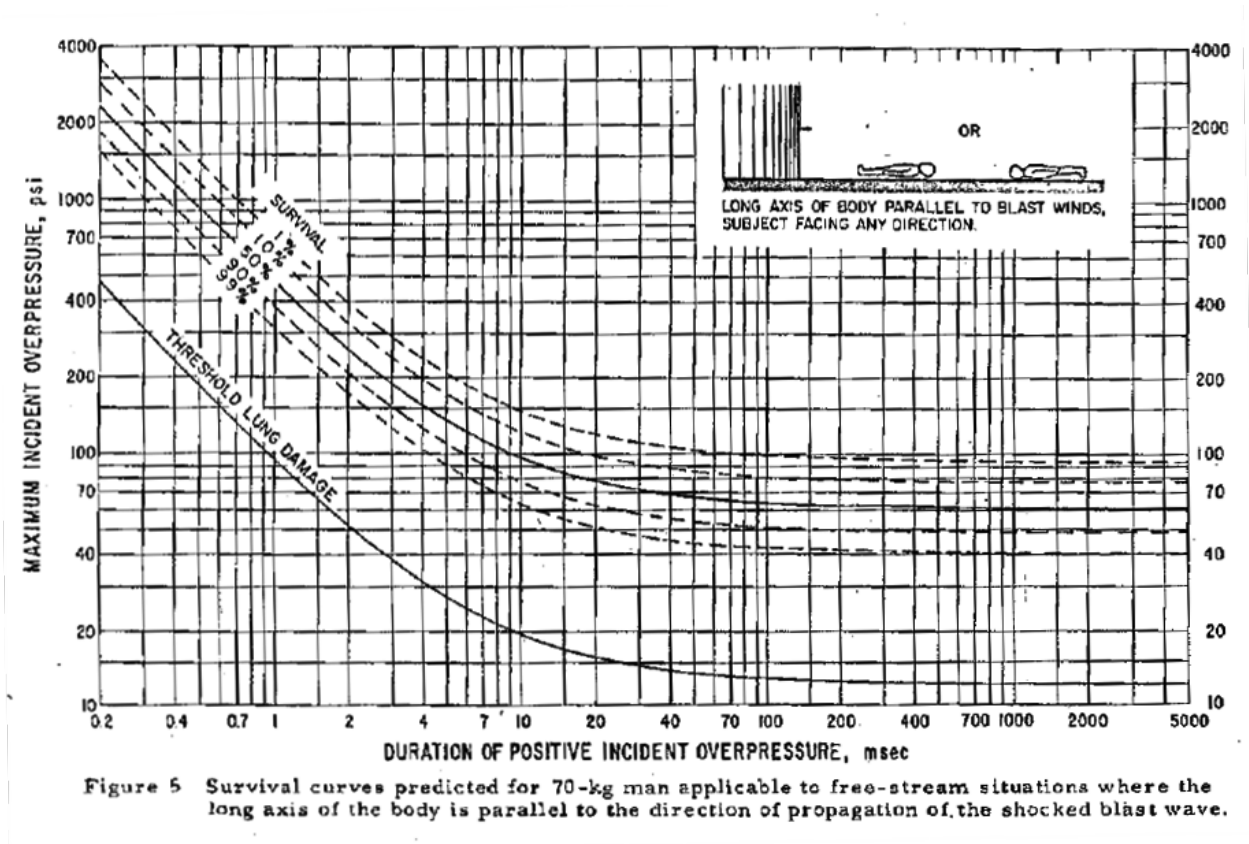

Figure 4.1: Bowen Curves for prone position [adapted from Bowen et al. 1968]

A review of the Bowen curves was conducted by Bass et al., and the curves were updated to include a wider range of animal test data [Bass et al. 2008], and further updated to distinguish between single and repeated exposures [Panzer 2011a]. These injury risk curves, while of great importance in pulmonary injury prediction and blast lethality assessment, do not attempt to correlate blast loading with head or brain injury. Recent work by Rafaels et al. has attempted to accomplish this, using small animals with thoracic protection exposed to blast loads in a shock tube [Rafaels et al. 2011, Rafaels et al. 2012]. These studies generated injury risk curves for blast fatality by relating survivability of the small animals with the inputted blast loads (Figure 4.2).

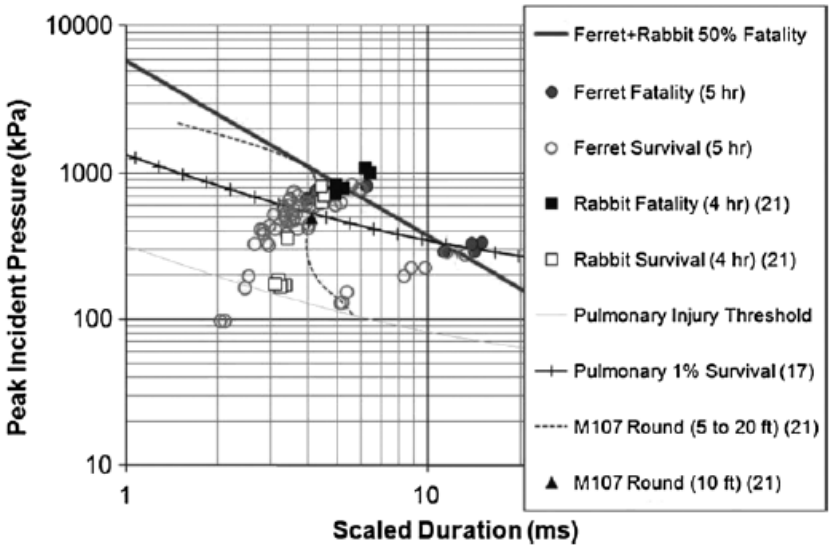

Figure 4.2: Injury risk curves for primary blast wave exposure (adapted from Rafaels et al. 2012)

In parallel to the injury risk curves developed by groups such as Bowen, Bass, and Rafaels, there has been mathematical models to predict blast injury. Stuhmiller developed a mathematical model to predict lung injury by analyzing the chest and lungs as a piston and compressible gas system [Stuhmiller et al. 1996]. The Stuhmiller model circumvents the difficult problem of local tissue response variables by treating the chest and lungs as a mechanical system. This model calculates the energy dissipated in the lung tissue in the form of work performed on the chest wall by the blast pressure wave, and correlates injury to the amount of work. The Stuhmiller model rates injury in terms of severity level rather than probability of injury. A similar mathematical blast injury model of the thorax was developed by Axelsson [Axelsson 1996], who used blast test data on sheep conducted by Yelverton [Yelverton 1993]. More recently, there have been numerous studies published on animals, both rodent [Bolander et al. 2011, Leonardi et al. 2011, Saljo et al. 2009] and porcine [Saljo et al. 2008, Shridharani et al. 2012], exposed to blast and the resulting injuries. These studies have concluded that primary blast can generate significant dynamic intracranial pressures in the brain and cause fatalities at high overpressures.

4.2 Mechanisms of Primary Blast Injury

In the most general sense, primary blast injury is caused by a pressure wave that produces a crushing force on the body, causing injurious stresses in the organs. The specific mechanisms and pathophysiology of injury can vary depending on the severity of loading and the type of tissue in question. In high severity loadings, the mechanism of injury is often clear – large contusions in the brain tissue or cerebral haematomas are generally easy to identify. One of the characteristics of mTBI is the lack of obvious signs of injury, suggesting a more subtle form of injury that affects the brain tissue. With regards to mild traumatic brain injury caused by blast exposure, there have been numerous mechanisms of injury proposed in the literature, some of the more prevalent of which are discussed below, although there is currently no strong consensus among the blast injury community.

One of the better understood types of injury in closed head injuries is diffuse axonal injury (DAI), which is caused by stretching and shearing of the axonal fibers that consequently impairs the function of the cells, and can eventually lead to cell death [Abolfathi et al. 2008]. The interfaces of grey and white matter and other areas with changes in density or bulk properties are thought to be particularly susceptible to DAI.

Another widely known potential injury mechanism in primary blast is cavitation of the cerebrospinal fluid surrounding the brain due to negative, or tensile, pressures induced by the blast wave. Cavitation is a well-known damage mechanism in naval engineering, where the generation and subsequent collapse of cavitation bubbles in water create high pressures on propellers blades in a phenomenon known as ‘pitting’. A similar phenomenon has been proposed in primary blast injury, whereby the collapse of cavitation bubbles adjacent to brain tissue can cause sharp

pressures spikes and lead to trauma in the tissue. Cavitation as a blast injury mechanism is predicated on the ability of the blast wave to generate sufficient negative pressures in the head to cause the CSF to cavitate, and this has been investigated by many authors [Moore et al. 2008, Wardlaw 2010, Goeller 2012, Panzer 2012, Singh et al. 2013], although cavitation of CSF has not yet been observed directly in vivo as a response to blast loading. Furthermore, a major limitation in blast induced cavitation research is the lack of sufficient knowledge on the cavitation thresholds of CSF, which is an area of active research [Singh 2014, Subhash et al. 2013].

More recently, groups have attempted to relate mTBI caused by blast exposure to biochemical processes in the brain by tracking various neuromarkers in animal tests [Cernak et al. 2011, Balakathiresan et al. 2012, Lucca et al. 2012, Valiyaveettil et al. 2012, Svetlav et al. 2012]. Although the results of these types of studies are promising, the complexity of neurological activity makes it challenging to derive any definitive conclusions about injury mechanisms at this point.

Effgen et al. [Effgen et al. 2013] exposed in vitro slice cultures of rat brain tissue to blast loadings using a shock tube, and tracked cell death in the tissue following blast exposure to determine if indeed a primary blast shock wave alone is sufficient to generate injuries in the tissues. They found that samples exposed to blast exhibited greater cell death than control samples, indicating a greater potential for injury. Vogel et al. [Vogel et al. 2014] used a similar method of exposing brain tissue cell cultures to shock tube loading, and found that blast exposure resulted in the disruption of long term potentiation in the brain tissue cells, even at low level blast loads that did not result in cell death, suggesting that long term potentiation may be a mechanism of injury relevant to mTBI.

There have also been other mechanisms of injury for blast brain injury, including an increased electric field around the brain caused by skull piezoelectricity [Lee et al. 2011], increased vascular pressure that reaches the brain from the blast wave impacting the torso [Bhattacharjee 2008], and skull flexure inducing or amplifying stress waves in the brain [Moss et al. 2009, Bolander et al. 2011]. In summary, although there are many proposed mechanisms of injury in primary blast, there is of yet no consensus. This is unsurprising due to the complexity of both the nature of the loading and the nature of the brain. In all likelihood, the precise pathophysiology of mTBI caused by primary blast is not a single universal pathway, but a combination of variables that requires significantly more research to fully comprehend. Regardless, the lack of well understood injury mechanisms does not preclude the existence of such injuries nor should it hamper the investigation of the head and brain response to primary blast as is the focus of the current work. It does, however, limit the ability of such investigations to relate measured response to specific injuries.

4.3 Injury Criteria

While the mechanisms of primary blast are not well understood, injury criteria can still be used to try to evaluate the possibility and severity of primary blast injury. Impact and injury biomechanics is inherently limited in a number of ways. Firstly, experiments using living human beings under loading conditions that could cause injury are justifiably unacceptable. Secondly, animal or surrogate models are limited in terms of biofidelity and scaling the results to be relevant to humans. Thirdly, the highly complex and inconsistent nature of biological organisms and tissues makes injury research a highly statistical endeavour. Consequently, blast injury researchers have employed numerous statistical techniques and scaling laws to correlate animal test data with human injury tolerance levels.

A great portion of the research into head and brain injury has been undertaken by the automotive industry, where significant resources are available to prevent automobile collision related injuries. More recently, there has also been a significant interest in sports-related head injuries, most notably in American football, where head trauma resulting in concussions has been recognized as a major clinical issue [Zhang et al. 2004]. Although neither automotive nor sports related head injury thresholds are directly applicable to blast due to the inherent differences in loading and duration, they provide a foundation of knowledge over which blast injury can be characterized.

Injury criteria for brain injury can be divided into two general types: global kinematics based criteria, and local tissue response based criteria. Kinematics based criteria use measures of the overall kinematics of the head, such as translational and/or rotational acceleration. In contrast, local tissue response based injury criteria use measures of stress and/or strain in the brain tissue to correlate with injury.

4.3.1 Global Kinematics Based Injury Criteria

The main benefit of global kinematics based injury criteria is that they are relatively easy to measure experimentally, since they only measure external loading to the head. Consequently however, they cannot take into account the internal responses of the tissues. The simplest kinematic measure of head response is the resultant head acceleration. Acceleration response can be characterized as either linear, rotational, or a combination of the two. In general, humans can tolerate greater accelerations for shorter durations as demonstrated by the Wayne State tolerance curves, although there is no consensus for acceleration thresholds of the head for very short durations relevant to blast.

One of the most widely used kinematic injury criteria is the Head Injury Criterion (HIC), which was developed for the automotive industry and has been used extensively in automotive safety standards. Although HIC is not directly applicable to blast, it provides a comparative benchmark criterion with which head kinematics resulting from blast loads can be evaluated. The Head Injury Criterion is obtained by calculating the time integral of the resultant linear acceleration of the head over a specified duration of loading, where the duration is chosen such that the HIC value is maximized (Equation 4.1).

$$\mathrm{HIC} = \max\left\{\left[\frac{1}{(t_2 - t_1)}\int_{t_1}^{t_2} a(t)dt\right]^{2.5}(t_2 - t_1)\right\} \qquad \textit{Equation 4.1}$$

Where acceleration is in g's, and time is in seconds. There are different standard maximum acceleration loading durations that are used, the most common of which is HIC_{15}, corresponding to a maximum duration of 15 ms. The generally accepted tolerance limit of HIC_{15} used in the automotive industry is 700, which corresponds to a 5% probability of severe head injury. The probabilities of failure for HIC were calculated using the Wayne State tolerance curves, which are based on the onset of skull fracture in blunt head impacts [Hutchison 1998]. HIC has been used in the literature to predict likelihood of head injury resulting from blast loads [Dionne 2002, Makris 2000].

There are some other translational acceleration based injury criteria in the literature, including the Gadd Severity Index [Gadd 1966], and the Japanese human head tolerance curve [Ono et al. 1980]. Another kinematics based injury criterion was proposed by Gennarelli that takes into account rotational accelerations [Gennarelli et al. 2003]. There is also a more recent global injury criterion called the Head Impact Power (HIP), which is based on the total power input to

the head [Newman et al. 2000]. The HIP criterion was developed using data from NFL football collisions, and it considers all six degrees of motion.

Although there is certainly great value in developing new and novel criteria using more complete measures of head kinematics beyond just translational acceleration, the widespread use and acceptance of HIC in the impact biomechanics community makes it a valuable benchmark for comparison. Furthermore, the HIP and Gennarelli rotational criteria have been found to produce trends comparable to HIC for a wide range of blast loads [Cronin et al. 2008]. It should be emphasized that these global injury criteria were not developed nor originally intended for use in blast overpressure scenarios, and therefore they have not been verified in these loading regimes. However, as there is no clear consensus for blast head injury criteria, these measures can provide comparative benchmarks for evaluating kinematics response from blast.

4.3.2 Local Tissue Level Injury Criteria

In contrast to global kinematics based injury criteria, local tissue based criteria are more direct measures of injury present in the tissues themselves. In general, the metrics used for local tissue criteria are various measures of stress, strain, and/or strain rate. Tissue based criteria have the benefit of a more direct pathophysiological justification for the predicted injuries, although are generally more difficult to measure experimentally than global criteria. One benefit of finite element models is that it is very simple to measure local tissue response in the models.

Intracranial pressure (ICP) is one of the most commonly used brain tissue injury response metrics. In this context, ICP refers to a dynamic measure of the local hydrostatic pressure in

the brain tissue as a result of a blast or blunt impact loading, as opposed to static or prolonged intracranial pressure that could be caused by a cerebral haematoma for example. Ward et al. [Ward et al. 1980] used a finite element model to develop thresholds of intracranial pressure by applying acceleration to the head and observing the pressures generated during injurious accelerations of the head. This analysis resulted in intracranial pressure limits of 172 kPa for moderate injury, and 234 kPa for severe injury. Kleiven [Kleiven 2007] used data from NFL collisions to reconstruct loading kinematics in a finite element model to generate injury curves for probability of concussion, and reported an intracranial pressure of 65.8 kPa for 50% probability of concussion. Zhang et al. [Zhang et al. 2004] used a similar method and reported an average ICP of 90 +/- 24 kPa for injurious loadings.

Negative, or tensile, intracranial pressure is another common response metric. Deck et al. [Deck 2008] reported a negative pressure threshold of 135 kPa for CSF to correspond to a 50% risk of subdural haematoma using a finite element to generate injury risk curves. Although cavitation induced brain injury is currently only a hypothesized injury mechanism that has yet to be experimentally verified, many studies have used estimated negative pressure injury thresholds to evaluate the potential for injury, even though the cavitation pressure threshold of CSF has not been measured in the literature. Thus, the cavitation pressure limits of CSF have been estimated based on measured properties of water. Negative pressure limits of water vary over several orders of magnitude, from 0.1 – 20 MPa according to the level of air saturation or the presence of impurities [Herbert et al. 2006]. When water is highly saturated with gases or particles, such as the case with CSF, these provide nucleation sites for cavitation bubbles to form, thereby reducing the negative pressure limit before cavitation occurs. Panzer et al. [Panzer et al. 2012] used a cut-off value for negative pressure of 100 kPa in their finite element

model to predict cavitation. And Coleman et al. [Coleman et al. 1995] reported a negative pressure threshold for soft tissue of 1.5 – 3.5 MPa based on acoustic pressure measurements in water.

Maximum shear stress is another brain tissue based response metric that has been used to predict brain injury. Shear stress has been hypothesized to be a measure of subarachnoid haematoma or diffuse axonal injury. Zhang et al. [Zhang et al. 2004] reported shear stress values of 6.0 kPa, 7.8 kPa, and 10.0 kPa corresponding to 25%, 50%, and 80% probability of mTBI respectively, from data collected from NFL player collisions.

In addition to the various measures of stress discussed above, first principal strain is also widely used as a local brain tissue response metric. First principal strain was favoured for this purpose above the Von Mises, or effective, strain due to the presence of directional axons in the brain tissue, which are hypothesized to cause injury by stretching, and first principal strain is a more analogous representation of axons. However, there is no guarantee that the strain induced in brain tissue will be oriented with axon direction. Elkin et al. [Elkin 2007] conducted experiments on in vitro samples of rat brain tissue and reported an injury threshold of between 0.10 – 0.20 for Lagrangian strain for the onset of cell damage. Wayne State University conducted research on rats and reported a peak first principal strain value of 0.121 resulted in axonal damage [Mao 2009]. More recently, a similar study by the same group reported a value of 0.30 correlated with the onset of brain contusion in rats [Mao et al. 2011]. Kleiven [Kleiven 2007] reported a peak first principal strain threshold of 0.26 for a 50% probability of concussion. And Deck et al. [Deck 2008] reported a threshold value of 0.40 indicated mild diffuse axonal injury.

Similar to the global kinematics criteria, it should be noted that all of the strain criteria were developed for blunt impact or automotive crash type impact scenarios, and not for blast. However, they can provide comparative values with which the tissue response in blast can be compared. An overview of the tissue level injury criteria in the literature for various response metrics is summarized below in Table 4.1.

Table 4.1: Local brain tissue injury criteria summary

Metric	Threshold	Notes	Source
Intracranial Pressure (kPa)	234 172	for severe injury (impact) for moderate injury (impact)	[Ward 1980]
	90 +/- 24	for mTBI based on NFL collisions	[Zhang et al. 2004]
	66	for 50% probability of concussion	[Kleiven 2007]
Negative Intracranial Pressure (kPa)	-1300 – 3500	for cavitation in soft tissue	[Coleman et al. 1995]
	-55	for 50% probability of concussion	[Kleiven 2007]
	-135	for 50% probability of subdural haematoma	[Deck 2008]
	-100	Estimate for onset of CSF cavitation	[Panzer et al. 2012]
Shear Stress (kPa)	6 7.8 10	for 25% probability of mTBI for 50% probability of mTBI for 80% probability of mTBI	[Zhang et al. 2004]
First Principal Strain	0.3 – 0.6	Onset of vascular rupture	[Lovenheim 1974] [Lee 1989] [Monson 2003]
	0.20	Onset of DAI	[Bain 2000]
	0.14 0.19 0.24	for 25% probability of mTBI for 50% probability of mTBI for 80% probability of mTBI	[Zhang et al. 2004]
	0.10 – 0.20	Threshold for cell damage	[Elkin 2007]
	0.26	50% probability of concussion	[Kleiven 2007]

	0.40	For mild DAI	[Deck 2008]
	0.121	Onset of axonal damage	[Mao 2009]
	0.30	For injurious brain contusion volume	[Mao et al. 2011]

Based on the preceding review of the literature, the most common injury response metrics in brain injury research are positive and negative intracranial pressure, and first principal strain. Thus, for blast injury numerical modeling, these metrics should guide the investigation of brain tissue response from blast. Effective strain rate, which is an invariant measure of strain rate and is commonly used in material behaviour characterization, and is also a useful metric to understand the importance of rate in terms of blast loading, which is inherently a high-rate phenomenon.

5. Overview of Helmet Protection

As early as the ancient Egyptian and Sumerian civilizations, humans have recognized the importance of protecting the head from injury. Consequently, helmets have been used throughout history for personal protection in both military and sporting endeavours. This chapter will cover a brief overview of the history of helmets, modern combat helmets and their materials, and the current understanding of helmets in the context of blast protection.

5.1 A Brief History of Head Protection

The earliest helmets were designed to protect against blunt or point impacts from clubs, spears, swords, or arrows, as these were the most common threat before the advent of firearms and explosives. The earliest archeological evidence of helmets is on a fragment of a monument called the Stele of Vultures, from an ancient Sumerian civilization from approximately 2600 – 2350 BCE (Figure 5.1). This fragment illustrates a row of soldiers with shields and spears, each wearing helmets. Although this is the earliest physical evidence of helmets in the archeological record, the concept of head protection by using some form of primitive helmet is certainly older than this. In prehistoric times, protective garments would have been made of a variety of natural materials, including wood, leather, and textiles [Cooper et al. 1997]. Numerous types of helmets using a variety of materials have been used throughout history with the primary aim of military superiority, some examples of which are shown in Figure 5.2.

Figure 5.1: Stele of Vultures, a fragment indicating early use of helmets in warfare, ca. 2500 BCE [Pouyssegur]

Figure 5.2: Examples of ancient helmets. Left, Corinthian hoplite bronze helmet ca. 500 BCE [Creative Commons]. Middle, Chinese stone helmet ca. 200 BCE [Creative Commons]. Right, Italian steel helmet ca. 1380 CE [TWCenter]

The next evolution in helmet technology came from the need to protect against firearms, which introduced a new threat in the form of ballistic impact. Although primitive forms of firearms were originally invented in China in the 13th century, they did not achieve widespread use in military encounters until around the 16th century [Chase 2003]. And although armourers were motivated to protect against this newfound threat, they were significantly limited in their choice of materials. The only practical material that could viably provide some degree of protection while maintaining feasibility in terms of manufacturability and wearability, was steel. Furthermore, the rapid advance in firearm effectiveness made steel plate or chain body armour practically obsolete by the 18th century, although helmets continued to be used [Cooper et al. 1997]. Steel as a helmet material continued to be used throughout the world wars, being the only available material that could be manufactured at such large scales. The advent of advanced composite materials lead to the development of Kevlar aramid fibre in 1965, which significantly improved the ballistic protection capability of body armour, including helmets.

5.2 Modern Combat Helmets

Modern helmet protection encompasses a combination of several factors, including environmental protection, eye and ear protection, ballistic protection, protection from concussive shock, comfort, and compatibility with other equipment [Lockhart 2010]. Today's militaries typically use Kevlar or other aramid fibre based helmets of generally comparable size and proportions. The entirety of modern combat helmets are too numerous to discuss, so two specific helmets will be looked at in detail: the Canadian CG634 helmet, and the United States PASGT helmet. The PASGT helmet is widely used across the world, and has readily available geometry and material properties information, contrary to more recent helmets, for which the details of many are still proprietary.

5.2.1 CG634 Helmet

In the Canadian Forces, the WW2 era M1 Helmet was replaced by the CG634 Helmet, which continues to be used today (Figure 5.3). The CG634 is made of a Kevlar shell, and is based on the French Gallet TC-3 helmet, although modified to be compatible with Canadian equipment. The CG634 helmet has a four-point chin strap, and uses a suspension strap system with a rubber and nylon webbing, combined with a foam liner [Canadian Forces Combat Helmet User Manual].

Figure 5.3: Canadian CG634 Helmet with camouflage cover [CMP]

5.2.2 PASGT Helmet

The Personnel Armor System for Ground Troops helmet, or PAGST helmet, is a combat helmet developed and used by the United States military since the 1980s (Figure 5.4). The PASGT

helmet consists of a Kevlar shell with a strap system to secure the helmet to the head, although some versions utilize foam pads that attach to the underside of the helmet.

Figure 5.4: PASGT helmet [McGuire]

The PASGT helmet shell is a one piece construction consisting of layers of Kevlar K29 fibre weave in a phenolic Polyvinyl Butyral (PVB) resin matrix. The PASGT helmet was replaced in the United States military by the Lightweight Helmet, the Modular Integrated Communications Helmet, and eventually by the Advanced Combat Helmet (ACH) [Folgar et al. 2007]. More recently, the United States is developing the Enhanced Combat Helmet (ECH) with increased ballistic protection performance [Tomkins 2014].

5.3 Helmet Materials

For the purpose of developing finite element models of helmets to evaluate blast protection, the mechanical properties of typical helmet materials must be understood. As the general form of modern combat helmets comprises of a Kevlar shell with foam lining, these two types of materials will be looked at in detail.

5.3.1 Kevlar Material Properties

Kevlar is a brand name aramid fibre of the DuPont chemical company, and widely used in modern combat helmets. The Kevlar composite material that is used in combat helmets is a layered aramid fibre weave in a resin. Aramid fibres are synthetic long chain polyamides which are well known for having a very high strength to weight ratio [Gower et al. 2008]. Kevlar specifically was first commercialized in 1972, and was recognized as a potential armour material due to its light weight and high impact resistance when reinforced with a matrix of resin. Kevlar reinforced resin is capable of protecting against low to moderate velocity impacts from projectiles by dissipating the energy of the impact in numerous ways, including cone shaped bulk deformation, shear plugging, primary fibre breakage, secondary fibre deformation, inter-fibre friction, and friction between the projectile and the Kevlar weave [Gogineni et al. 2012].

There are three common formulations of Kevlar fibre for ballistic applications, Kevlar K29 which is used in the PASGT helmet, Kevlar K129 which is used in the ACH helmet, and Kevlar KM2 used in various protective equipment. Kevlar K129 has a greater tensile strength, resulting in a marginally higher ballistic protection performance [Kulkarni et al. 2013]. In the PASGT helmet construction, the Kevlar K29 layers are impregnated with 16 – 18% by weight

of PVB resin and then compressed in a mold at high temperature and pressure to cure the resin [Folgar et al. 2007].

Due to the composite nature of Kevlar reinforced nature, it is a highly anisotropic material. Gower et al. investigated the anisotropic properties of K29 composite panels experimentally, and their results are summarized in Table 5.1. [Gower et al. 2008]

Table 5.1: K29 Kevlar composite properties (adapted from Gower et al. 2008)

Property	**Values reported in literature**	**Initial numerical values**	**Experimental values (static testing)**
E_1 (GPa)	18.5	18.5	17.86
E_2 (GPa)	18.5	18.5	8.3
E_3 (GPa)	6.0	6.0	-
u_{12}	0.25	0.25	-
$u_{31,32}$	0.33	0.33	-
G_{12} (GPa)	0.77	0.77	0.85
$G_{13,23}$ (GPa	5.43	2.71	-
r (g/cm3)	1.23	1.23	-
S_1 (MPa)	1850.0	555.0	444.9
S_2 (MPa)	1850.0	555.0	225.5
CS (MPa)	1200.0	1200.0	~900
S_{12} (MPa)	77.0	77.0	56.7
$S_{13,23}$ (MPa)	543.0	898.0	-
Sn (MPa)	34.5	34.5	-
ISS (MPa)	9.0	9.0	-
STF_1	0.1	0.03	0.045
STF_2	0.1	0.03	0.050

5.3.2 Foam Material Properties

Solid foams are used in many applications where energy absorption is required. The microstructure of foam materials is unique in that they are a cellular structure composed of a network of cell walls containing pockets of air. Differences in the size and structure of the

cellular network combined with the material properties of the cell wall material, result in a very versatile class of material, that can be either highly elastic or highly plastic (crushable). Solid foams can be divided into two types; open cell foams where the air pockets connect with one another, or closed cell foams where the air pockets are closed on all sides (Figure 5.5). Closed cell foams typically have greater compressive strength and are denser than open celled foams [Thom 2009].

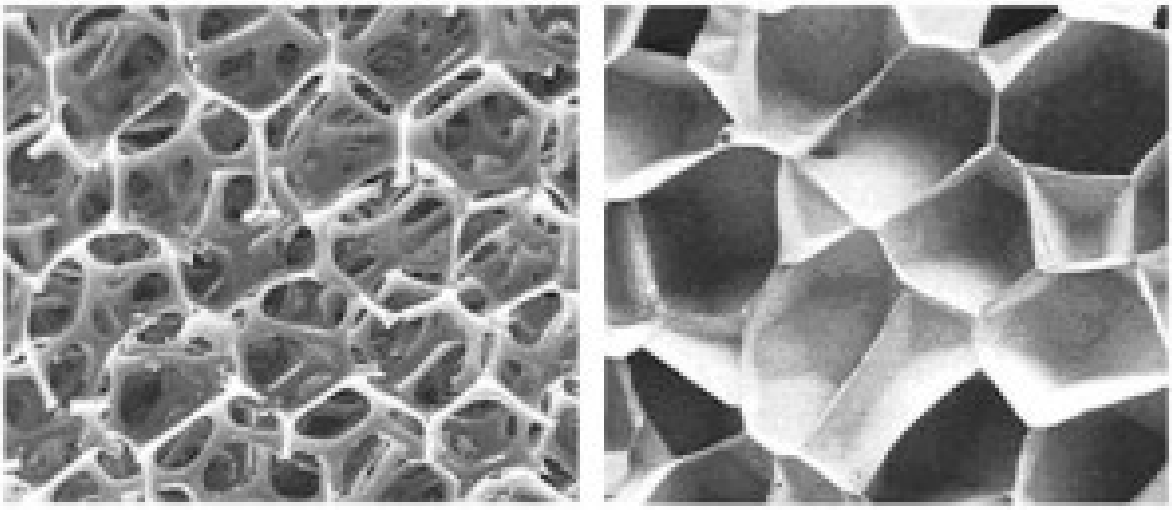

Figure 5.5: Open cell (left) vs. closed cell (right) foam [SFIP]

The compressive response of foams is generally well understood due to the prevalence of foam materials in safety applications for decades. The stress-strain curves for a foam material in compression can be divided into three distinct phases of loading (Figure 5.6). Initially, the cell walls of the foam will undergo bending, and the stress-strain curve will exhibit a linear elastic response with recoverable strain. Eventually, large compressive forces will cause buckling of the cell walls, which creates plastic deformation in the material and the stress-strain curve will enter a plateau region. Finally, as all of the air is pushed out from the foam, the foam undergoes

densification when the cell walls are in contact with each other, and the stress-strain curve becomes linear again according to the Young's modulus of the cell wall material itself. In closed cell foams the densification can occur without rupture of the cell walls, in which case the air becomes pressurized and contributes to the densification behaviour. [Thom 2009]

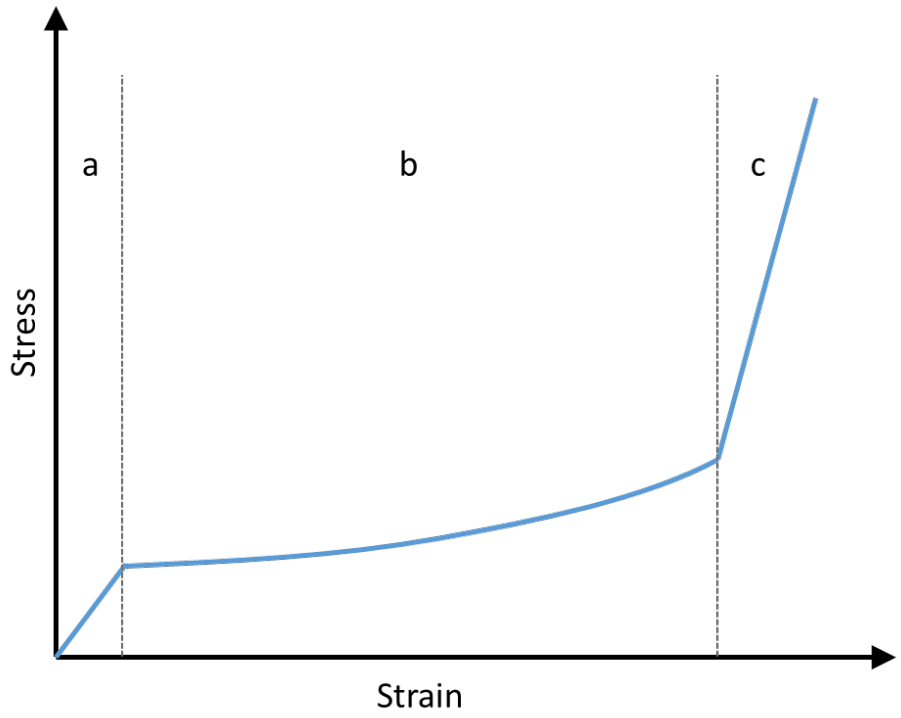

Figure 5.6: Stress-strain curve of typical foam (Adapted from Thom 2009)

Many different materials can be used to create foams. The most common for helmet materials are polymers, including variable density polyethylene, polyurethane, expanded polystyrene, and expanded polypropylene, although metal foams have also been investigated to some degree [Goel 2011]. The quasi-static stress-strain behaviour of foams is dependent on the material properties of the foam material in its solid phase, as well as the foam density. In general, increasing the density of a foam will increase the plateau stress and decrease the densification

strain (Figure 5.7) [Gibson & Ashby 1997]. Foams are also rate dependent, exhibiting generally stiffer response at higher strain rates (Figure 5.7).

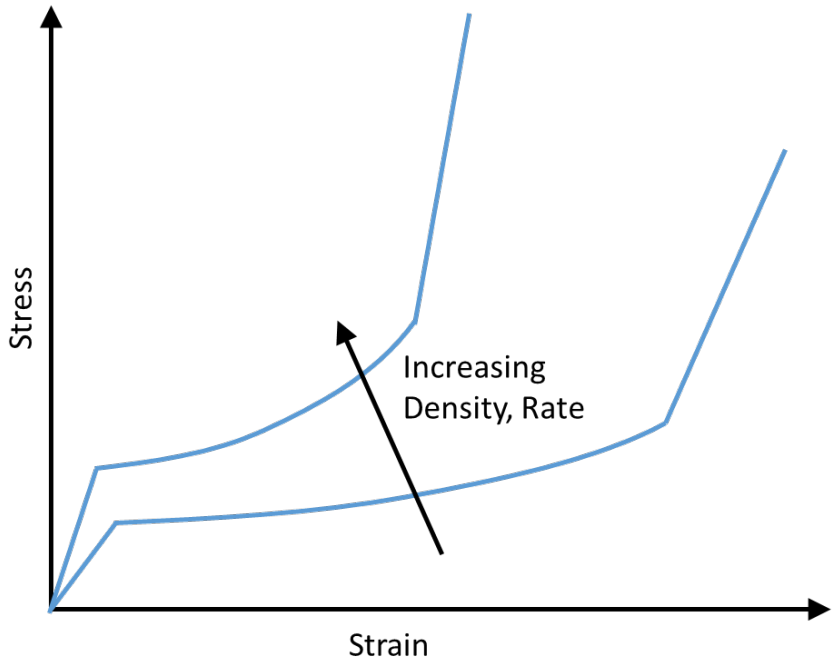

Figure 5.7: Stress-strain curve of foams with different density and different rates

Ouellet et al. [Ouellet et al. 2006] investigated the compressive response of several common foams at high rates relevant to blast loading, and found a significant rate dependence. Expanded polystyrene and polyethylene foams exhibited increased plateau stress and decreased densification strain as the strain rate increased, and the rate dependence was greater as the foam density increased (Figure 5.8, Figure 5.9). A similar trend was observed experimentally by Bioux et al. [Bioux et al. 2009].

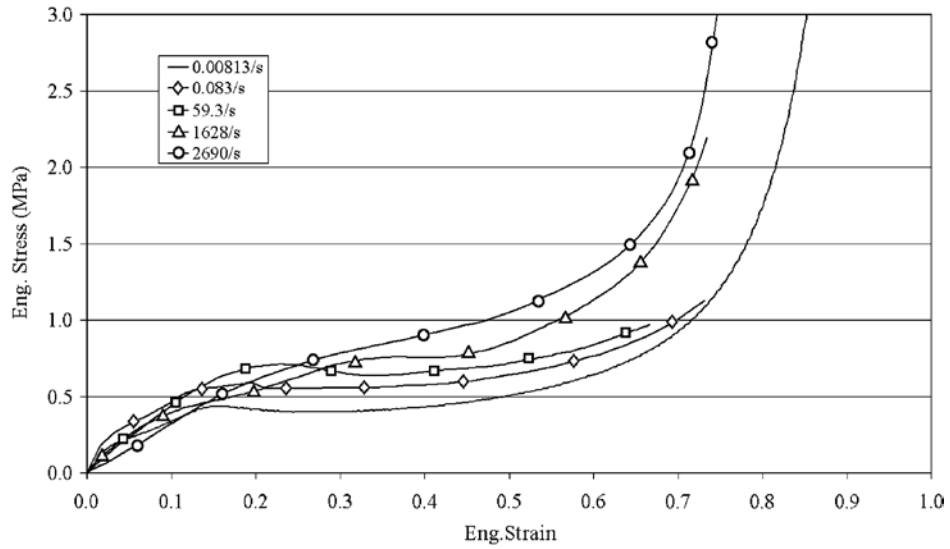

Figure 5.8: Stress strain curve of HDPE foam at various strain rates (adapted from Ouellet et al. 2006)

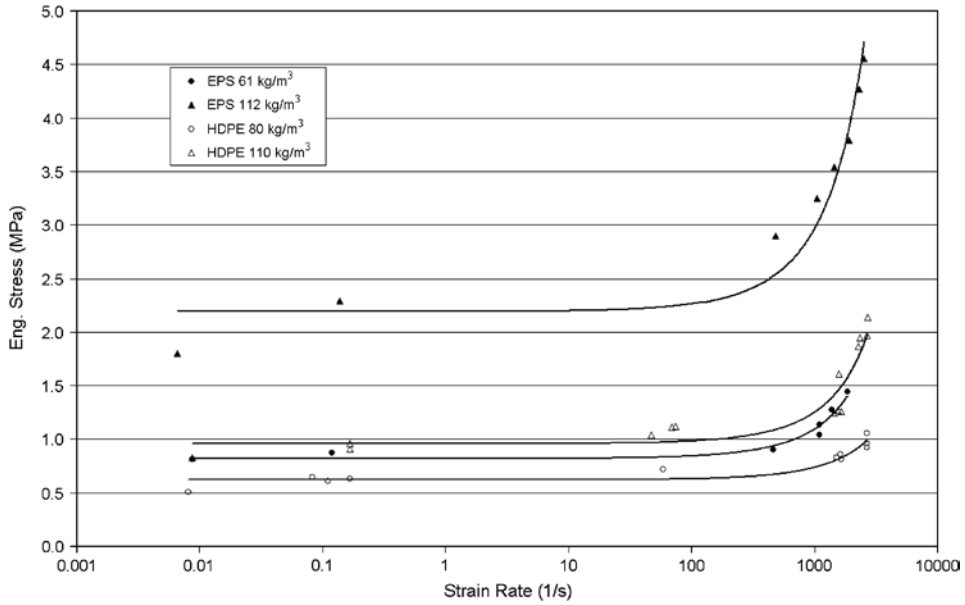

Figure 5.9: Rate dependency of various foams (adapted from Ouellet et al. 2006)

The material properties for some common foams are summarized in Table 5.2, based on data and analysis conducted by Thom [Thom 2009].

Table 5.2: Material properties of common foams (adapted from Thom 2009)

Foam Type	Name	Density (kg/m3)	Elastic Modulus (kPa)
Low density polyethylene	LDPE 45	45	320
High density polyethylene	HDPE 80	80	2 720
High density polyethylene	HDPE 110	110	8 000
Low density polyurethane	LDPU 37	37.2	23.4
Expanded polystyrene	EPS 61	61	10 400
Expanded polystyrene	EPS 112	112	52 700
Rigid polyurethane	PU 6708	128	22 000
Rigid polyurethane	PU 6712	192	57 700
Rigid polyurethane	PU 6715	240	71 900
Rigid polyurethane	PU 6718	288	114 000

5.4 Effects of Helmets on Blast

As blast induced mild traumatic brain injury gained prevalence as a clinical issue, many studies have investigated the effects of helmets and different helmet configurations on the potential for injury in blast. Dionne et al. [Dionne et al. 2002] exposed anthropomorphic mannequins to various blast overpressures in a free field environment and compared the head kinematics of unprotected mannequins to mannequins outfitted with the Med-Eng EOD-8 helmets. The presence of the helmet reduced the peak head accelerations from 78 – 84% depending on the initial charge size. Furthermore, the presence of the helmets significantly reduced HIC values.

Moss et al. [Moss et al. 2009] used a finite element model of a simplified head and helmet and found that the presence of a helmet can significantly affect the blast wave interaction with the head. They found that without lining in the helmet, the air gap between the head and the inside face of the helmet allowed pressure wave reflections which amplified pressures acting directly on the skull. This phenomenon is known as the ‘underwash’ effect. They concluded that the addition

of foam lining reduces this effect, but increases the kinematic loading on the head due to mechanical coupling of the head and helmet together.

Grujicic et al. [Grujicic et al. 2010a] used a one dimensional finite element model with adjacent layers of elements representing the various tissue and helmet layers, to investigate blast mitigation behaviour of various materials. They found that different foams had minimal impact at moderate blast loads, but polyurea foams substantially reduced peak loadings in the brain at higher blast loads. The same group also used a three dimensional head model with the ACH helmet, and concluded that the ACH provides some level of protection against mTBI, and that the protection increases with increased blast incident overpressures [Grujicic 2011].

Jason [Jason 2010] investigated the ACH geometry on intracranial pressures resulting from blast wave interaction with the head using a three dimensional finite element head model based on the DVBIC model (described in Section 6.4). This study found that the ACH did not block the main pathways of wave transmission into the brain, and thus the intracranial pressure mitigation was minimal. However, the presence of a faceshield in their simulations prevented initial wave transmission into the head, although allowed for reflections behind the faceshield later in time. Similar conclusions were reported by Nyein et al. [Nyein et al. 2010].

Panzer et al. [Panzer et al. 2010] used a plane-strain model of the transverse section of the head to investigate the role of helmet protection with various foam materials to blast mitigation. The findings concluded that a helmet with foam lining can reduce pressures and accelerations in the head, but can increase strains. Furthermore, lower density foams resulted in lowest pressures, while crushable foams resulted in lowest head accelerations.

Thom [Thom 2009] used one-dimensional finite element models to examine the effects of foams on blast wave mitigation. This analysis concluded that low impedance foams can reduce peak pressures from a blast wave, increasingly so at greater thicknesses. Furthermore, in cases where a hard plate is mounted to the foam, the blast wave could either be reduced or amplified depending on the permeability and areal density of the plate.

Ganpule et al. [Ganpule et al. 2012] used a three dimensional tetrahedral finite element model to investigate helmet protection in blast, and concluded that the underwash effect can result in greater reflected pressures at the rear of the head in helmets with no lining, although these pressures are still lower in magnitude than the initial reflected pressures at the front of the head during blast wave impingement. Their model suggested that tight foam pads can reduce this effect. In a more comprehensive study using this same model, Ganpule [Ganpule 2013] remarks that the blast pressure field around the head in primary blast is complex and non-uniform, and that small differences in surface geometry and curvature can significantly affect the flow dynamics and resultant loads. Additionally, significant differences in head response was found with differing head orientations.

Lockhart et al. [Lockhart et al. 2014] used a previous version of the sagittal model used in this study to investigate the kinematics of the head with a helmet and various foams, and found that a helmet with an optimized foam lining resulted in the greatest reduction of head acceleration and HIC_{15}, as compared to an unprotected head or a helmet with no lining.

In summary, a number of researchers have investigated the effects of helmets and different helmet configurations on the loadings experienced by the head in blast scenarios. The majority of these studies use finite element models that, while having the benefit of three dimensional geometries,

consist of elements too coarse to provide an accurate understanding of the brain tissue response (with some exceptions as discussed in the preceding paragraphs). Consequently, the focus in the literature in terms of evaluating helmet protection has been on metrics of global head kinematics. The consensus in the literature seems to be that the presence of a helmet generally reduces the head acceleration, and the presence of foam lining inside the helmet offers additional reduction. The effects of helmet protection on intracranial pressure has been investigated to a lesser degree, with the primary conclusions being that a helmet without a visor does not offer any significant ICP mitigation.

6. Review of Finite Element Modeling

Numerical models of biological tissues have been used since at least 1980, when Ward et al. [Ward et al. 1980] developed a finite element model of the human head to evaluate blunt impact loading to the head and brain. Since then, there has been much research and progress of detailed imaging techniques to advance the understanding of anatomical geometries, improved material characterization of the various tissues of the human body, and improved computational capabilities. These advances have allowed the quality of numerical models to steadily improve over the years.

This chapter will overview the basic concepts behind numerical modeling with a focus on blast, mesh convergence theory, constitutive modeling, and discuss some existing finite element models in the literature.

6.1 Finite Element Analysis Overview

Finite element analysis (FEA) is a numerical technique used to analyze the stress behaviour of complex structures computationally. FEA simplifies a complex structure by dividing it into simple geometric elements, joined by shared nodes, which are analyzed concurrently. In general, finite element analyses calculate approximate solutions to differential equations with specified initial and boundary conditions.

The two most common element types are 8-noded hexahedral (cubic) elements, and 4-noded tetrahedral elements. Hexahedral elements are generally considered to be superior compared to tetrahedral elements due to their robustness, although many models in the literature use tetrahedral

elements due to their ease of meshing complex geometries. In applications where hydrostatic effects are dominant, such as blast, tetrahedral elements can suffer from hydrostatic locking, whereby the elements exhibit non-physical stiffness due to artificial volumetric constraints [Bonet 1998].

An important concept of finite element modeling are the ideas of verification and validation [ASME 2006]. Verification of a model is simply verifying that the model is behaving correctly according to the inputted or defined parameters. In other words, there are no erroneous numerical errors or incorrectly defined values that are affecting results. This includes things like unsuitable material models, element formulations, and element sizes. A model should always be verified to confirm that it is behaving in the way that would be expected. On the other hand, model validation is comparing the results of a model to an experimental or theoretical value. The validation of a finite element model to experimental values is one of the most important concepts in numerical modeling, as it the only way to prove that the model is accurately simulating the real world scenario in question.

Both implicit and explicit formulations can be used in finite element methods. Implicit formulations use a global stiffness matrix that is solved simultaneously, whereas explicit formulations use an iterative approach for solving a series of partial differential equations at each time step. There are advantages and disadvantages to both implicit and explicit methods. Generally, implicit methods are used for quasi-static load cases, since the global stiffness matrix approach does not require iterations for every time step, and quasi-static problems can have large values of time to solve over. On the other hand, explicit methods are well suited for dynamic problems with large deformations or movements and relatively short duration. For the purposes

of this work in primary blast modeling, explicit finite element formulations are most suitable. The iterative process of calculations that an explicit code undertakes at each time step is illustrated in Figure 6.1.

LS-DYNA is an advanced multi-physics simulation explicit finite element software package widely used in complex non-linear and dynamic modeling situations. It was originally developed at the Lawrence Livermore National Laboratory in 1976 to model nuclear bomb effects, and underwent numerous updates over the years to add functionality. In 1988, the Livermore Software Technology Corporation (LSTC) was formed to continue developing and maintaining the software package, which is now called LS-DYNA. Currently, LS-DYNA is used in many industries including automotive, defence, aerospace, construction, and bioengineering.

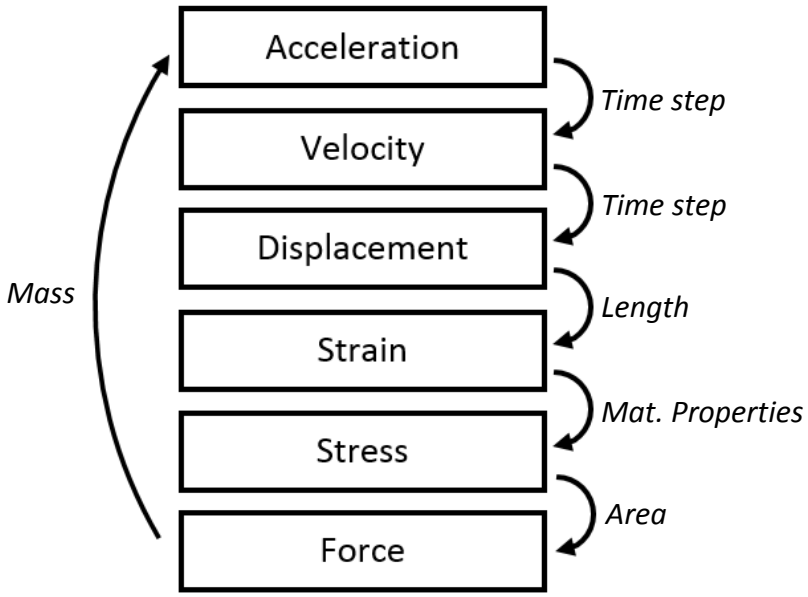

Figure 6.1: Iterative approach for explicit finite element method at each time step

6.2 Arbitrary Lagrangian Eulerian (ALE) Formulation

Numerical modeling of fluids, such as air, is typically associated with computational fluid dynamics codes, which use Eulerian control-volume principles. However, these codes generally do not have the capability to model deformation behaviour of solid materials such as brain tissue, which is a requirement for modeling blast injury. Consequently, alternative methods must be found to model blast waves using Lagrangian (control mass) based finite element codes. One method of doing this is using an Arbitrary Lagrangian Eulerian (ALE) formulation, which is an algorithm that allows Lagrangian elements to be treated as control volume through continuous remapping during each time step [Souli et al. 2004]. Furthermore, this method allows for coupling with fully Lagrangian elements to achieve a fluid structure interaction model. The ALE formulation in LS-DYNA has been widely used in the literature for modeling air shock waves and interaction with structures including the human body [Greer 2006, Cronin et al. 2008, Thom 2009, Lockhart 2010, Panzer et al. 2010].

The ALE formulation works by performing an advection, or remapping, step after each Lagrangian time step. The advection step removes mesh distortion by moving the nodes of the ALE elements back to their original positions, while keeping any distorted material at the new position. The way that this algorithm is implemented in LS-DYNA, prevents any material from being transferred diagonally through the mesh, so only material that is normal to the element sides is transferred (Figure 6.2). This is an important consideration when creating a mesh that uses this formulation, in that the mesh should minimize diagonal edges perpendicular to the wavefront.

Another important consideration in using the ALE formulation to model a fluid structure interaction is the element size. The element sizes of the Lagrangian and the ALE elements should

be comparable, or the coupling could result in numerical errors [Hallquist 2006]. The ALE formulation is well suited to simulating blast waves in air, since this method can account for the large distortions in the air caused by the shock wave through the remapping of elements.

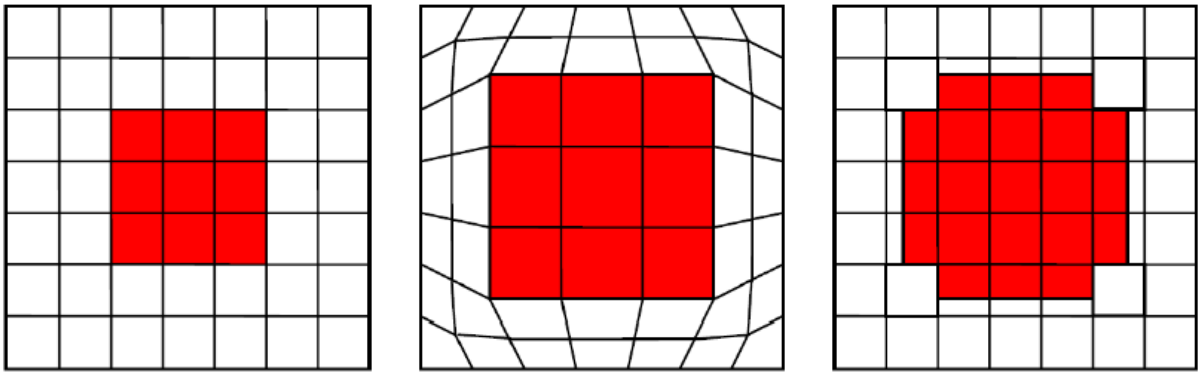

Figure 6.2: Illustration of ALE remapping concept (Adapted from Thom 2009)

6.3 Mesh Convergence Theory

Achieving mesh convergence is critical in finite element modeling to produce useable results. If the element size is too coarse relative to the detail in the geometry and applied loading/boundary conditions, the model may not be able to accurately predict stresses and strains, which can lead to erroneous conclusions. Furthermore, different measures of the model response can require different levels of mesh refinement. For example, it may require a finer mesh to achieve convergence for nodal velocities, compared to element stresses. So the level of mesh refinement necessary also depends on the specific metric or metrics that are relevant to the application. The general principle of mesh convergence is to refine the mesh until the difference between predictions results in an acceptable level of error. However, a formalized mathematical method of

determining mesh convergence is the Grid Convergence Index (GCI) and the Richardson extrapolation method.

The GCI has been proposed as a standard way of measuring mesh convergence in numerical models [Roache 1998]. The basis behind this method is the assumption that the results of the model approach a 'true' value asymptotically as the mesh is refined. By comparing the results of three meshes with different element sizes, an exponential relationship between element size and model prediction can be generated, and used to determine the degree of convergence. To use the GCI method, the order of convergence, *p*, must be calculated (Equation 6.1).

Order of convergence:

$$p = \frac{\ln\left(\frac{f_3 - f_2}{f_2 - f_1}\right)}{\ln(r)}$$

Equation 6.1 [Roache 1998]

where,

f_1, f_2, f_3 = the model results for fine, medium and coarse meshes respectively

r = the grid refinement ratio (i.e. r = 2 when the element sizes are halved for fine mesh to medium mesh and from medium mesh to coarse mesh)

Once the order of convergence is known, the Grid Convergence Indexes can be calculated for the fine to medium and medium coarse meshes (Equations 6.2 and 6.3). These equations also include a factor of safety, F_s, which is recommended to be 1.25 for a high confidence level in a three mesh analysis [Roache 1998].

GCI fine to medium: $$GCI_{12} = \frac{F_s\left(\frac{f_2 - f_1}{f_1}\right)}{r^p - 1}$$ *Equation 6.2*

GCI medium to coarse: $$GCI_{23} = \frac{F_s\left(\frac{f_3 - f_2}{f_2}\right)}{r^p - 1}$$ *Equation 6.3*

Using these GCI values, it can be determined if the results are in the asymptotic regime if the following condition (Equation 6.4) is valid.

Asymptotic regime condition: $$GCI_{23} \approx r^p GCI_{12}$$ *Equation 6.4*

If the asymptotic regime condition is true, then the results of the medium mesh size can satisfactorily be deemed to be in the asymptotic region of the response, and therefore that mesh size is appropriate for the model and response metric being analyzed [Roache 1998]. The GCI method is a useful tool for quantifying the mesh convergence of a numerical model, and should be used in finite element modeling to determine the possibility or likelihood of model results being determined by mesh coarseness instead of application-specific physics.

6.4 Constitutive Modeling

Constitutive modeling is a vitally important part of finite element analysis, and defines the relationship between strain, strain rate, and stress in the elements. A common occurrence in finite element modeling is an overemphasis on geometrical detail at the expense of appropriate constitutive models. It is therefore imperative to thoroughly investigate and verify the constitutive properties used in a finite element model, to have any sort of confidence in the values that the model outputs.

A constitutive equation is one that relates a material's response, or deformation, to some applied load. One of the simplest constitutive models in the linear elastic model, $\sigma=E\varepsilon$, which assumes a linear stress-strain relationship governed by the elastic modulus. Real world materials however are generally more complex and require more complex equations, such as hyperelastic where the stress-strain response in non-linear, or viscoelastic where the stress-strain response changes with rate.

Materials that exhibit rate dependency require constitutive equations capable of modeling viscoelasticity, and are generally characterized by their stress relaxation and creep behaviour. Stress relaxation is measured using a constant applied strain and observing the degradation of stress in the material, while creep behaviour is measured by applying a constant stress and observing the deformation of the material over time. A general formulation for a viscoelastic constitutive model is the general linear viscoelastic model (Equation 6.5) based on the Maxwell spring-damper system summed in a series.

General Linear Viscoelastic Model:

$$\sigma(t) = \int_0^t \frac{\partial \varepsilon(\tau)}{\partial \tau} G(t-\tau) d\tau$$

$$G(t) = \sum_{i=1}^{n} G_i \exp(-\beta_i t)$$

Equation 6.5 [Christensen 1982]

Where σ is stress, ε is strain, G is the shear modulus, β is a decay constant, τ is a time constant, and t is time. The general viscoelastic model assumes linear viscoelasticity, where the long-time stress-strain relationship is linear. An example of this linearity is shown in Figure 6.3, where each numbered set of stresses and strains are experimentally determined values in stress relaxation tests. Typically, viscoelastic linearity is a reasonable assumption at small deformations. At high

deformations, more complex non-linear viscoelastic relationships would be required. [Hallquist 2006]

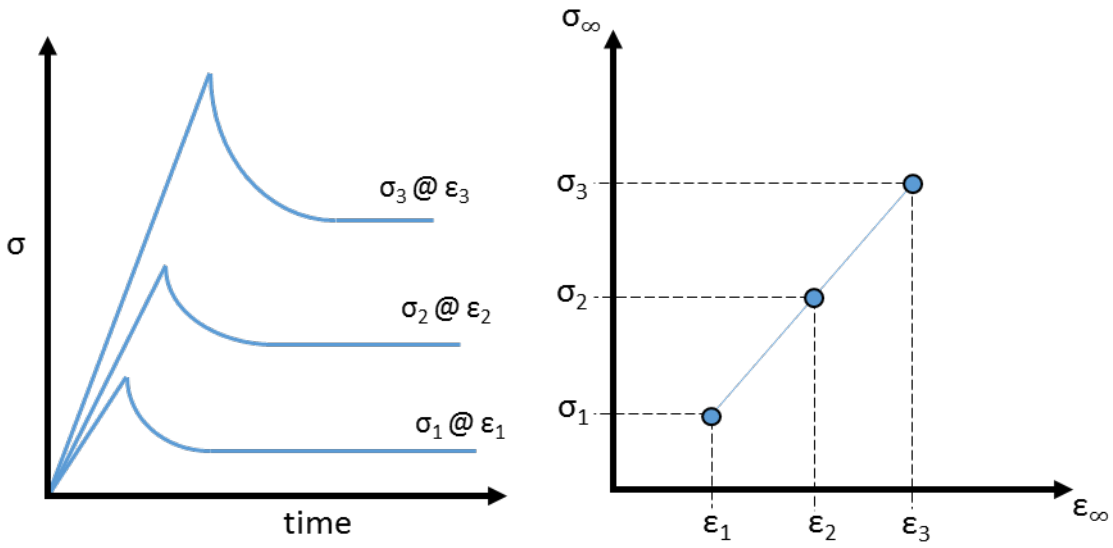

Figure 6.3: Example of linear viscoelasticity (adapted from Cronin ME 720 Section 7.4)

Some constitutive models also require equations of state to be defined. An equation of state is a mathematical relationship that relates the pressure, volume, and internal energy of a material. This relationship is required for a material to undergo shock, as shock waves require compressibility of the material that is defined by a non-linear pressure-volume curve where *dP/dV* increases with increasing pressure. In other words, for a material to undergo shock, it needs to have a non-constant bulk modulus that allows the wave speed to increase as the material is compressed. This allows pressure waves to travel faster along pre-compressed material and create a shock front. Thus, a material that does not have an equation of state that defines the non-linearity of the bulk modulus, cannot exhibit shock behaviour.

One of the simpler equations of state is the ideal gas law (Equation 6.6), which is a simplified form

of a linear polynomial equation of state (Equation 6.7).

Ideal Gas Law:

$$P = \rho(C_p - C_v)T$$
$$C_p = C_{p0} + C_L T + C_Q T^2$$
$$C_v = C_{v0} + C_L T + C_Q T^2$$

Equation 6.6

where P is pressure, ρ is density, T is temperature, C_p and C_v are constant pressure and volume heat capacities defined by the quadratic equations with constants as shown.

Linear Polynomial Equation of State:

$$P = C_0 + C_1\mu + C_2\mu^2 + C_3\mu^3 + (C_4 + C_5\mu + C_6\mu^2)E$$

Equation 6.7

where P is pressure, μ is $(\rho/\rho_0\text{-}1)$, C_0 to C_6 are constants, and E is energy.

Another commonly used equation of state is the Mie-Gruneisen formulation (Equation 6.8), which is based on statistical mechanics and internal energies of atoms.

Mie-Gruneisen Equation of State:

$$P - P_0 = \frac{\gamma}{V}(E - E_0)$$

$$\rho = \frac{\rho_0 C^2 \mu \left[1 + \left(1 - \frac{\gamma_0}{2}\right)\mu - \frac{a}{2}\mu^2\right]}{\left[1 - (S_1 - 1)\mu - S_2 \frac{\mu^2}{(\mu+1)^2}\right]^2} + (\gamma_0 + a\mu)E$$

$$\rho = \rho_0 C^2 \mu + (\gamma_0 + a\mu)E$$

Equation 6.8 [Meyers 1994]

where P is pressure, V is volume, E is energy, ρ is density, C is the acoustic wave speed, μ is $(\rho/\rho_0\text{-}1)$, γ is a constant called the Gruneisen Gamma, and a, S_1, and S_2 are constants.

6.5 Summary of Existing Models

There have been numerous automotive finite element models that have been developed to simulate and predict head injuries caused by automotive impact scenarios. These models include the GHBMC model [Gayzik et al. 2012], the THUMS model [Ipek et al. 2009], the SIMon model [Takhounts et al. 2008], and the WSUBIM model [Zhang et al. 2004]. Generally, these automotive or blunt impact models were developed specifically for the regimes of loading relevant to crash impacts and subsequent modes of injury, and thus are limited in their applicability to blast head models. However, some aspects of the model development such as constitutive models and material properties can be relevant. Of more relevance to the current work are the existing models that have attempted to simulate blast loadings to the head, which are discussed in the following paragraphs.

El Sayed et al. [El Sayed et al. 2008] developed a 3D finite element head model to simulate impact related traumatic brain injuries. The model consists of 39 047 tetrahedral composite elements. The brain was modeled using a combination of viscoelastic and elastoplastic models to account for both permanent and transient deformation. Grey matter, white matter, the brain stem, and the corpus callosum were distinguished in this model.

Cronin et al. [Cronin et al. 2008] used a transverse blast head model coupled to an air mesh to investigate tissue response in blast. The brain and CSF, skull, eyes, and soft tissue were differentiated. Furthermore, this model utilized solid hexahedral elements, and demonstrated mesh convergence. Increasing blast load severity was shown to result in greater pressures in the brain tissue.

The United States Defence and Veterans Brain Injury Center (DVBIC) developed a three dimensional model of the brain and surrounding tissue to evaluate blast loading to the brain [Moore et al. 2009]. It was composed of 808 766 tetrahedral elements. The volumetric response of the brain tissue was described by a Tait equation of state with parameters adjusted to fit the bulk modulus of the various tissue types.

Taylor et al. [Taylor 2009] developed a 3D voxel model of the brain and skull for simulating blast-induced wave effects in the brain. This model consisted of 6 850 560 voxels of 1 mm^3 size. In this model, the grey matter and white matter were considered to be compressible viscoelastic materials. Although the voxel approach to geometry provides a high resolution, it is limited in its ability to model tissue interfaces, since the voxels cannot conform to anatomical curvatures.

Chafi et al. [Chafi et al. 2010] developed a 3D finite element model for evaluating blast loading to the brain. Their model consisted of 27 971 solid hexahedral and membrane elements. The size of the elements varied from 1 mm to 6 mm. A hyper-viscoelastic constitutive model was used to model the brain under the assumptions that the brain behaves as a homogeneous and isotropic material.

Panzer et al. [Panzer et al. 2010] developed a planar finite element model for evaluating blast injury. The model is of the head and brain in the transverse plane, and consisted of 7 650 hexahedral elements with an average characteristic length of 1.5 mm. All brain tissue was modeled using the same linear viscoelastic model, with no distinction between brain tissue types.

Roberts et al. [Roberts et al. 2012] developed a finite element model of the human head and neck, based on a human surrogate model to investigate blast head injury. This model consisted of

130 000 hexahedral, tetrahedral, shell, and beam elements, and included parts to represent the face, skull, brain, brainstem, and a Hybrid III neck. An average element size was not reported for this model. The brain was modeled homogeneously as a viscoelastic material.

Grujicic et al. [Grujicic et al. 2010b] developed a finite element blast head model using 40 000 tetrahedral elements, that included the cerebrum, cerebellum, CSF, brainstem, pituitary gland, and the skull. The typical element size in this model was 3 mm, and authors note that the use of finer meshes produced different numerical quantities, which indicates a lack of mesh convergence. The model was used in a later study to investigate the effect of protection (combat helmet) on the response of the head [Grujicic et al. 2011]. The helmet mesh size was similarly on the order of 3mm.

In summary, there have been many important contributions to blast injury modeling in the literature, including investigations using three-dimensional head models. However, the current three-dimensional blast head models are limited in a number of ways, primarily due to the complex geometry of the tissues which makes achieving an appropriate quality mesh challenging. This challenge has been addressed in the literature using the following approaches, but with limitations.

Many three-dimensional models are meshed with element sizes that are considered too coarse for blast analysis which limits the predictive capabilities of these models. Coarser meshes are not convergent and will provide inconsistent response predictions, a limitation that is acknowledged in many of the studies utilizing coarse elements. Numerical models that do not achieve mesh convergence can be used in a limited capacity parametrically, but their predictions are not indicative of the actual loading. Properly refined three-dimensional finite element meshes are not impossible to achieve, but are computationally prohibitive if they will be used for meaningful

analysis.

Full three dimensional models often contain gaps in the mesh/model resulting from areas where tissues and tissue interfaces may have very small dimensions relative to the element size, or where tissues may terminate in triangular shapes, which cannot be easily meshed with hexahedral elements. When response is primarily related to the transmission of waves, as is the case over the short time frames associated with primary blast loading, a lack of mesh continuity will result in incorrect results due to artificial internal wave reflections. Gaps in the model when meshing with hexahedral elements can be addressed by meshing using a voxel approach similar to Taylor et al. [Taylor et al. 2009], which is conducive to subject scan data; however, this results in faceted boundaries between tissues which will affect wave transmission, and will over or underrepresent tissues in areas where two tissues meet. Moreover, stepped interfaces will provide physical locking between tissues that inhibits relative sliding motion. Some of the above limitations in meshing complex shapes can be addressed using tetrahedral elements; however, these elements are well-known to exhibit hydrostatic locking which incorrectly predicts pressure and therefore affects wave transmission through the mesh [Belytschko 2000].

The development of finite element blast head models to investigate primary blast injury, which address some of the limitations of existing models, are discussed in detail in the following chapter.

7. Sagittal and Transverse Models

The finite element blast head models used in this study are fully coupled models in the sagittal and transverse planes of the head. These models were developed for the purpose of evaluating human brain tissue response to primary blast loading. The coupled sagittal and transverse models are capable of simulating a blast pressure wave interaction with the head, and measuring the resultant head kinematics and tissue stresses and strains. These are planar models in two perpendicular planes, because full three dimensional models with the required mesh resolution are computationally challenging, particularly for larger scale parametric studies.

Finite element models have three general components: geometry, constitutive models, and boundary conditions, each of which will be covered in the following subsections. The models were validated against relevant experimental data, the results of which are also discussed in this chapter.

7.1 Model Geometry

Due to the fine mesh resolution required in blast models, full three dimensional models become computationally prohibitive. This is further compounded by the necessity of mesh continuity between the tissue structures to prevent any gaps which would impede wave transmission. The computational challenges present in developing a full three dimensional blast head model led to the development of sagittal and transverse planar models, which provide a fully coupled fluid-structure analysis with the required mesh resolution while remaining computationally feasible to

enable larger scale parametric studies. The models consist of a single layer of solid hexahedral elements in the sagittal and transverse planes.

The geometry of the models was guided by images from the Visible Human Project, which is discussed in detail in Section 3.4. The VHP slices were used to identify the different tissue layers present in the head, and finite element meshes were generated for each of these (Figure 7.1). The sagittal model geometry was cut off at the neck to reduce the total number of elements in the model. Although this creates a non-physical interface at the neck, this is not anticipated to significantly affect pressure response at the brain tissue, nor the head kinematics since primary blast waves result in predominantly translational accelerations.

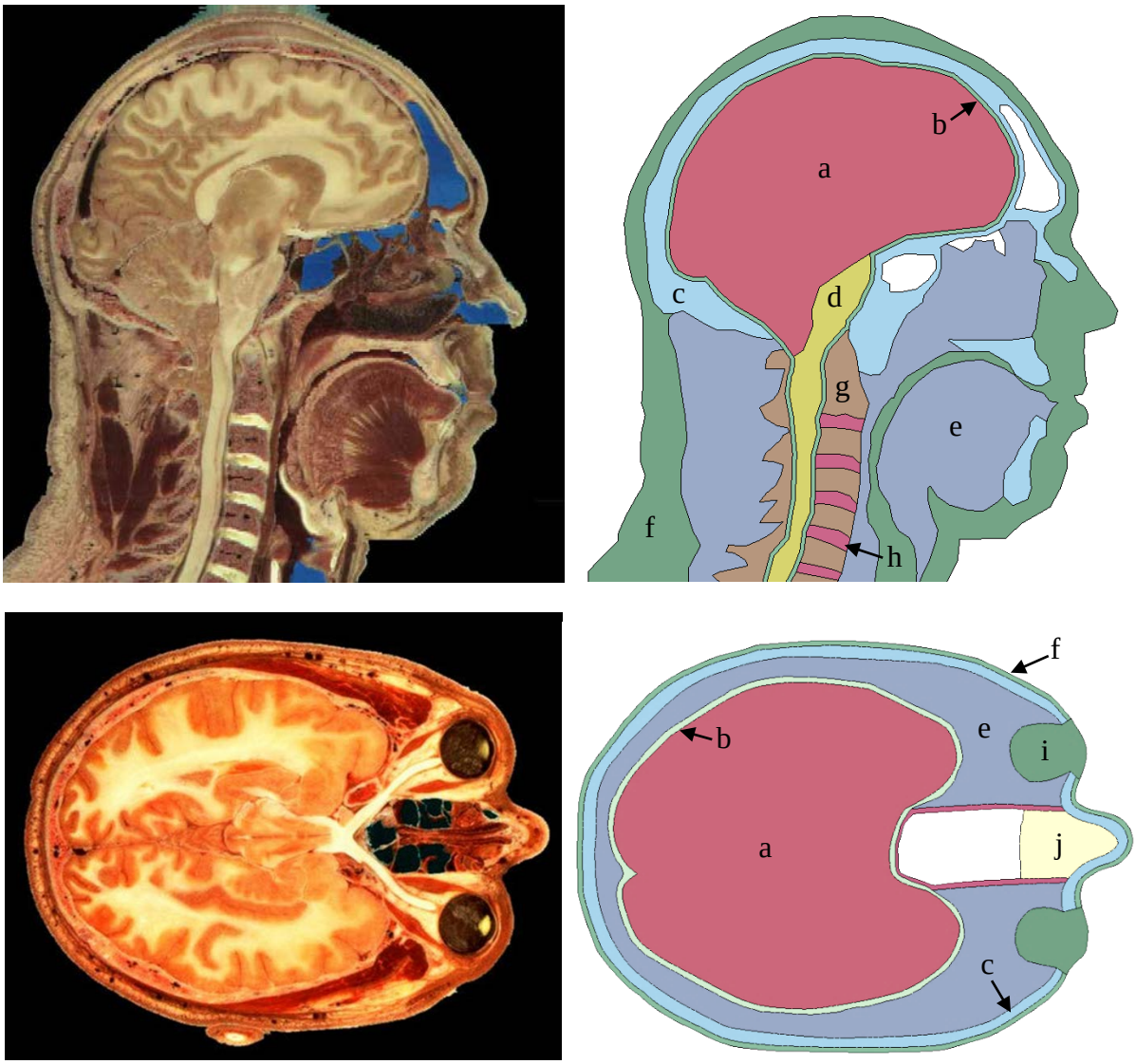

Figure 7.1: The Visible Human Project slice and FE head model for sagittal (top) and transverse (bottom), showing (a) brain, (b) cerebrospinal fluid, (c) skull, (d) spinal cord, (e) muscle tissue, (f) skin, (g) vertebrae, (h) vertebral discs, (i) eyes (soft tissue), and (j) sinus (soft tissue)

A critical parameter of a finite element model is the element size. A mesh convergence study must be done in order to verify that the model response is not governed by the mesh size. Lockhart performed a mesh convergence study of the sagittal model and determined that an element size of 1 mm was required to predict accurate kinematics, in agreement with similar studies in the literature [Panzer et al. 2011b, Lockhart 2010, Greer 2006]. A mesh convergence study using

intracranial pressure as the response metric was performed in the current work (Appendix A), and similarly concluded that a mesh size of 1 mm was necessary to achieve convergence. Thus, the sagittal and transverse models were meshed with an average element size of 1 mm (Figure 7.2).

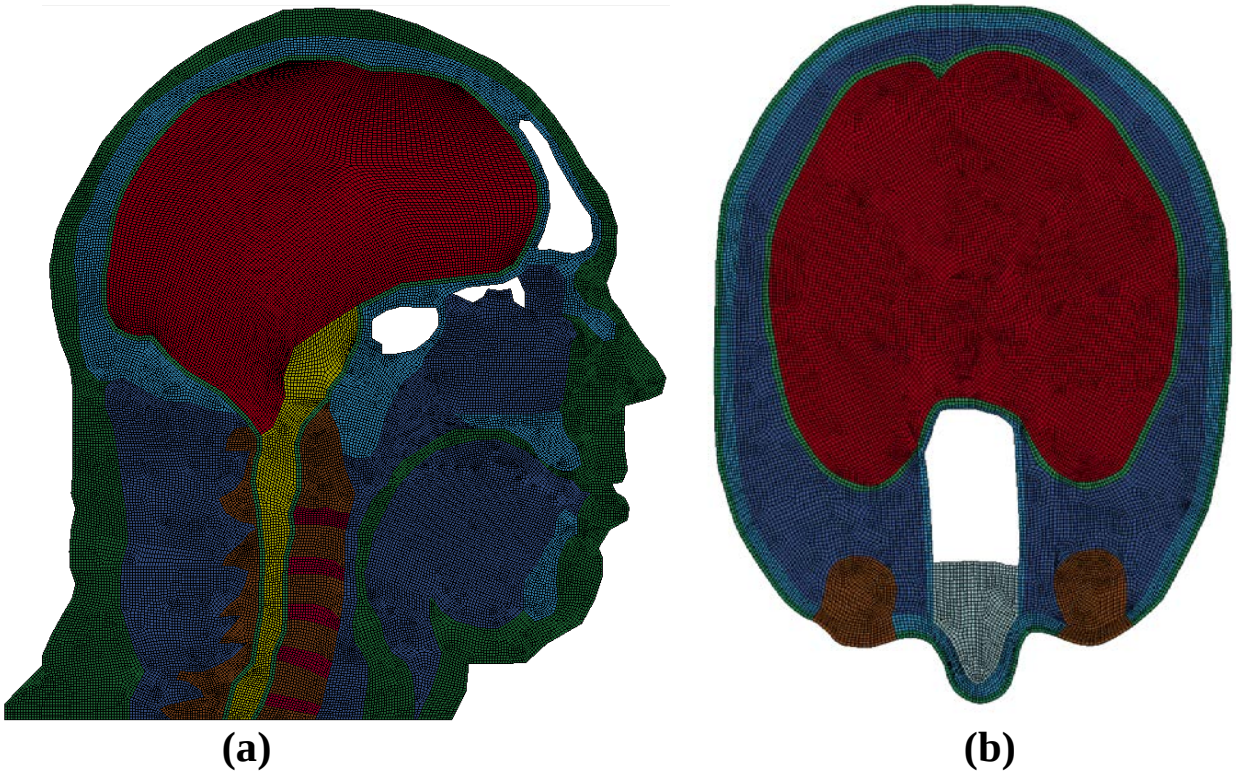

Figure 7.2: Finite element meshes for the (a) sagittal and (b) transverse geometries

While hexahedral elements are generally considered superior, many models in the literature use tetrahedral elements. To investigate the difference between these element types, the sagittal model geometry was meshed using both hexahedral and tetrahedral elements to compare the response. This investigation is included as Appendix B, and concluded that tetrahedral elements report nominally 300% greater pressures than hexahedral elements for the same applied blast load. Thus, solid hexahedral elements were used in the head models.

To ensure that the wave transmission in the tissues of the models was not impeded by the presence of any gaps, the nodes between adjacent tissue layers were merged. This approach preserves the material boundaries and the relative impedance between adjacent materials, and does not require a contact algorithm in order to transfer forces. This method does have the limitation of preventing significant sliding motion between tissues layers, which may be important near the CSF and brain interface during rotational loadings [Abney et al. 2010]. However, the short duration loading in primary blast makes it unlikely that there would be any large bulk motion of the tissues, especially rotationally since the blast wave is more or less a planar wave at the standoffs relevant for mTBI. This was found to be the case in the current study. Furthermore, previous studies that have compared different sliding and tied contact interfaces between the brain and CSF in blast load conditions found no significant difference in pressures or strains [Chafi et al. 2010]. In addition, although contact definitions are widely used in finite element modeling, many contact algorithms use scaling methods for interfaces with high and low impedance materials (such as the skull and brain), that may be dissipative under some circumstances [LS-DYNA Manual R7]. Therefore, ensuring accurate wave transmission in the models by merging nodes is a more important consideration than allowing for sliding motion to occur.

7.2 Boundary Conditions

In terms of the head model boundary conditions, the sagittal and transverse head models were constrained from out of plane rotation or translation, to prevent undesired nodal movements. In the sagittal model, the bottom layer of nodes at the neck were additionally fully constrained, to capture any rotational effects that may be caused by the neck and torso interface. Beyond these constraints, the models were free to translate and rotate in plane during the simulations.

To apply the blast load to the head models, an additional air mesh was required that could couple to the head models, carry the blast pressure wave, and apply the wave to the head models. The air mesh was modeled using an Arbitrary Lagrangian Eulerian (ALE) formulation in the finite element software LS-DYNA, as described in Section 6.2. The Lagrangian sagittal and transverse head models were embedded into the ALE air mesh, resulting in a fully coupled fluid/structure interaction. As mentioned in Section 6.2, the ALE air elements were capable of handling large deformation problems, which is ideal for blast where the air elements would experience significant distortion due to the air shock wave impinging on the head models. This method of ALE coupling allows for the complex reflections in the air around the geometries of the head to be modeled. Simpler models that do not include an air mesh cannot model these reflections, which are especially important in modeling helmets systems that can change the way the reflections interact with the head.

To facilitate accurate coupling of the ALE air elements with the head models, the size of the ALE elements is recommended to be of a similar characteristic length to the Lagrangian elements, which was 1 mm. Furthermore, the total size of the air mesh was required to be large enough to prevent any boundary reflections from interfering with the models. The final dimensions of the air mesh were 1.20 x 2.05 m (Figure 7.3). Maintaining a 1 mm sized air mesh for the entire area of the air mesh was computationally inefficient, so the air mesh was graded away from the head models to reduce the total number of elements. This method allowed for a computationally efficient air mesh, while maintaining the required air elements size in the vicinity of the head models to ensure accurate coupling (Figure 7.4).

Figure 7.3: Total size of air mesh used in the models

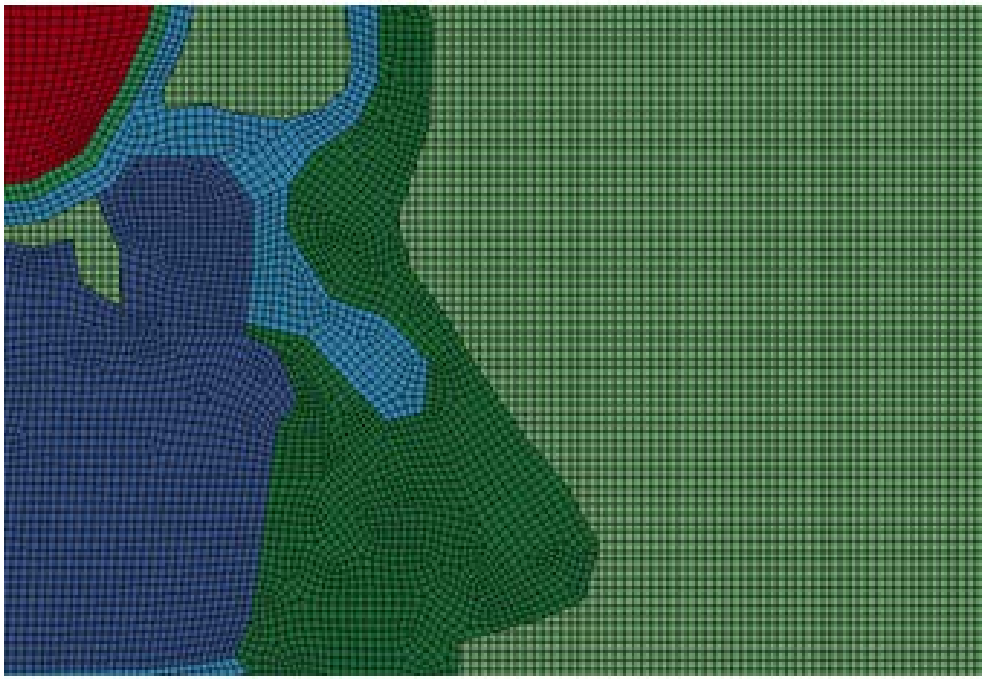

Figure 7.4: Air mesh and head model element size continuity

To actually apply the blast wave to the air mesh, specific volume and temperature boundary conditions were applied to the leading edge of the air mesh (Figure 7.5). In order to calculate the necessary specific volume and temperature histories for a particular blast load condition, a combination of the Conventional Weapons (CONWEP) equations and the Rankine-Hugoniot relations for air were used [Needham 2010]. The CONWEP equations were used to determine the pressure-time history for the blast case through LS-DYNA, and the Rankine-Hugoniot equations were used to convert the pressure-time history into specific volume and temperature (internal energy) histories. This step was necessary because the finite element software required these inputs to prescribe for boundary conditions on the elements. The specific volume and temperature in the elements was calculated and tracked through the defined equation of state. A sample calculation for this procedure of converting a pressure value to temperature and specific volume is shown in Table 7.1.

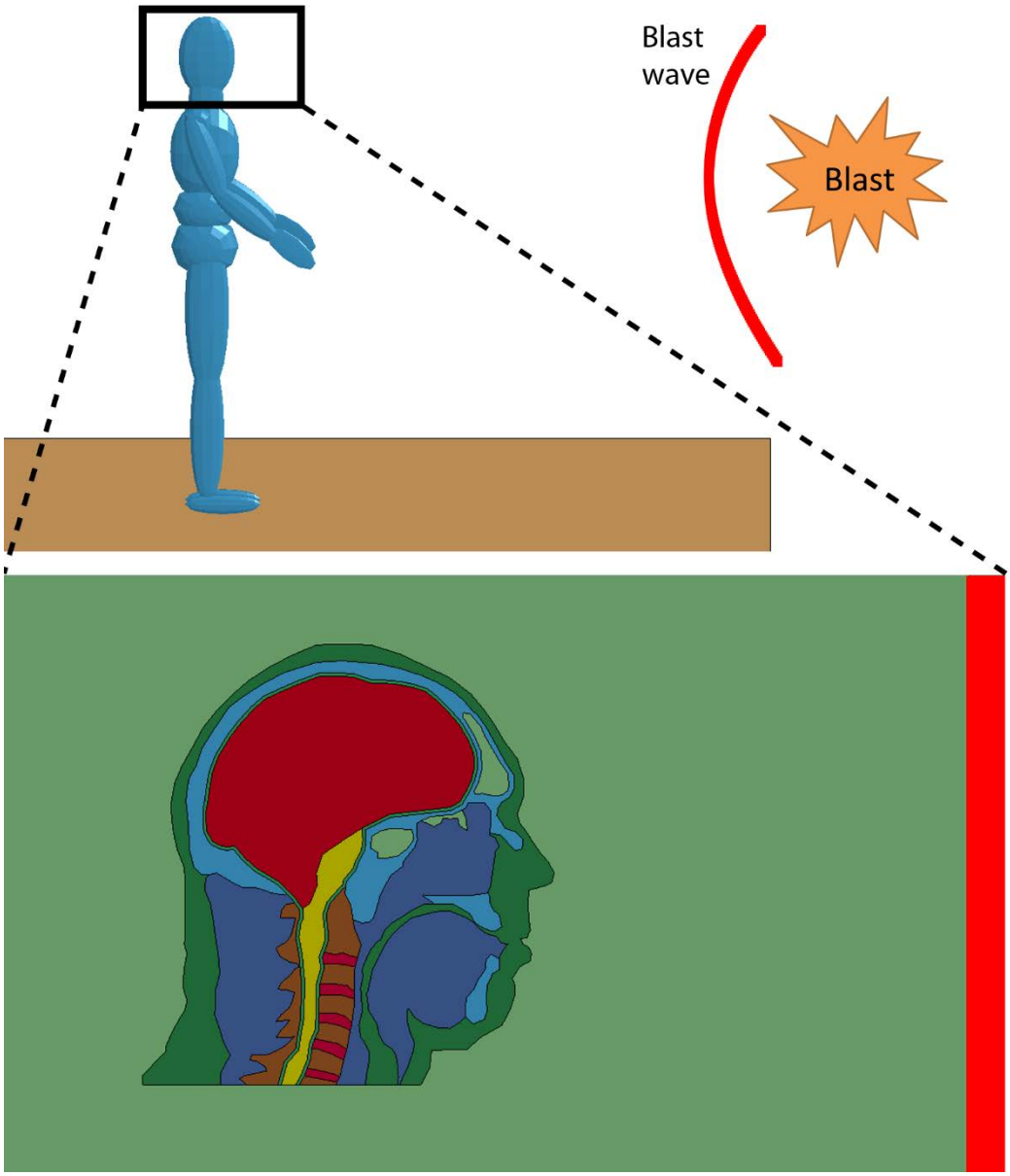

Figure 7.5: Schematic of blast load application

Table 7.1: Sample calculation for Rankine-Hugoniot conversion

Atmospheric Pressure	P_{atm}	*101 325*	*Pa*
Atmospheric Temperature	T_{atm}	*293*	*K*
Atmospheric Density	ρ_{atm}	*1.205*	*kg/m3*
Atmospheric Specific Volume	v_{atm}	*1*	
Pressure at a time step from CONWEP	P	*270 000*	*Pa*
Temperature	$= T_{atm}\left(\frac{7+\frac{P-P_{atm}}{P_{atm}}}{7+6\frac{P-P_{atm}}{P_{atm}}}\right)\left(1+\frac{P-P_{atm}}{P_{atm}}\right)$	= 398.2	K
Specific Volume	$= \left(\frac{7+\frac{P-P_{atm}}{P_{atm}}}{7+6\frac{P-P_{atm}}{P_{atm}}}\right)$	= 0.510	

The boundary condition method described in the preceding paragraph induces a pressure wave in the air mesh that can propagate through the mesh and interact with the embedded head models. Since the standoff distances that are relevant to mTBI are generally far enough away to escape the effects of the charge shape, the planar wave approximation was valid. This method of modeling blast events has been used in previous finite element studies [Singh et al. 2013, Panzer et al. 2012, Cronin et al. 2008, Greer 2006].

In selecting the specific blast load cases to be applied to the models, a representative set of loadings relevant to mTBI was selected for which experimental data was available. These cases were for 5 kg of C4 high explosive at 1.5 m height of burst, at standoff distances of 3, 3.5, and 4 m, which result in peak blast overpressures of 326, 230, and 170 kPa respectively. These specific load cases were chosen because they correspond to experimental tests conducted by DRDC Valcartier, the data for which could be used to help validate the results of the models. Ground interaction was not included in the pressure histories for the applied waves because the Mach stem triple point did

not affect the head for the charge size and standoff distances considered, as may be the case for larger standoffs [Haladuick et al. 2012].

The method of applying a blast load to the air mesh described above was used for these three load cases, and the resulting pressures in the air mesh (with no head models) was compared to the theoretical pressure curves (Figure 7.6). The ALE modeling method demonstrated good accuracy in simulating the peak pressures and durations in the air resulting from a blast.

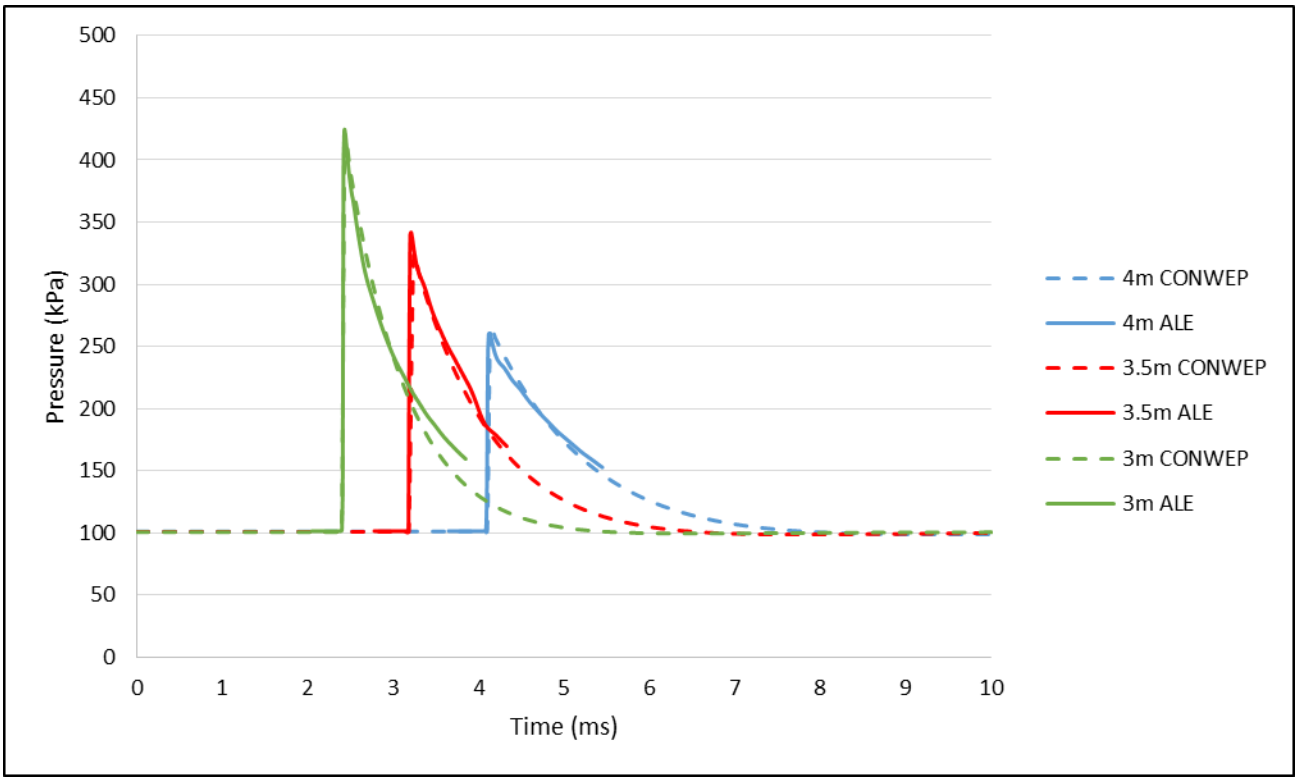

Figure 7.6: Pressure history comparison between ALE and CONWEP for three blast load cases

7.3 Constitutive Models

The air mesh was modelled using a viscous fluid material model (*MAT_NULL in LS-DYNA) that has no shear stiffness and no yield strength, and behaves in a fluid-like manner [LS-DYNA

Manual R7]. Combined with an ideal gas equation of state to govern the pressure and volume response, this provided a good representation of the ambient air in the blast model. The air material properties are summarized in Table 7.2.

Table 7.2: Material properties of air elements

Material Parameters		Ideal Gas Law Parameters				
Density (kg/m3)	**Dynamic Viscosity (Pa·s)**	**C_{V0}**	**C_{P0}**	**C_L, C_Q**	**T_0**	**V_0**
1.205	1.821e-5	717.86	1005	0	293.15	1.0

The different tissue layers present in the head models were assigned appropriate constitutive properties to govern their mechanical behaviours (Table 7.3). The skull, vertebral bodies, vertebral discs, and skin tissues were modeled as simple elastic models, with the material properties taken from the literature. Since primary blast is inherently wave dominated with large hydrostatic pressures, the most important parameters for the constitutive models are in the bulk response, and simple elastic constitutive models can represent this behaviour, particularly for the hard tissues that do not undergo any inelastic deformation for this type of loading. Furthermore, the tissues themselves are not expected to exhibit shock behaviour, as the loads necessary to induce shock waves in solid tissues are far beyond any that would be expected in scenarios relevant to mTBI. Failure models were not included for the bone materials because of the small expected deformations in the models in primary blast due to the short duration of loading.

The muscle tissue was modeled using a strain rate dependent simplified rubber model, which has been used in previous studies to model muscle tissue in similar finite element blast models [Lockhart 2010, Cronin et al. 2008]. The muscle tissue is defined by a series of uniaxial stress-strain curves for various strain rates which differentiate the compressive response of the material,

based on the work of van Sligtenhorst [van Sligtenhorst et al. 2006]. The cerebrospinal fluid was modeled using an elastic fluid material model, which uses a defined bulk modulus in lieu of the elastic modulus and Poisson's ratio, and offers no resistance to shear. The constitutive material properties of the tissues used in the head models are summarized in Table 7.3.

Table 7.3: Constitutive properties of different tissues used in the models (adapted from Lockhart 2010)

Tissue	**Material Model**	**Density (kg/m^3)**	**Poisson's Ratio**	**Young's Mod. (Pa)**	**Bulk Mod. (Pa)**
Skull/Vertebrae	Elastic	1561	0.379	7.92e9	
Vertebral Discs	Elastic	1040	0.40	3.4e6	
Skin	Elastic	1200	0.42	1.7e9	
Muscle/Soft Tissue	Hyperelastic	1050			2.2e9
CSF	Fluid	1040			2.2e9

7.3.1 Brain Tissue Constitutive Modeling

Since the main purpose of these models was to investigate the brain tissue response, the constitutive model for the brain tissue was a critically important parameter, which was guided by the physical properties of the brain as discussed in Section 3.3. Physically, brain tissue is hyper-viscoelastic, anisotropic, and heterogeneous with some degree of regional variation in mechanical properties. For the purpose of modeling this highly complex material, a number of simplifying assumptions must be made.

Firstly, regarding the hyperelastic and viscoelastic nature of the brain, the stress strain behaviour should be modeled as accurately as possible according to the available data, as that is what will govern the basic model response. As the rate of loading is a definitive important factor in blast (high rate of loading), viscoelasticity was necessary to include in the constitutive model. Although brain tissue has been reported to exhibit non-linearity in its viscoelastic response [Jin et al. 2013], the constitutive parameters available in the literature for the non-linear response

are highly limited. In contrast, a number of studies have reported on viscoelastic parameters of brain tissue assuming linear viscoelasticity [Zhang et al. 2001, Klatt et al. 2006, Hamhaber et al. 2007, Green et al. 2008, Takhounts et al. 2008, Ipek et al. 2009, Sack et al. 2009, Zhu et al. 2010a, Zhang et al. 2011b]. Therefore, a linear viscoelastic constitutive model was deemed appropriate for this study due to the availability of parameters in the literature and due to the anticipated low deformation over the duration of the event.

Secondly, regarding the anisotropic behaviour of the brain tissue. Anisotropy, while an important consideration, generally affects the strain behaviour of a material, as the fibre orientation will change how the material deforms. In primary blast loading, where the deformations are expected to be small, the effects of anisotropy should similarly be small. Since primary blast is dominated by pressure waves, and the wave transmission and reflection in the tissues is governed by the bulk properties, the presence of anisotropy in the constitutive equations will not greatly change the results. Furthermore, the degree of anisotropy and the fibre orientation mapping in the brain tissue has not been well characterized in the literature, so attempts to include anisotropy in the models would be largely based on conjecture. Therefore, the brain tissue was assumed to be isotropic in these models.

Thirdly, regarding the heterogeneity of the tissues. Brain tissue is divided into two main types of tissue, white matter and grey matter. Although the material properties of these two tissues are well known to exhibit different mechanical properties, there has been no investigation as to the differences in bulk modulus or bulk properties. Therefore, the acoustic impedance governed wave behaviour of the tissues would not be affected by a distinction between white and grey matter. For this reason, the brain tissue in the models was assumed to be homogeneous.

Based on the explanations above, the most appropriate constitutive model for the brain tissue was deemed to be a linear viscoelastic model, where the brain is treated an isotropic and homogeneous continuum. A linear viscoelastic constitutive model (*MAT_VISCOELASTIC in LS-DYNA) defines shear relaxation behaviour from Equation 7.1, where G_0 is the short-time shear modulus, G_∞ is the long-time shear modulus, and β is the decay constant.

$$G(t) = G_\infty + (G_0 - G_\infty)e^{-\beta t} \qquad \textit{Equation 7.1}$$

7.3.2 Initial Investigation and Results of Brain Tissue Variability

One of the challenges in modeling biological tissues is the large amount of variability present in experimental test of material properties, and the sensitivity to test methodology and material condition. Consequently, the available viscoelastic parameters in the literature for brain tissue vary widely (Table 7.4). To investigate the effect of these differing properties on the model results, the viscoelastic parameters from various literature sources were compared. In some cases, where the literature source presented different properties for different regions, the properties were averaged. For the purposes of comparing the viscoelastic parameters, this averaging was deemed acceptable because the total range of parameters considered was greater than the differences in regional properties reported by the authors.

Table 7.4: Viscoelastic parameters for brain tissue from the literature

Literature Source	Bulk Modulus (GPa)	Density (kg/m^3)	G_∞ (Pa)	G_0 (Pa)	B (s^{-1})
[Ipek et al. 2009]	2.20	1050	49000	16200	145
[Zhang et al. 2001]	2.19	1050	44333	7333	400
[Zhu et al. 2010a]	2.20	1050	15900	3600	504.5
[Takhounts et al. 2008]	2.20	1050	1662	928	16.95

The brain tissue was also investigated using a viscous fluid material model (*MAT_NULL in LS-DYNA). Such a material would give minimal resistance to dynamic shear, and therefore would result in maximum predicted strains for a particular load case. This provides an upper bound on the strains expected for a tested load case, which is essentially a very conservative estimate for the model strain response in blast. A Gruneisen equation of state was defined for the viscous fluid material with the properties of water taken from the literature (Table 7.5).

Table 7.5: Viscous fluid brain material properties

Density (kg/m^3)	1050
Dynamic Viscosity (Pa·s)	8.90e-4
Gruneisen EOS parameters [Tan et al. 2009]	C = 1483 S1 = 1.75 γ = 0.28

The sagittal and transverse models were analyzed using the 5 kg of C4 at 4 m standoff distance blast load case, using the blast load application method described in Section 7.2, for each of the viscoelastic parameters as well as the viscous fluid material for the brain tissue. The model response was compared in terms of peak first principal strain and effective strain rate.

The peak principal strain response in the brain tissue material increased in both the sagittal and transverse models as the shear modulus of the viscoelastic parameters decreased (Figure 7.7). The peak strains predicted by the models varied significantly, almost one order of magnitude, with the available viscoelastic parameters in the literature. This underscores the uncertainty present in the current understanding of brain tissue material properties. As expected, the viscous fluid material reported the greatest strains for both models. Interestingly, the maximum effective strain rates did not differ significantly for the different parameters, although the viscous fluid material resulted in slightly increased strain rates, more so for the transverse model

(Figure 7.8). There was also no significant difference (less than 0.1% difference) in peak intracranial pressures for the different brain tissue parameters, which is expected since the bulk properties are very similar between the sets of parameters.

All further simulations with these models used the parameters from Zhu et al. 2010a, which represent the median response of the range of parameters tested. This was deemed to be a reasonable compromise to determine the strain response of the models based on the currently available data.

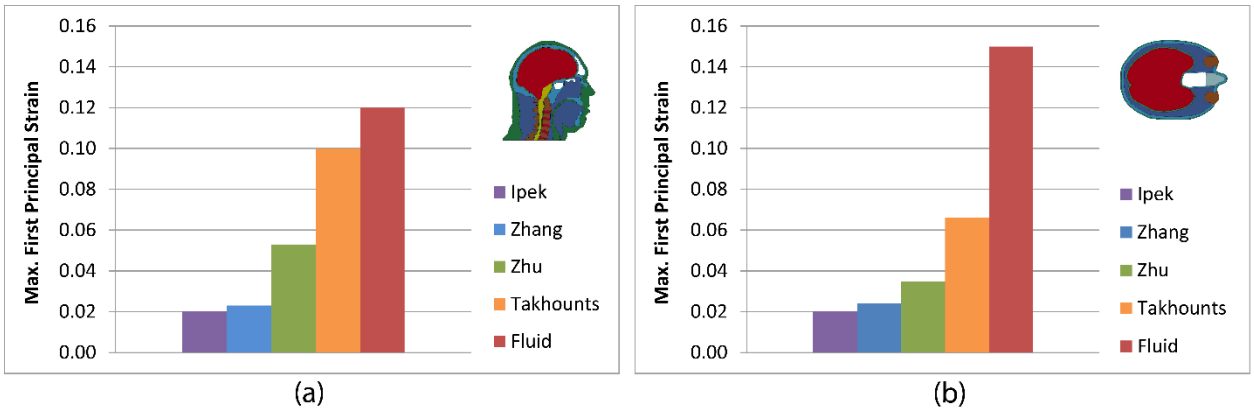

Figure 7.7: Comparison of peak first principal strains for various viscoelastic parameters for (a) sagittal and (b) transverse models for 5 kg of C4 at 4 m standoff

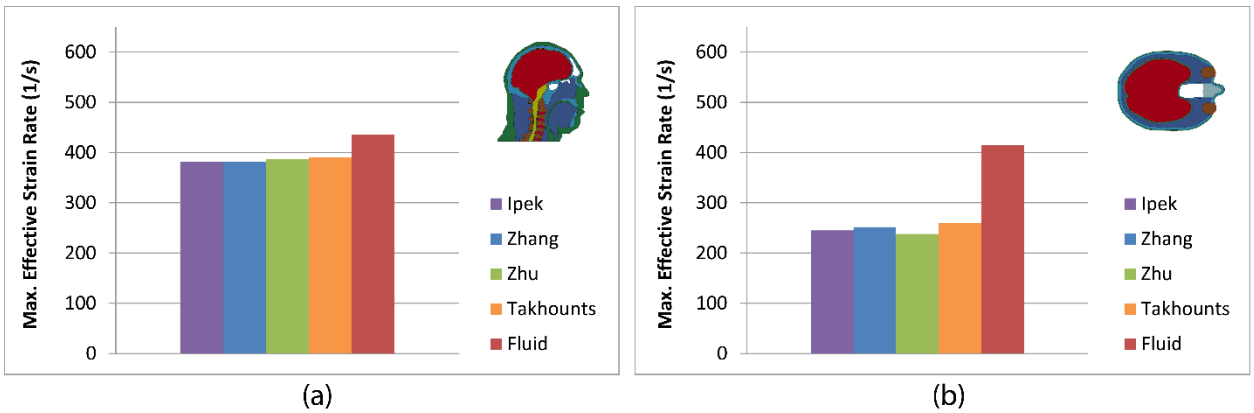

Figure 7.8: Comparison of peak effective strain rates for various viscoelastic parameters for (a) sagittal and (b) transverse models for 5 kg of C4 at 4 m standoff

7.4 Model Validation

Of critical importance in the development of a finite element model is validation against experimental data. The sagittal and transverse models described in the preceding sections were validated in their kinematic response and intracranial pressure response using available data.

7.4.1 Head Acceleration Validation

To validate the kinematics of the sagittal and transverse models, the peak head acceleration and HIC_{15} values of the models were compared to experimental data on Hybrid III anthropomorphic test device heads exposed to blast conducted by DRDC Valcartier [Lockhart et al. 2011]. The experimental tests used accelerometers mounted at the centre of gravity of Hybrid III heads to record the accelerations. The blast load cases in the experiments were 5 kg of C4 at a 1.5 m height of burst, tested at three standoff distances of 3, 3.5, and 4 m. The predicted kinematics of the sagittal and transverse were also compared to the predicted head kinematics from a simplified rigid multi-body numerical model of a human being called the Generator of Body Data (GEBOD), which has been previously used and validated for predicting kinematics resulting from blast [Haladuick et al. 2012, Cronin et al. 2008]. The head accelerations in the sagittal and transverse models were obtained from the resultant acceleration history of the skull. This was deemed to be a more appropriate measure of the head acceleration rather than the nodal acceleration at the location of the head centre of gravity, as nodal accelerations in finite element models generally lack robustness. The HIC_{15} values were calculated from the acceleration curves using the built in data processing functionality of LS-DYNA. The experimental acceleration data was filtered using a CFC 1000 filter with a cut-off frequency of 1650 Hz, in agreement with industry standards [Lockhart 2010].

The sagittal and transverse models predicted decreasing head accelerations with increasing blast standoff distance, as expected. Furthermore, the peak accelerations agreed well with the experimental values for all three standoffs (Figure 7.9). The experimental data is presented with error bars that represent the range of values seen in the experiments. The transverse model predicts slightly higher peak accelerations than the sagittal, but both fall within the scatter for the experimental data. The scatter of the experimental results is significant for the smaller standoff distances, in large part due to dynamic effects from the fireball at those close ranges.

The HIC_{15} values from the numerical models were similarly compared to the experimental values (Figure 7.10). Also include in this graph is the HIC_{15} tolerance value used in automotive standards. The numerical models predict slightly higher values of HIC_{15} for the 3.5 m and 4 m standoffs, and fall within the lower range of the experimental data for the 3 m standoff. With respect to the HIC_{15} tolerance level, the sagittal and transverse models do not exceed the threshold value for any of the standoffs, whereas both the GEBOD and the experimental data exceed the threshold for the 3 m standoff. It bears repeating that this threshold is merely a benchmark value, and not necessarily indicative of injury in the context of primary blast.

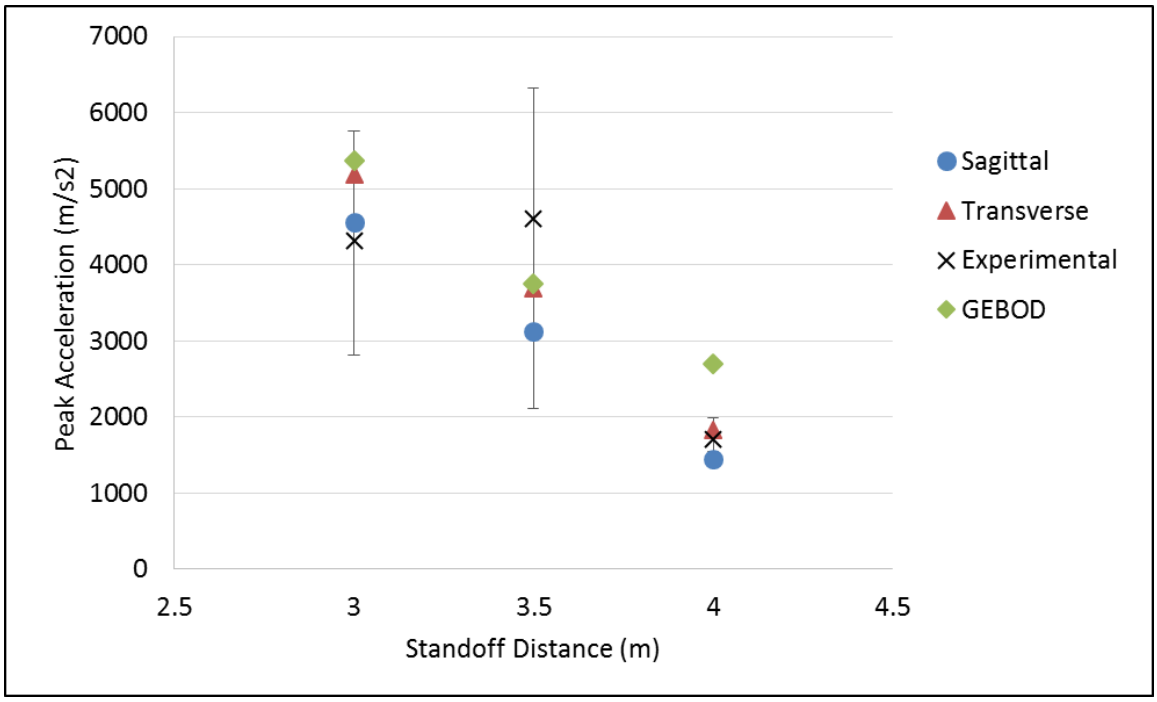

Figure 7.9: Results for peak head acceleration for 5 kg of C4 at various standoffs

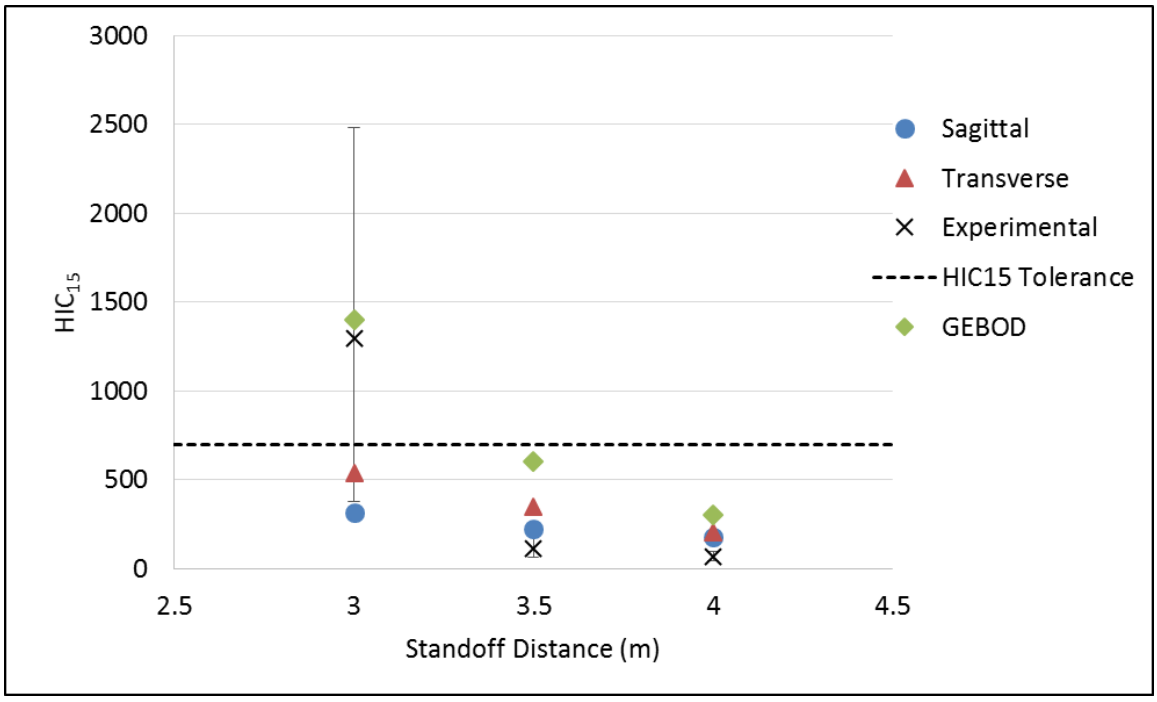

Figure 7.10: Results for HIC_{15} for 5 kg of C4 at various standoffs

An additional validation case of head kinematics in blunt impact loading was undertaken with the sagittal model to evaluate the model response under a different mode of loading, and this is included as Appendix C. The model was able to predict gross head kinematics due to blunt impact loading in good agreement with the experimental data, although the intracranial pressures were overpredicted by the models due to the focal nature of the impact. However, since blast loads are distributed relatively evenly across the head with smaller deformations of the tissues, this was judged to be acceptable.

7.4.2 Intracranial Pressure Validation

Since intracranial pressure is one of the key response metrics in primary blast head injury, validating the sagittal and transverse models for ICP is necessary for understanding and assessing the predictions of the models. Due to the difficulties inherent in experimental studies using blast, the available data is highly limited. One of the more relevant sources of data is an experimental study conducted by Bir that measured intracranial pressures on post mortem human subject (PMHS) heads in a shock tube loading environment [Bir 2011]. This study used optical pressure sensors to record intracranial pressures at four locations in the brain, namely at the frontal, temporal, parietal, and occipital lobes. The predicted ICPs of the sagittal and transverse models were compared with the results from this study at the corresponding locations (Figure 7.11).

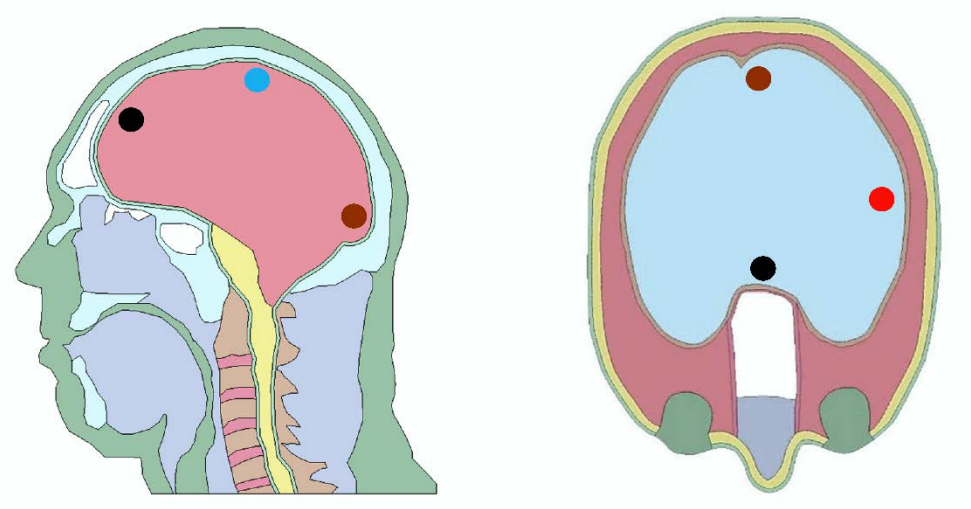

Figure 7.11: Corresponding locations in the sagittal model of the intracranial pressure transducers at the frontal (black), parietal (blue), occipital (brown), and temporal (red) locations

The experimental study exposed the PMHS heads to three different incident overpressures using the shock tube, specifically 71, 76, and 104 kPa with positive phase durations of 7.5, 7.4, and 7.0 ms respectively (Figure 7.12). These load cases are of lower pressure and greater duration than the nominal load cases selected as representative of mTBI in the current work, but are generally of a similar order of magnitude. The specific overpressure and duration from the Bir study were replicated in the ALE blast model and applied to the sagittal and transverse models using the method described in Section 7.2, so that the intracranial pressures could be compared directly.

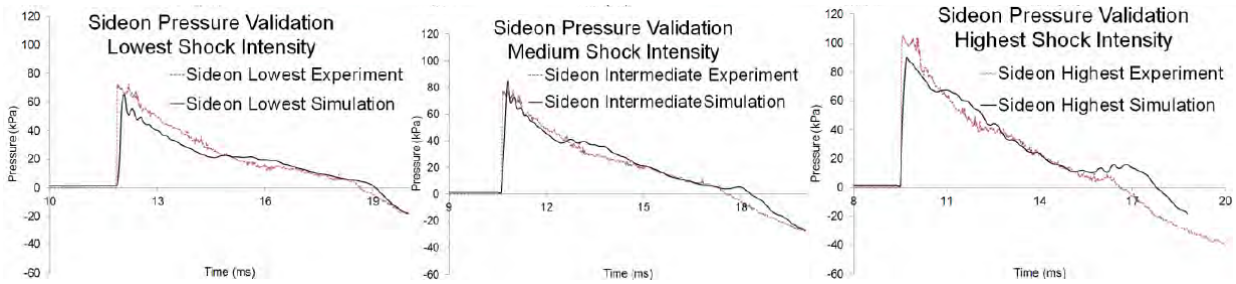

Figure 7.12: Pressure-time curves from the shock tube experiments conducted by Bir for three load intensities (adapted from Bir 2011)

Elemental pressure histories at the locations described in the study were extracted from the models, with the element in the models closest to the described location chosen. The variation in peak pressure with adjacent elements was nominally less than 5%, so the effect of element selection was minimal. The pressure histories of the models and experiments were compared for each location and for each load case (graphs included as Appendix D).

Due to the geometries of the sagittal and transverse models, parietal pressures could only be extracted from the sagittal model, and temporal pressures only from the transverse model. Frontal and occipital pressures were extracted from both models. Another important note about the geometries is that the transverse model geometry is at approximately eye level, whereas the experimental locations for the frontal and occipital measurements were offset from this plane (as can be seen in Figure 7.11).

In general, the models predicted pressure magnitudes and durations comparable to the experimental data (see Appendix D for the complete data set). Qualitatively, the frontal and temporal locations appear to have the best fit. The parietal location predicts comparable magnitudes, but overpredicts the durations. And the occipital location appears to have the

largest disagreement. In order to better understand the data and avoid purely qualitative analysis, the model response compared to the experiment was quantified.

A signal processing software called CORA was used to compare the experimental and numerical model curves in order to quantify the fit [Thunert, Gehre et al. 2009]. CORA is a mathematical tool that calculates a rating, analogous to a coefficient of determination, that describes the similarity of two transient responses. CORA uses two methods of comparison, a cross-correlation method and a response corridor method. The cross-correlation method uses the size, shape, and phase shift of the two curves to calculate fit, while the response corridor method uses user-defined corridors to quantify the fit. Since the repeatability in the experimental data was not sufficient to construct adequate response corridors, only the cross-correlation method was used for this analysis. While CORA is a valuable tool for quantification of data, it must be used with some degree of common sense, as the predicted correlation values of CORA can be tuned to an extent through modification of the analysis coefficients. In the current study, the default analysis coefficients for the CORA analysis were used, and were found to produce reasonable results. These analysis coefficients were held constant for the study, and are included in Appendix E.

The results of the CORA correlation are shown in Table 7.6, where the numbers are the determination coefficients for each load case and location. In some of the experimental cases, two experiments were done for a particular load case, so each experiment was correlated separately to the model curves.

Table 7.6: Cross-correlation comparison of sagittal and transverse models to experiments

Blast Insult	Front Sagittal	Front Transverse	Temporal	Parietal	Occipital Sagittal	Occipital Transverse	**Mean**
Low	0.855	0.717	0.536	0.677	0.448	0.434	**0.632**
	0.758	0.789	0.670	0.438	-	-	
Mid	0.890	0.919	0.710	0.718	0.530	0.453	**0.717**
	0.810	0.945	0.741	0.450	-	-	
High	0.824	0.892	0.742	0.769	0.266	0.270	**0.627**
Mean		**0.840**	**0.680**	**0.610**		**0.400**	**0.633**

A commonly used baseline for evaluating model fit in biomechanics is the ISO biofidelity classifications, which use a rating system based on the correlation coefficients. Under this system, the ratings are assigned designations according to the following definitions [Cesari et al. 2001].

Excellent:	0.860 – 1.000
Good:	0.650 – 0.859
Fair:	0.440 – 0.649
Marginal:	0.260 – 0.439
Unacceptable:	0.000 – 0.259

The mean correlation coefficient for the frontal location was 0.840, which demonstrated a good approaching excellent fit with the data. In terms of peak pressures at the frontal location, the models underpredicted the experimental values by 5%, 3%, and 25% for the 71, 76, and 104 kPa load cases respectively for the sagittal model, and by 13%, 26%, and 35% for the transverse model. At the temporal location, the peak pressure and durations were predicted accurately by the transverse model, which demonstrated a good fit with a coefficient of 0.680. The sagittal model predicted comparable peak pressures at the parietal location with a coefficient of 0.610, although the durations were overpredicted. The occipital location demonstrated the least fit with a correlation coefficient of 0.400, and the negative pressure and duration were

underpredicted by the models. The overall mean correlation coefficient for all load cases was 0.633 which, using the designations described above, is classified as a fair fit.

A major limitation of the experimental study was the lack of sample size, with most of the experiments reporting two curves, and many only reporting one. Although this significantly limits the ability to get a good estimate of the variability in the experiments, a crude estimate was calculated by comparing the experimental curves in all of the cases where two repeated experiments were presented using the cross correlation method. The overall average correlation coefficient for repeated experiments in the study was 0.595. This value is comparable to the overall correlation coefficient of the model fit, demonstrating that the variability between experiments is significant and similar to that of the models.

There are several sources of error in the experimental study that can account for the differences between the experimental and numerical data. Firstly, there is an inherent variability in biological testing, where tissue properties and geometries can vary significantly between specimens. Furthermore, the pressure transducers used in the models could affect the wave behaviour in the brain tissue since they have a different acoustic impedance than the surrounding tissues, although this effect is likely small due to the small size of the sensors used. Additionally, the PMHS specimen orientation is another variable that could significantly affect the pressures recorded by the transducers, whereas the sagittal and transverse models assume a horizontal Frankfurt plane.

Overall, in assessing the sagittal and transverse models in terms of their intracranial pressure predictions, the models are able to predict pressures with good agreement in the frontal, temporal, and parietal regions. At the occipital region, the models underpredict the negative

pressures. This could be due to the planar nature of the sagittal and transverse models, which cannot capture three dimensional effects. These three dimensional effects are further investigated in the following section.

7.5 Three Dimensional Ellipsoid Study

To investigate the effects of the three dimensionality of the head and how this influences the intracranial pressure predictions in the sagittal and transverse models, a study was undertaken using a simplified three dimensional ellipsoid representation of the head. The ellipsoid model approximated the general shape and size of the head, while remaining geometrically simple enough to develop with relative ease. By comparing the pressures in the three dimensional ellipsoid with sagittal and transverse planar models of the ellipsoid, the validity of the sagittal and transverse models in capturing the pressure response can be determined. It needs to be emphasized that the simplified three dimensional ellipsoid is not intended to be an accurate predictor of the biomechanical response of the human head. Rather, the purpose of the ellipsoid model was simply to provide a comparison with corresponding sagittal and transverse ellipse-shaped models to allow for a determination of the applicability of using such models to represent a three dimensional geometry.

7.5.1 3D Ellipsoid Methods

The three dimensional ellipsoid model consisted of three parts representing the brain, the cerebrospinal fluid, and the skull. It was decided that a quarter-symmetry model was sufficient to investigate three dimensional effects, instead of the half-symmetry model necessary to model the full human head. This was done to manage the computational demand which can become

prohibitive with three dimensional models with small element sizes. The dimensions of the quarter ellipsoid brain were defined to approximate the general size and proportions of the human brain, and were chosen to be 0.0605 x 0.0654 x 0.152 m (Figure 7.13). The cerebrospinal fluid layer was 2 mm thick with two elements across the thickness, and the skull layer was 5 mm with five elements across the thickness. These thicknesses were consistent with the average thicknesses of the sagittal and transverse geometries as derived from the Visible Human Project.

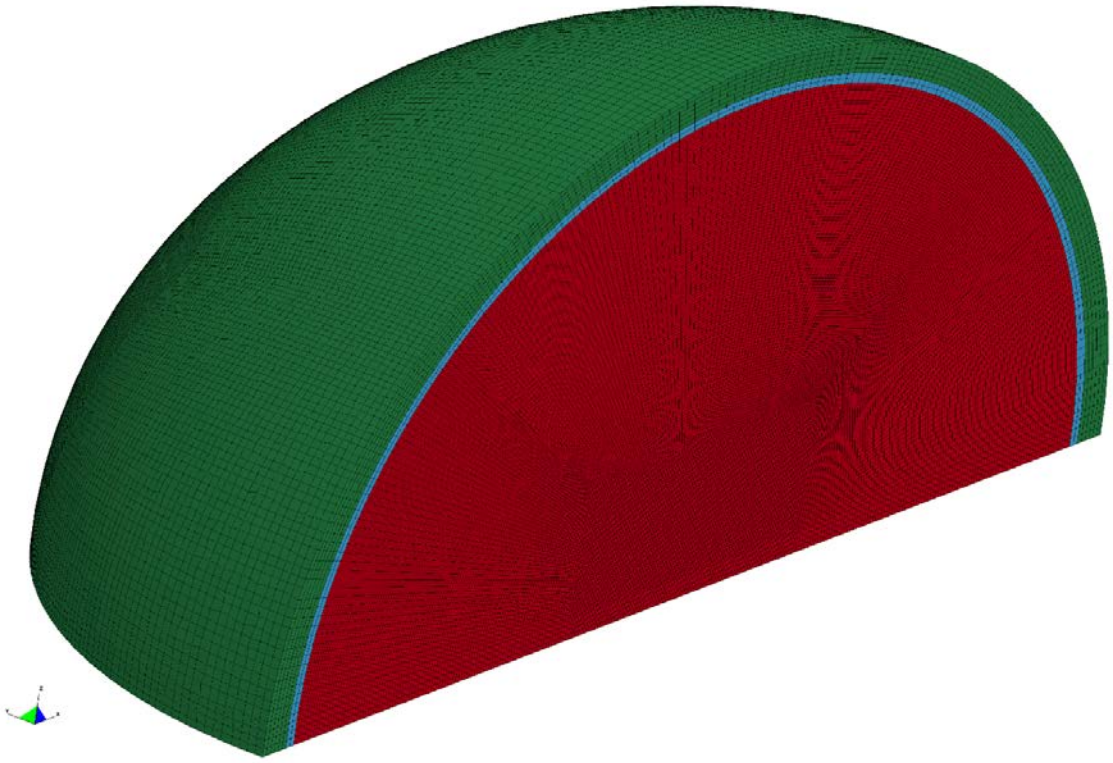

Figure 7.13: Simplified three dimensional ellipsoid mesh with the skull (green), CSF (blue), and brain (red) tissues

The same methodology was used for the ellipsoid model as the anatomical sagittal and transverse models. The ellipsoid model was meshed using solid hexahedral elements with an

average element size of 1 mm, which was consistent with the anatomical sagittal and transverse models, and was determined by a convergence study. The total number of elements in the quarter ellipsoid model was 1 977 664 solid elements. The material properties for the brain, the cerebrospinal fluid, and the skull were the same as described in Section 7.3.

The boundary conditions were also applied in the same manner, using an ALE air mesh. A rectangular air mesh of size 0.5 x 0.5 x 0.8 m was created, sized to prevent boundary reflection effects from interfering with the initial wave transmission through the quarter ellipsoid model (Figure 7.14). The element size of the air mesh was 1 mm in the vicinity of the quarter ellipsoid model, in order to facilitate accurate coupling between the ellipsoid model elements and the air elements (Figure 7.14). To reduce the number of elements in the air mesh, the mesh was graded so that the elements were larger away from the ellipsoid model. The number of elements in the air mesh was 5 507 600 solid elements. The quarter ellipsoid model was embedded into the ALE air mesh, and symmetry boundary conditions were imposed on the flat faces of the ellipsoid. The total three dimensional ellipsoid model including the head and the air meshes consisted of 7 485 264 solid elements, underscoring the large computational requirements of full three dimensional models.

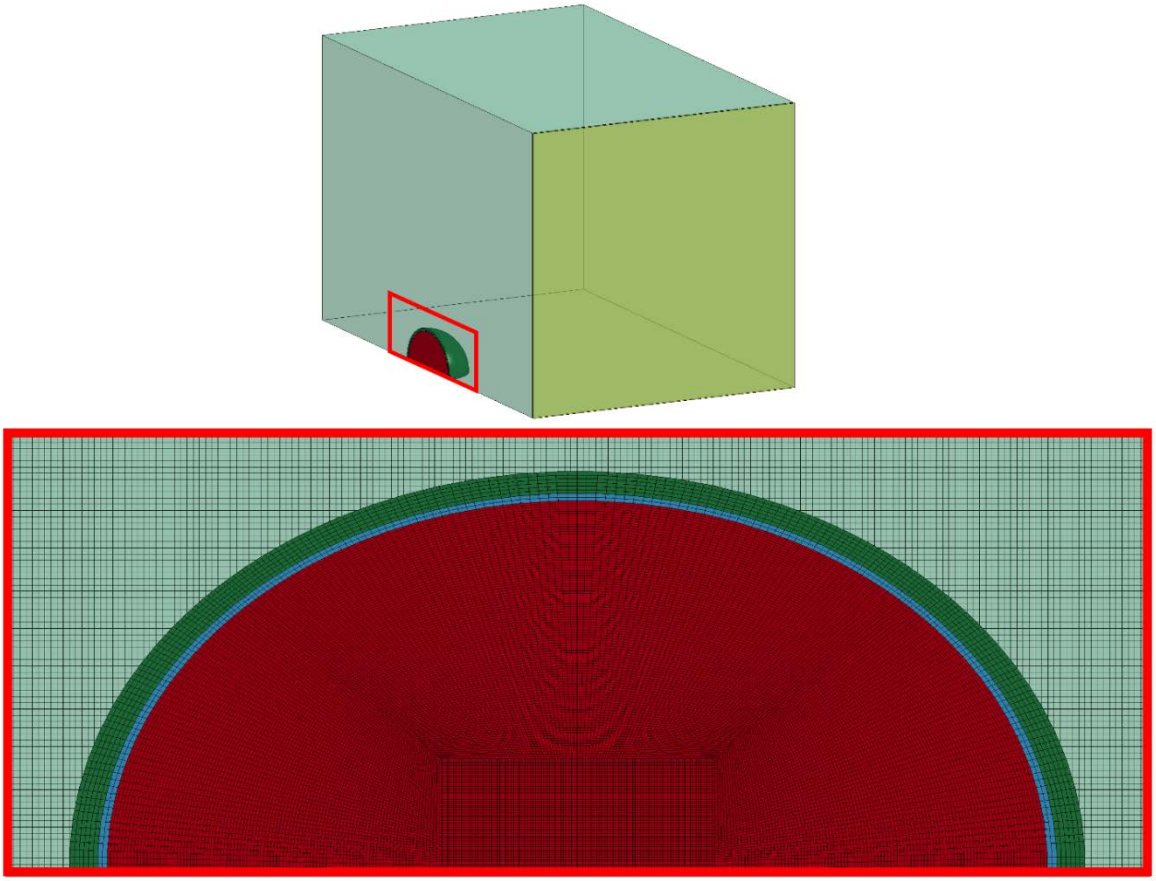

Figure 7.14: Three dimensional ellipsoid model in the three dimensional air mesh, with close-up of element size continuity between the head and air meshes

The blast load was applied to the ellipsoid model in the same way described in Section 7.2, where specific volume and temperature boundary conditions were applied to the air mesh, which created a pressure wave in the air that could propagate and impact with the ellipsoid mode.

Sagittal and transverse sectional models were created using the dimensions and geometry of the quarter ellipsoid model, analogous to the way that detailed anatomical sagittal and transverse models were created from the geometry of the human head (Figure 7.15). This allows a direct comparison of a three dimensional model with planar representations of it. The three models

(the three dimensional ellipsoid, the sagittal model of the ellipsoid, and the transverse model of the ellipsoid) were run with the same blast load case, corresponding to the 5 kg of C4 at 4 m standoff distance.

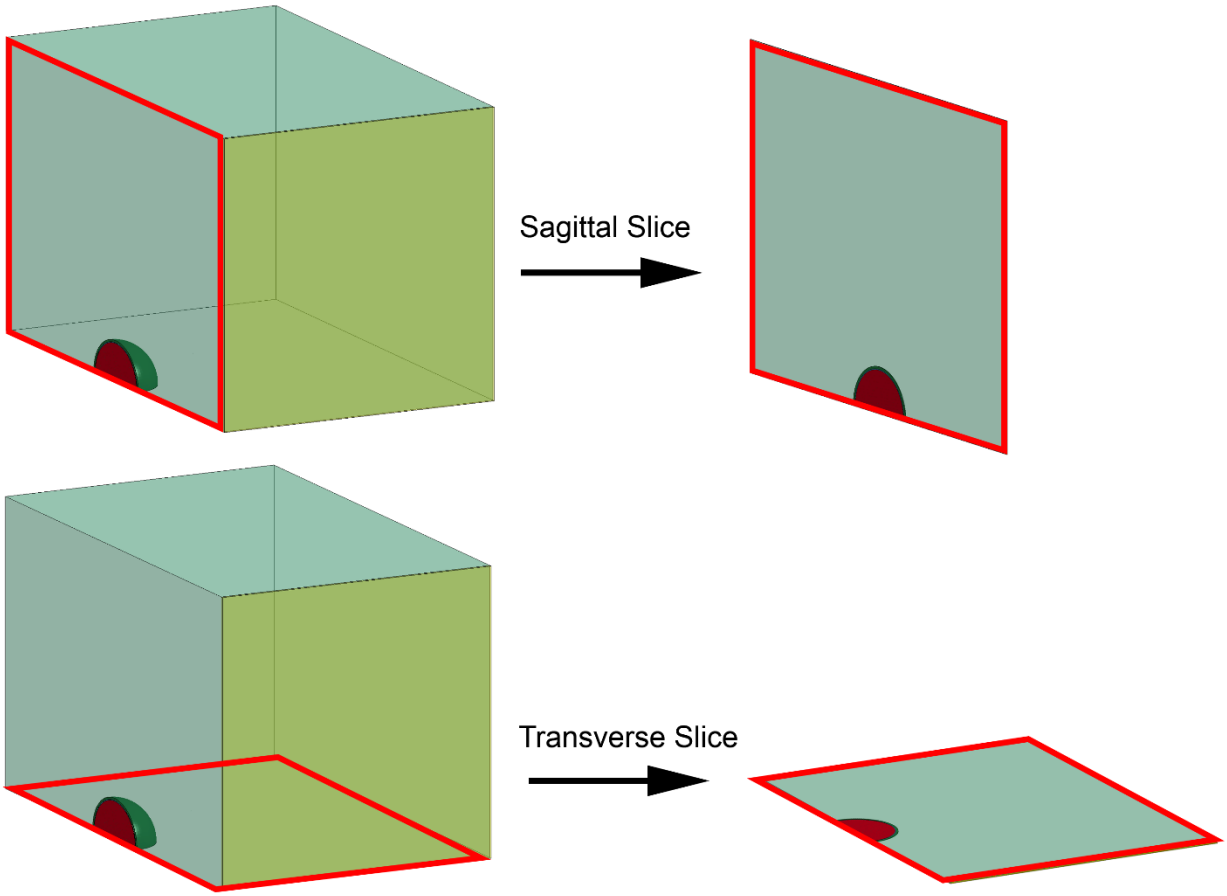

Figure 7.15: Visualization of the analogous sagittal and transverse versions of the three dimensional ellipsoid model

7.5.2 3D Ellipsoid Results

The peak intracranial pressures at four locations (frontal, temporal, parietal, and occipital) were compared between the three dimensional ellipsoid model and the sagittal and transverse

representations of the ellipsoid (Figure 7.16). The locations were chosen based on the four locations used in the intracranial pressure validation study in Section 7.4.2.

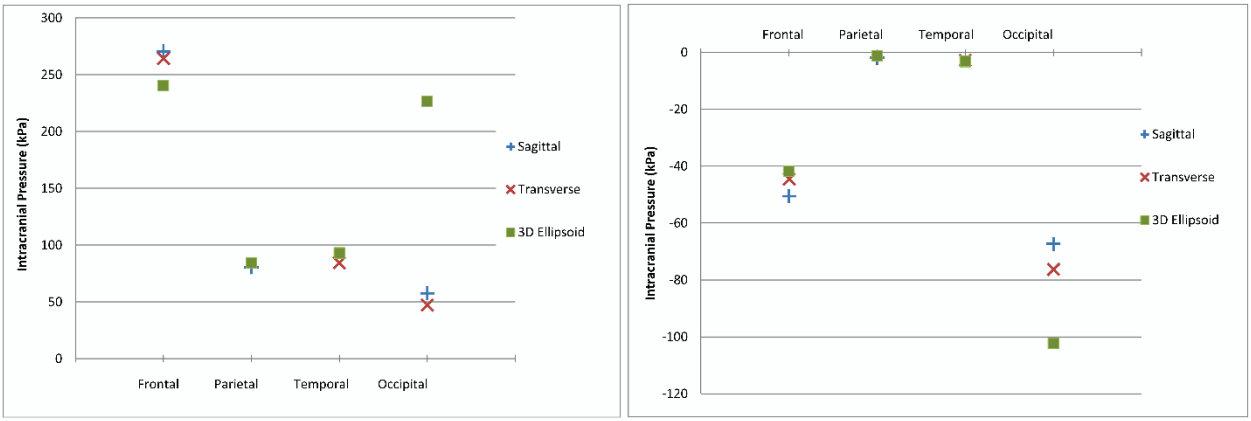

Figure 7.16: (a) Positive and (b) negative intracranial pressure results at various locations in the brain for the 3D ellipsoid model and its analogous sagittal and transverse models

The planar models of the ellipsoid reported pressures very close to one another, as expected since the geometries are very similar to each other, only differing slightly in proportion. At the frontal location, the planar models reported slightly greater peak positive and negative pressures (10 – 13%) than the ellipsoid model. Both the peak positive and negative pressure magnitudes at the temporal and parietal locations were in good agreement (<5%) with the ellipsoid model.

The occipital region demonstrated the most significant difference in terms of peak pressures. The three dimensional ellipsoid model predicted significantly greater positive and negative peak pressures than the planar models. This is likely due to wave superposition effects at the back of the simulated skull. The superposition effects are captured in the three dimensional model because the pressure wave travels and can undergo superposition along all the diagonal planes of the three dimensional curvature of the head. In the sagittal and transverse models, the

wave travels only along one plane, so the cumulative superposition of the wave will be smaller. This effect is important at the occipital location because that is where the superposition occurs due to the influence of the curvature of the head on the incident wave. In fact, the idealized geometry of the ellipsoid model may be overemphasizing this superposition effect by creating a stronger focusing effect than the anatomical geometry of the human head may warrant.

7.5.3 3D Ellipsoid Conclusions

The investigation of three dimensional effects using a simplified ellipsoid model has resulted is several important conclusions. Firstly, the sagittal and transverse models of the ellipsoid were able to predict intracranial pressures at the frontal, temporal, and parietal locations in good agreement with the three dimensional model. However, the pressures at the occipital location were underpredicted in the planar models, due to the lack of three-dimensional wave superposition in the planar models, although this superposition effect may be artificially enhanced by the idealized geometry of the ellipsoid model. Furthermore, the nature of the quarter model assumes symmetry about the transverse plane, which neglects the neck and torso that are present in an actual human head. The presence of the neck would serve to disrupt the pressure wave and reduce the effect of superposition at the occipital location. So although the sagittal and transverse do likely underpredict pressures at the occipital end since they cannot capture three dimensional effects, the difference is likely less than what the results of this simplified ellipsoid study suggest.

7.6 Model Overview

In summary, the sagittal and transverse blast head models used in this study utilize detailed anatomical geometries of the human head, coupled to an air mesh to simulate blast head interaction

in primary blast. Although three-dimensional wave effects cannot be simulated using the sagittal and transverse models, these models, being in perpendicular planes, allow us to capture the primary wave interactions of the blast wave and the head at two extremes of orientation, which is a reasonable compromise given the computational challenges inherent to a full three-dimensional models. The models were validated against experimental data for both head acceleration and intracranial pressure, and demonstrate good agreement. These models have several benefits over existing finite element blast models. Due to the small element size determined through mesh convergence analysis, the models are able to accurately resolve the magnitudes of pressure waves in the head in primary blast. Furthermore, due to the relatively fast completion time of the simulations, these models allow for comprehensive parametric studies to be conducted.

8. Results: Brain Tissue Response

The brain tissue response for both the sagittal and transverse models was investigated in terms of first principal strain, and positive and negative intracranial pressure. The results of the model simulations are presented in graphs that show the volume fraction of the brain material exposed to varying levels of pressure or strain. This allows the distribution of the response data in the brain tissue to be presented, as well as the maximum values.

The baseline load cases considered in this study are 5 kg of C4 at 3m, 3.5m, and 4m standoff distances. These were chosen because of the corresponding experimental tests conducted by DRDC Valcartier were done at these loads, and because the overpressures for these blast loads are generally consistent with those relevant to mTBI. The data for intracranial strain and pressure were extracted from simulations run at these load cases, to provide representative data for low to high blast overpressures.

The duration of the model simulation was 1.8 ms, starting from a time when the blast wave was 0.4 m away from the head. Relative to the simulated charge size and standoffs of 5 kg C4 at 3, 3.5, and 4 m, the start times of the simulations correspond to 1.83, 2.55, and 3.37 ms after detonation respectively. The duration of the simulation is limited by the size of the air mesh, since boundary reflections later in time introduce non-physical loadings. The 1.8 ms simulation duration was sufficient to model the initial transmission and reflection in the head and brain, which makes it sufficient for modeling primary blast injury.

8.1 Simulation Results

When the simulated blast overpressure wave impinges on the head models, pressure waves are generated in the tissues. These pressure waves are able to travel through the tissues of the head and into the brain, generating stresses and strains in the brain tissue. The waves transmit and reflect between the different tissue layers present in the models, and are observable in both the sagittal and transverse models (Figure 8.1). The blast wave makes contact with the head models at 0.43, 0.47, and 0.55 ms for the 3 m, 3.5 m, and 4 m standoffs respectively. The initial incident pressure wave passes through the head models (front to back) in less than 600 microseconds. In both the sagittal and transverse models, the blast wave experiences significant reflections off of the head models generating greater pressures in the air surrounding the heads (reflected pressure), as can be seen in Figure 8.1. The models report reflected pressures in front of the head to be 3 to 4 times the incident pressures. This is expected from blast wave theory where reflected pressures are typically between 2 and 8 times the static pressure as discussed in Section 2.3, and indicates that the fluid structure coupling is behaving correctly.

When the blast wave impacts the head models, significant pressures are generated in the anterior tissues of the head. Specifically, in the sagittal model, the tissues around the nose experience very large pressures during the initial impingement, due to proximity with the incoming blast wave. Additionally, the back of the neck and the lower three vertebral discs experience large pressures later in time (Figure 8.1, sagittal model at 1.25 ms), although this is likely due to the boundary condition imposed at the neck. In the transverse model, the eyes and nasal cavity tissue experience large pressures initially, again, because of their proximity with the incoming wave. Regardless, for the purposes of evaluating the response which is relevant for mTBI in primary blast, we are mostly interested in the brain tissue response.

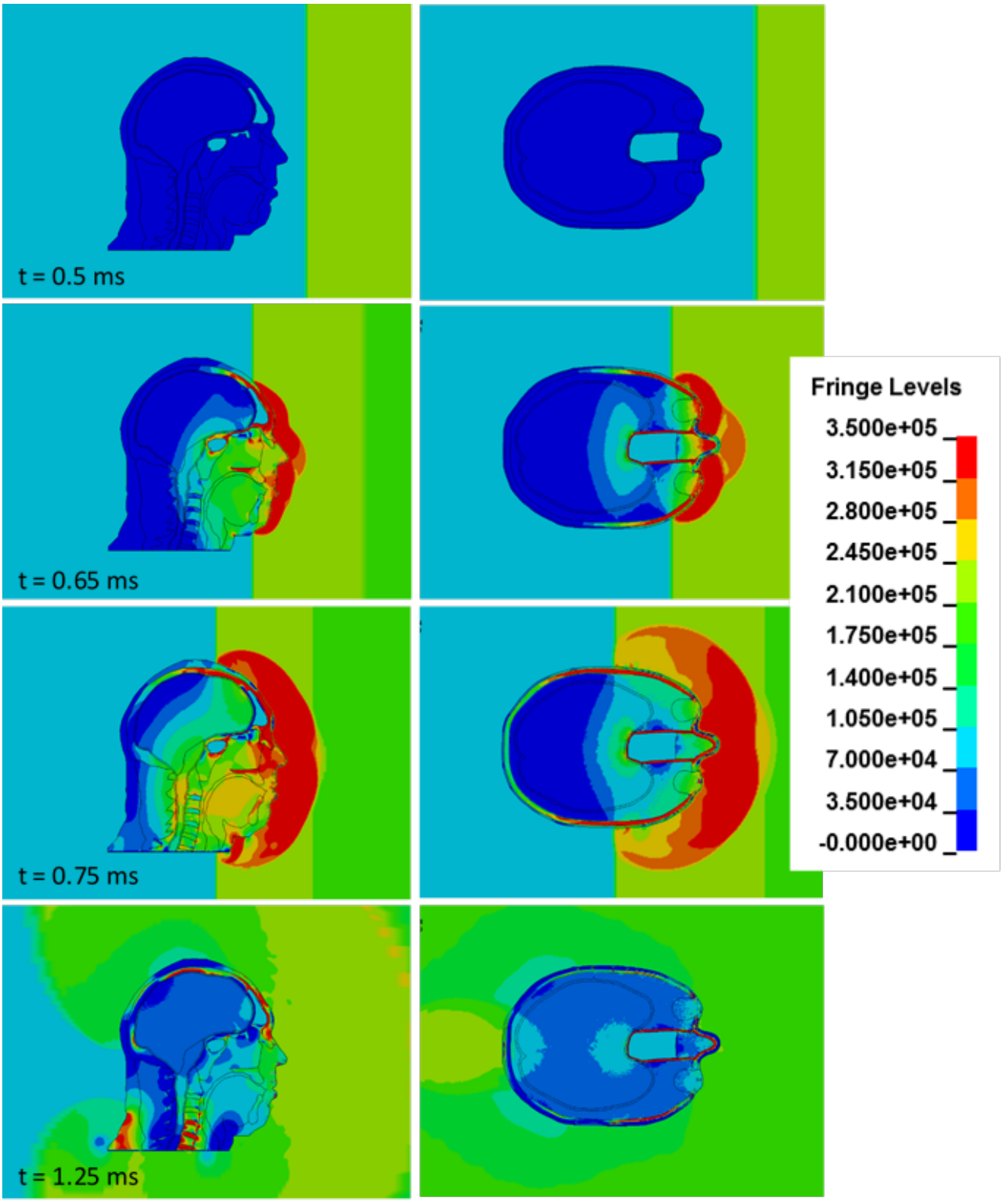

Figure 8.1: Simulation results for sagittal and transverse models at various times for 5 kg of C4 at 4 m standoff, with contours of pressure in Pa

The pressure waves in the models propagate through the brain tissue at a velocity of 1560 m/s, which is consistent with the acoustic wave speed for brain tissue reported in the literature [Tsaklis 2010]. In the sagittal model, the directly anterior portion of the brain is initially insulated from the wave by the superior sinus cavity. Consequently, the wave travels through the facial tissues and the skull and passes into the brain both above and below the sinus cavity (Figure 8.1, sagittal model at 0.65 ms). Similarly in the transverse model, the anterior portion of the brain is protected by the sinus cavity, although the energy of the wave is transferred through the bone enclosing the sinus to load the brain directly. The soft tissue pathway through the eyes serves as a secondary pathway for the wave to reach the brain (Figure 8.1, transverse model at 0.65 ms). The greatest positive intracranial pressures occurred in the anterior portions of the brain in both models, during the initial impact of the blast wave with the front of the head.

Skull flexure, which has been hypothesized as a potential mechanism of loading, is observed in the models. The sagittal model reports a maximum relative difference between the frontal and occipital bones of 0.075 – 0.231 mm depending on the standoff distance, and the transverse model from 0.346 – 0.826 mm. Although it is observed in the models as a structural response to the blast load, the implications of skull flexure on the brain tissue response remain unclear.

8.2 Brain Tissue Strain

The maximum first principal strains in the brain tissue are summarized in Table 8.1 for the sagittal and transverse models at the three load cases.

Table 8.1: Peak first principal strains in the brain tissue for the models for 5 kg of C4 at various standoffs

Blast Load Case	Sagittal	Transverse
4 m Standoff	0.053	0.035
3.5 m Standoff	0.054	0.038
3 m Standoff	0.087	0.062

However, these peak strains are only experienced by a small percentage of the brain volume, with the majority of the brain volume experiencing significantly smaller strains (Figure 8.2 and 8.3). Furthermore, the difference in strains between the different load cases are not very large, with about 80% of the brain volume experiencing similar values of strain for all three load cases. This suggests that principal strain is not a very sensitive response metric in primary blast.

The first principal strain response of the models follows the expected trend of increasing strain with decreasing standoff distance. The peak values of strain, as well as the distribution in the brain volume, are greater in the sagittal model than the transverse, although both models are in good agreement in terms of the shape of the curves (Figures 8.2 and 8.3).

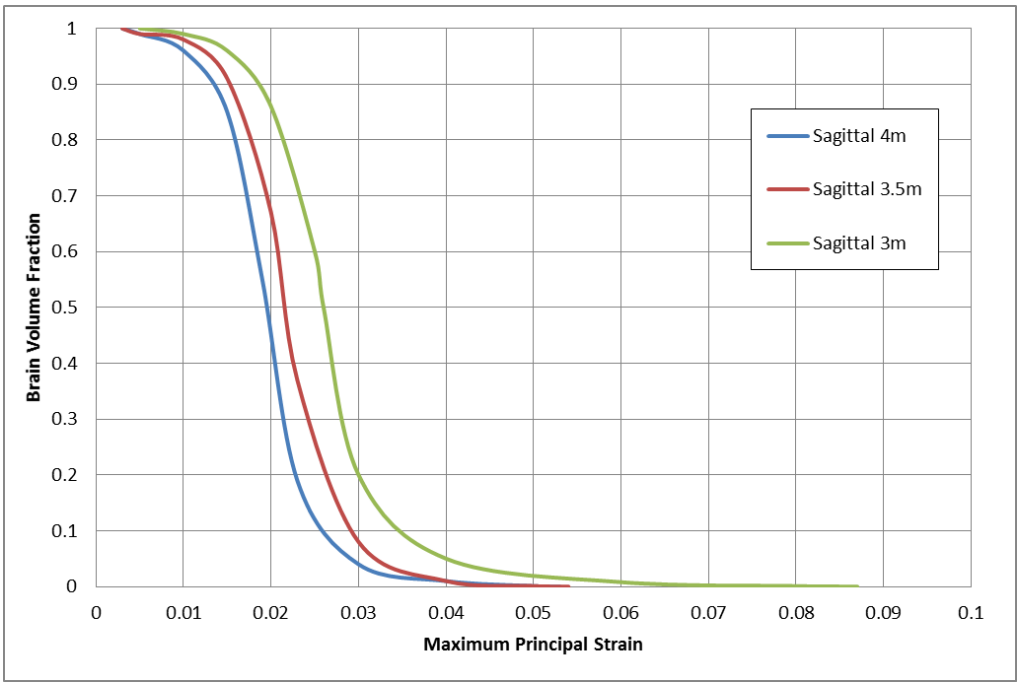

Figure 8.2: Intracranial strain response for the sagittal model for 5 kg of C4 at various standoffs

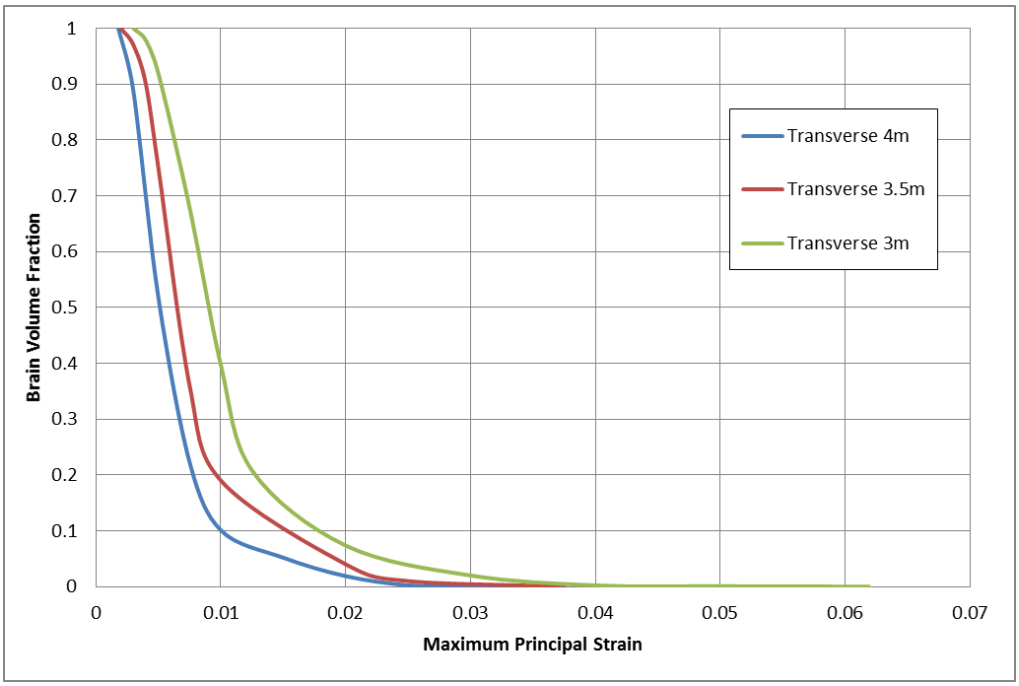

Figure 8.3: Intracranial strain response for the transverse model for 5 kg of C4 at various standoffs

Bayly et al. [Bayly et al. 2005] measured the deformation in the brain during mild frontal and occipital head impacts on volunteers, and reported first principal strains of 0.05 to 0.06. Although the actual impulse in these tests was not reported in the study, the peak accelerations in the experiment were generally three orders of magnitude lower in value, and the durations were three orders of magnitude greater in value than typical blast loads. Takhounts et al. [Takhounts et al. 2008] reported a maximum principal strain of 0.347 in their automotive finite element model with a peak linear acceleration of 135 g. In general, the principal strains predicted by the sagittal and transverse models in blast load conditions are relatively low compared to values predicted by automotive models [Deck 2008, Danelson et al. 2008, Feng et al. 2010].

The sagittal model reported peak shear strains approximately 10% greater in magnitude than the principal strains. In contrast, the transverse model reported shear strains approximately 20% lower in magnitude than the principal strains (Table 8.2). This may be due to the inherent asymmetry in the sagittal model geometry which creates more shear loadings in the tissues. However, the shear strains in both models generally exhibited the same trends with respect to standoff distance as the principal strains.

Table 8.2: Peak shear strains in the brain tissue for the models for 5 kg of C4 at various standoffs

Blast Load Case	Sagittal	Transverse
4 m Standoff	0.057	0.030
3.5 m Standoff	0.061	0.031
3 m Standoff	0.097	0.052

The maximum effective strain rate, which is an invariant measure of strain rate, reported in the brain tissue for each model was also extracted (Table 8.3). The strain rates that the models report

in primary blast, which range from 226 – 571 s^{-1}, are an order of magnitude greater than what is observed in typical automotive scenarios, where the rates generally range from 10 – 100 s^{-1} [Deck 2008, Danelson et al. 2008]. These high rates are expected in blast due to the high loads and short durations inherent to blast impacts.

Table 8.3: Peak effective strain rates in the brain tissue for the models for 5 kg of C4 at various standoffs

Blast Load Case	Sagittal	Transverse
4 m Standoff	378 s^{-1}	226 s^{-1}
3.5 m Standoff	422 s^{-1}	238 s^{-1}
3 m Standoff	571 s^{-1}	425 s^{-1}

Overall, the models report that the intracranial strains in primary blast are relatively small, reporting less than 10% peak principal strain even in the 3 m standoff load case. Thus, the assumptions made during the model development, where the strains were postulated to be small due to the lack of bulk motion in the time frames relevant to primary blast, are validated.

8.3 Intracranial Pressure

Both the sagittal and transverse models report significant intracranial pressures generated in the brain tissue upon blast wave impingement. The peak values of positive and negative intracranial pressure, as well as the 5% maximum volume fraction values are summarized in Table 8.4 for the three blast load cases. The 5% maximum volume fraction pressure is the maximum pressure experienced by at least 5% of the volume fraction of the brain tissue, and provides a representative value of pressure without allowing single elements to dominate the results. The selection of 5% for this measure did not alter any of the trends reported by the models. The positive and negative

intracranial pressures for the models are also plotted in terms of volume fraction of the brain tissue material that experienced varying levels of pressure over the course of the simulation (Figures 8.4 – 8.7).

Table 8.4: Peak and 5% maximum volume fraction of intracranial pressure (in kPa) for the models for 5 kg of C4 at various standoffs

Blast Load Case	**Sagittal**				**Transverse**			
	Positive ICP		Negative ICP		Positive ICP		Negative ICP	
	Peak	*5% Max*	*Peak*	*5% Max*	*Peak*	*5% Max*	*Peak*	*5% Max*
4 m Standoff	270.6	174.5	-71.9	-34.7	338.1	148.5	-91.1	-28.2
3.5 m Standoff	523.8	355.0	-148.4	-68.6	542.6	305.0	-199.4	-57.3
3 m Standoff	676.3	469.5	-232.5	-103.0	756.9	430.0	-311.3	-83.5

The positive intracranial pressures for both the sagittal and transverse models exhibited the expected trend of greater intracranial pressures with decreasing standoff distance. Both models demonstrated similar trends of pressure response with brain volume fraction for the three load cases (Figure 8.4, 8.5). Although the peak values in the transverse model were greater, the sagittal model reported a larger percentage of the brain volume being exposed to intermediate pressures. Furthermore, it is clear from Figures 8.4 and 8.5 that the highest values of pressure are only experienced by a small fraction of the brain material volume, with the majority of the brain experiencing significantly lower values.

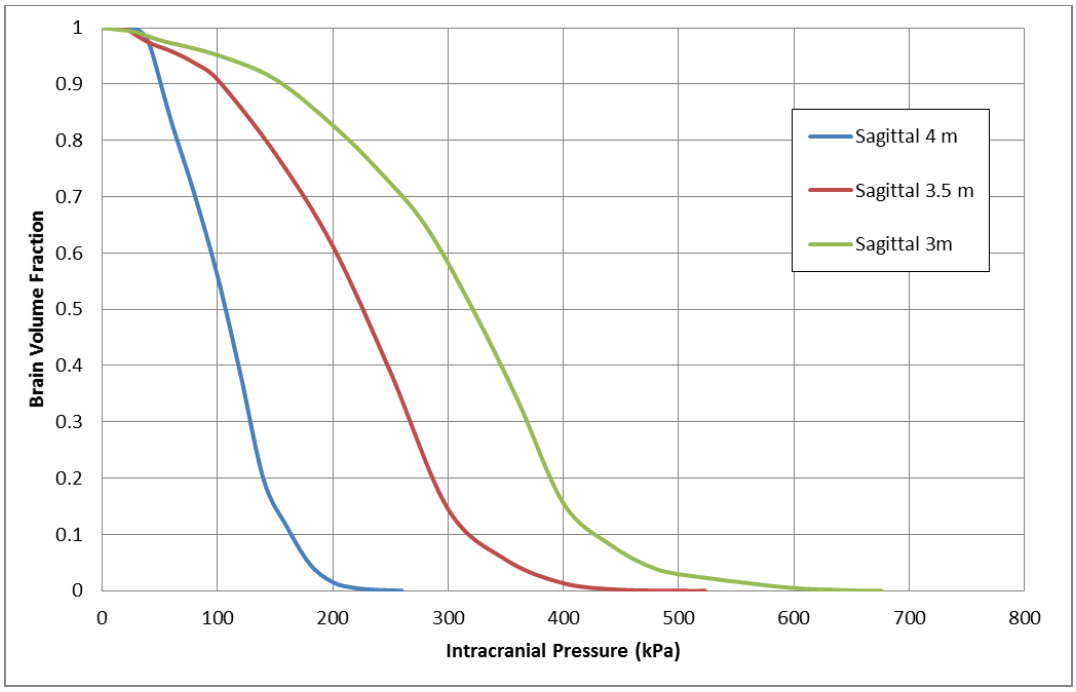

Figure 8.4: Positive intracranial pressure response for the sagittal model for 5 kg of C4 at various standoffs

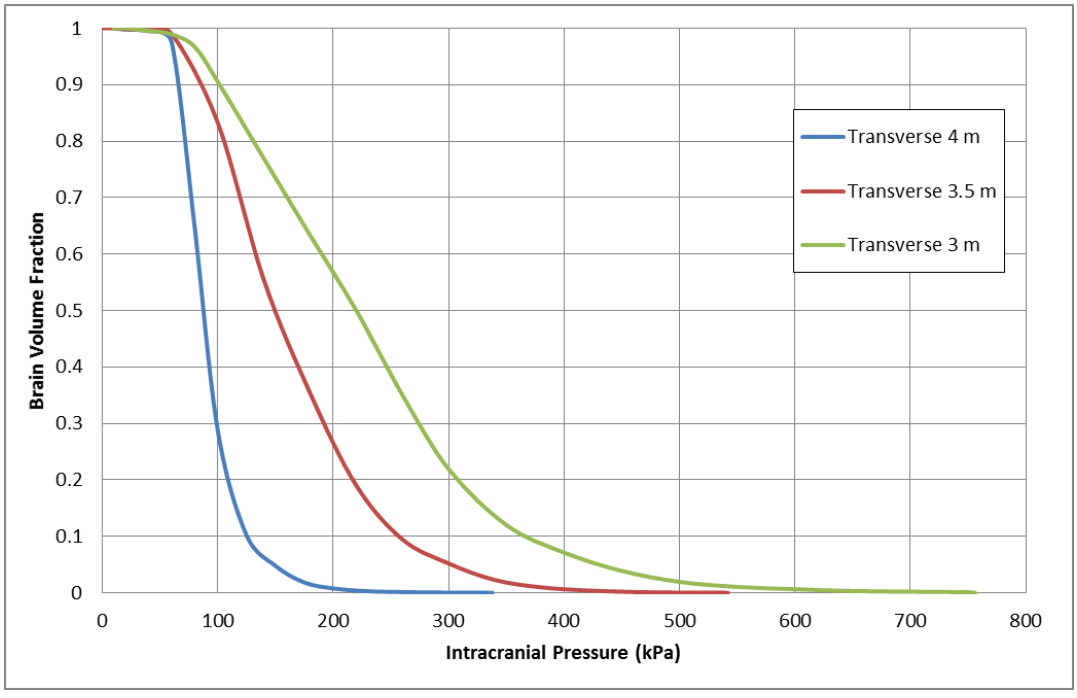

Figure 8.5: Positive intracranial pressure response for the transverse model for 5 kg of C4 at various standoffs

The negative pressure response of the models followed the same general trends as the positive pressure, and similarly exhibited relatively large peak values, but only for a small percentage of the brain volume (Figure 8.6, 8.7). Similar to the positive pressure response, the sagittal model reported smaller peak values of negative pressures, although more of the brain volume experienced intermediate pressures compared to the transverse model. Additionally, not all of the brain volume was exposed to negative pressures, more so in the transverse model where even the 3 m standoff load case resulted in only 60% of the brain volume experiencing negative pressures (Figure 8.7).

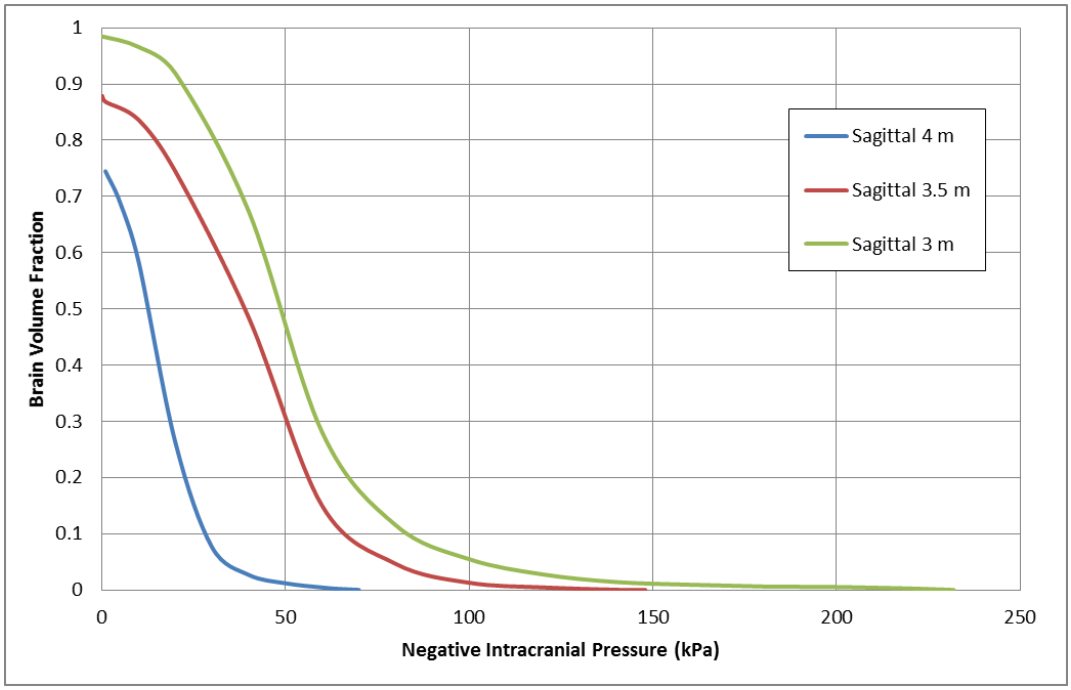

Figure 8.6: Negative intracranial pressure response for the sagittal model for 5 kg of C4 at various standoffs

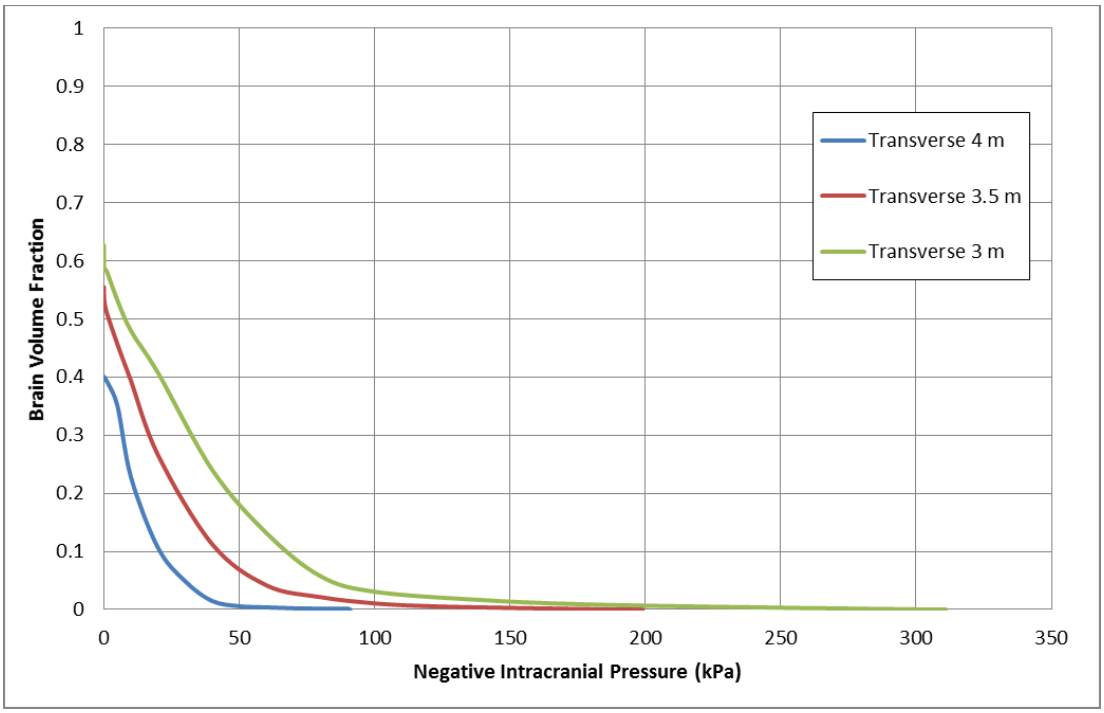

Figure 8.7: Negative intracranial pressure response for the transverse model for 5 kg of C4 at various standoffs

Another important observation that the models demonstrate is the tensile reflection of the initially compressive wave off the back of the head, which generates negative pressures in the brain tissue. Elemental pressure histories in the brain tissue for both the sagittal and transverse models demonstrate how the wave progresses through the brain and results in tensile pressures at the occipital regions (Figure 8.8, 8.9). This is due to the large impedance mismatch between the head and the surrounding air, and has been hypothesized as a potential mode of negative pressure loading. The models confirm the potential of this mode of loading to generate significant negative pressures in the posterior regions of the brain.

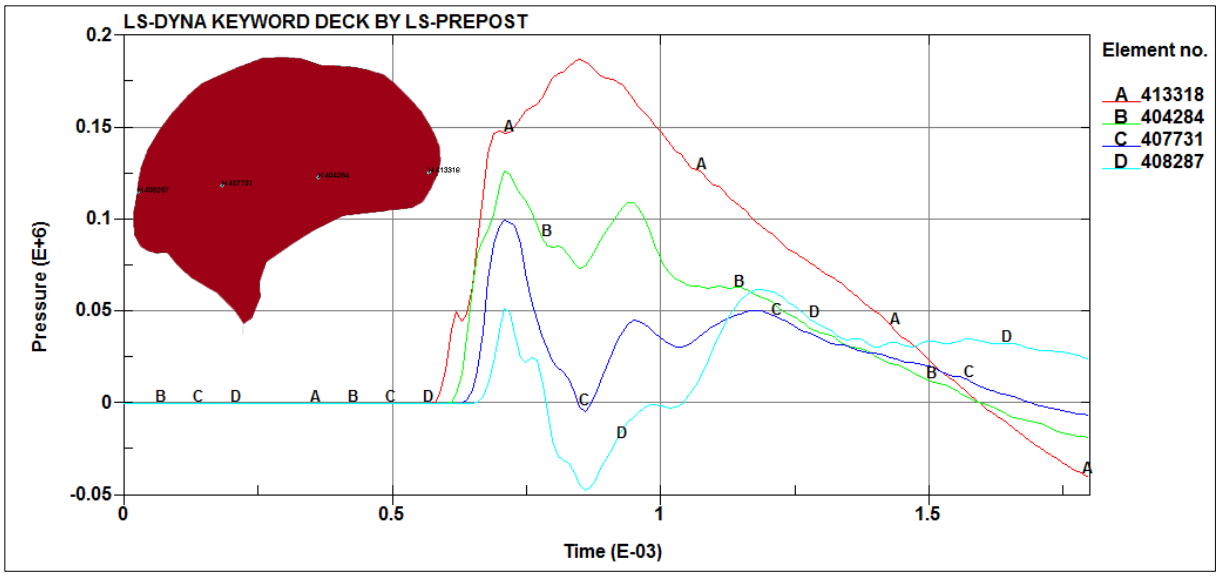

Figure 8.8: Pressure traces across brain tissue in sagittal model for 4 m load case (pressure in Pa vs. time in ms)

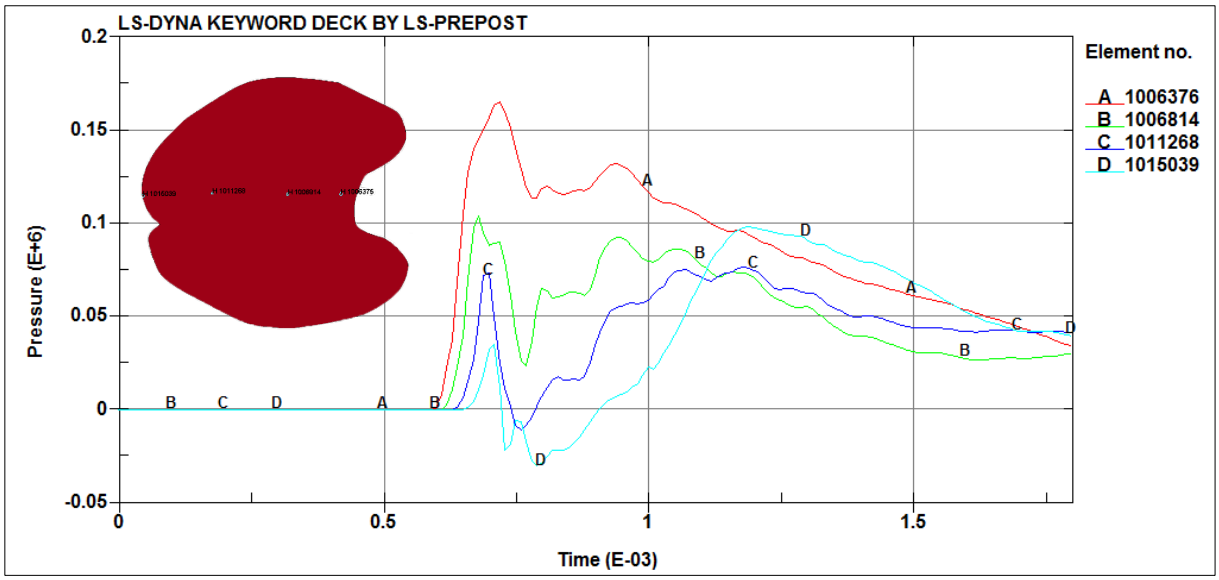

Figure 8.9: Pressure Traces across brain tissue in transverse model for 4 m load case (pressure in Pa vs. time in ms)

9. Results: Helmet Protection

In addition to allowing for the investigation of the nature of primary blast injury and the subsequent loading to the brain tissue, the sagittal and transverse models are well suited to evaluating protection strategies from blast. To that end, the models were used in a parametric study to evaluate the effects of various helmet configurations on the head response to blast. For the purposes of this study, the PASGT helmet was used due to the availability of its geometry and material properties, and widespread adoption internationally in combat helmet standards and applications.

9.1 Helmet Test Matrix

There were several factors that were considered in the parametric study. In terms of helmet material properties, two representative sets of constitutive properties were used for both the helmet Kevlar material and the foam lining. In addition, the models were also tested with no foam lining, to represent a helmet with a strap suspension system. Furthermore, a 6 mm thick polycarbonate visor was also investigated in both full-visor and half-visor configurations. Each parameter was tested for both the sagittal and transverse models, as well as for a high and low blast load (corresponding to 5 kg C4 at 3m and 4m). The different helmet configurations for the sagittal and transverse models are pictured in Figures 9.1 and 9.2 respectively. In contrast to the head model tissue interfaces, the nodes between the helmet and head were not merged. Instead, an automatic surface-to-surface contact algorithm was used to define the contact between the helmet foam lining and the head in the finite element models. This contact algorithm mimics the contact present when a person wears a helmet.

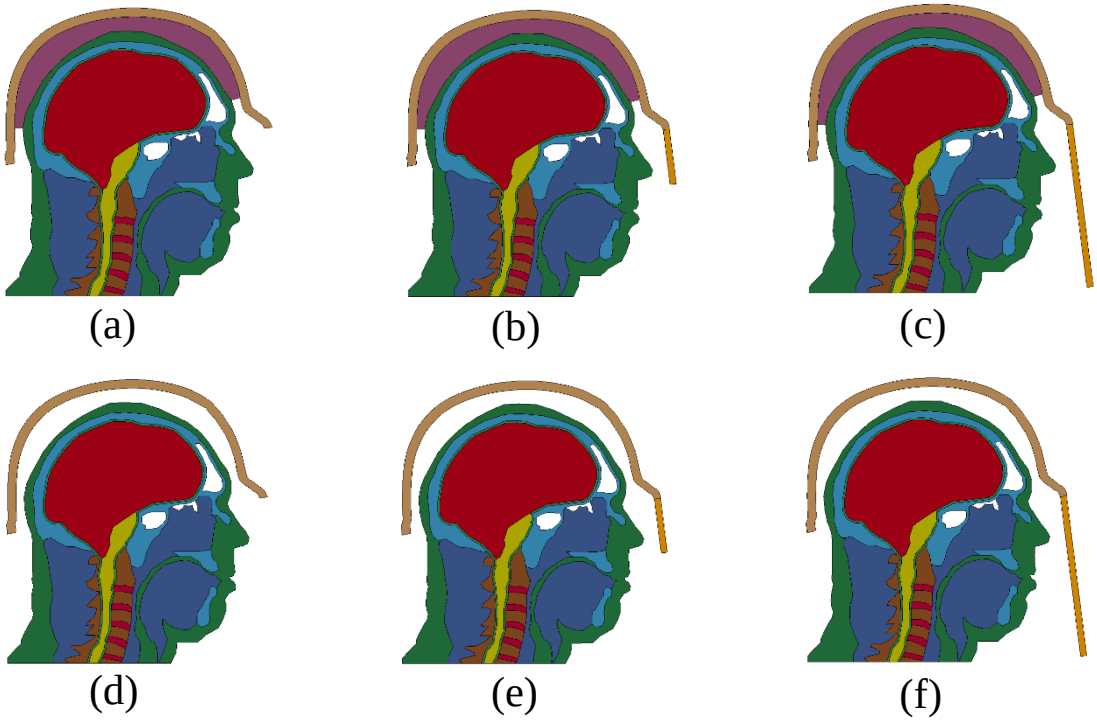

Figure 9.1: Sagittal model helmet configurations with (a) foam with no visor, (b) foam with half-visor, (c) foam with full-visor, (d) no foam with no visor, (e) no foam with half-visor, (f) no foam with full-visor

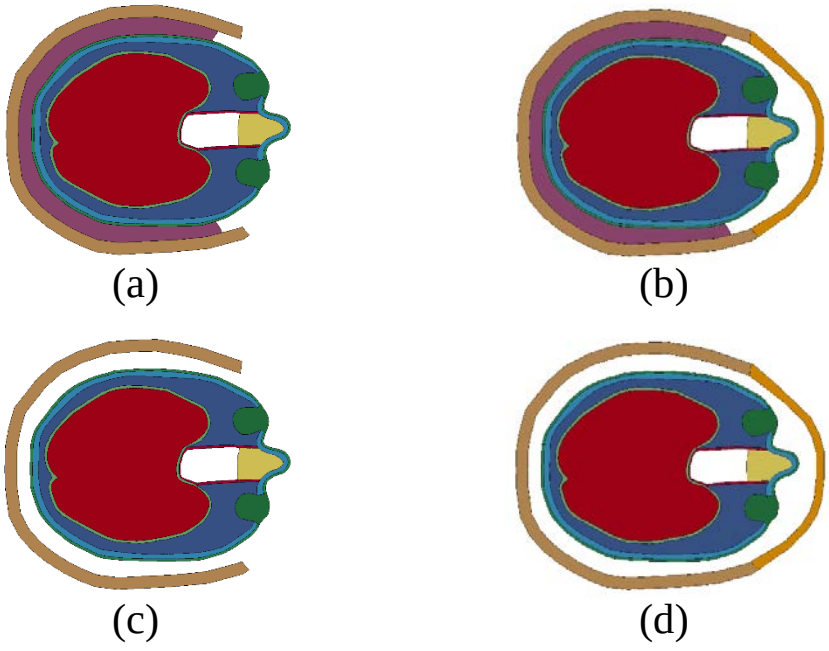

Figure 9.2: Transverse model helmet configurations with (a) foam with no visor, (b) foam with visor, (c) no foam with no visor, (d) no foam with visor

The two foam materials selected for the helmet lining in this parametric study were a high density polyethylene foam (HDPE85) and a low density polyethylene foam (LDPE45), the material properties for which are summarized in Figure 9.3. These two foam materials were chosen to allow for a comparison of response between a high and low density foam, since foam density is expected to be a significant variable in influencing helmet effectiveness.

Foam	Density (kg/m3)	Young's Modulus (kPa)
LDPE45	45	320
HDPE85	80	2720

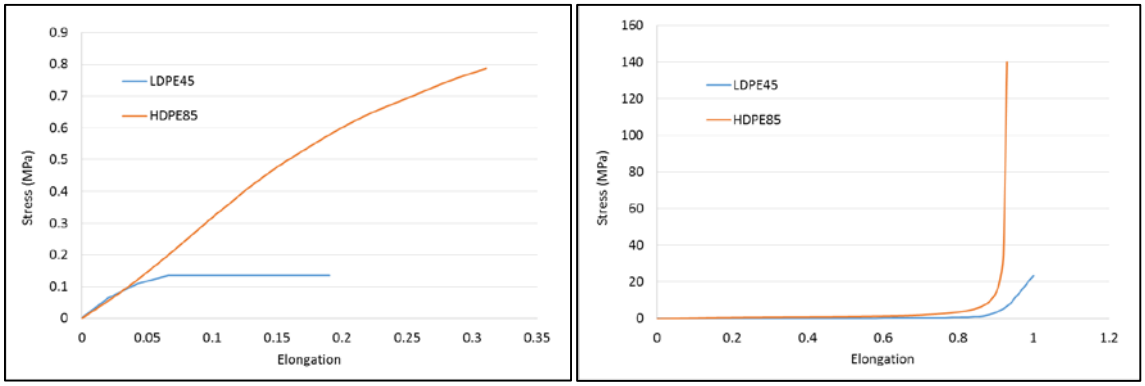

Figure 9.3: Foam material properties for high and low density polyethylene foams

The baseline helmet shell material was taken to be K29 Kevlar, which is the most commonly used Kevlar material in combat helmets with its material properties available. To determine the effects of the stiffness of the helmet shell, a low stiffness Kevlar material was used to provide a comparative response to the K29 material. The material properties for the Kevlar materials are summarized in Table 9.1, where the designations K1 and K2 are used to represent the high and low stiffness materials respectively. The Kevlar materials were modeled using an anisotropic constitutive model which includes anisotropy parameters that define the transformation matrix (*MAT_ORTHROTROPIC_ELASTIC in LS-DYNA).

Table 9.1: Kevlar material properties (adapted from Gower et al. 2008)

Material Property	High Stiffness (K1)	Low Stiffness (K2)
Density (kg/m^3)	1230	1230
E_1 (MPa)	18.5	1.85
E_2 (MPa)	18.5	1.85
E_3 (MPa)	6.0	0.6
PR_{21}	0.25	0.25
PR_{31}	0.33	0.33
PR_{32}	0.33	0.33
G_{12} (MPa)	0.77	0.077
G_{23} (MPa)	5.43	0.543
G_{31} (MPa)	5.43	0.543

A linear elastic material model with the properties of polycarbonate was used for the helmet visor material (Table 9.2).

Table 9.2: Polycarbonate visor properties

Material Property	Value
Density (kg/m^3)	1200
Elastic Modulus (MPa)	2300
Poisson's Ratio	0.37

The full parametric study, with the different foam and helmet materials, visor configurations, blast load cases, and differentiating between the sagittal and transverse models, resulted in 60 individual runs (Table 9.3).

Table 9.3: Helmet Test Matrix

	Model		Standoff		Visor			Foam			Kevlar	
	Sag.	**Trans.**	**4 m**	**3 m**	**None**	**Half**	**Full**	**None**	**LDPE**	**HDPE**	**K1**	**K2**
1	X		X		X			X			X	
2	X		X		X			X				X
3	X		X		X				X		X	
4	X		X		X				X			X
5	X		X		X					X	X	
6	X		X		X					X		X
7	X		X			X		X			X	
8	X		X			X		X				X
9	X		X			X			X		X	
10	X		X			X			X			X
11	X		X			X				X	X	
12	X		X			X				X		X
13	X		X				X	X			X	
14	X		X				X	X				X
15	X		X				X		X		X	
16	X		X				X		X			X
17	X		X				X			X	X	
18	X		X				X			X		X
19	X			X				X			X	
20	X			X				X				X
21	X			X					X		X	
22	X			X					X			X
23	X			X						X	X	
24	X			X						X		X
25	X			X				X			X	
26	X			X				X				X
27	X			X					X		X	
28	X			X					X			X
29	X			X						X	X	
30	X			X						X		X
31	X			X				X			X	
32	X			X				X				X
33	X			X					X		X	
34	X			X					X			X
35	X			X						X	X	
36	X			X						X		X
37		X	X		X			X			X	
38		X	X		X			X				X
39		X	X		X				X		X	
40		X	X		X				X			X
41		X	X		X					X	X	
42		X	X		X					X		X
43		X	X				X	X			X	
44		X	X				X	X				X
45		X	X				X		X		X	
46		X	X				X		X			X
47		X	X				X			X	X	
48		X	X				X			X		X
49		X		X	X			X			X	
50		X		X	X			X				X
51		X		X	X				X		X	
52		X		X	X				X			X
53		X		X	X					X	X	
54		X		X	X					X		X
55		X		X			X	X			X	
56		X		X			X	X				X
57		X		X			X		X		X	
58		X		X			X		X			X
59		X		X			X			X	X	
60		X		X			X			X		X

The model response was measured in terms of positive and negative intracranial pressure, as well as peak head acceleration. To prevent single elements from defining the model response, representative intracranial pressure magnitudes were measured using the 5% maximum volume fraction pressure, as described in Section 8.3. The peak head acceleration was measured using the resultant average acceleration of the whole skull.

9.2 Results of Parametric Study

The results of the parametric study are separated into three subsections. First, the overall trends in the data will be discussed with the raw data from the model simulations. Secondly, a quantitative analysis of the different parameter effects will be performed using the averaged results for each parameter configuration. Lastly, the pathways of loading of the brain tissue from the primary blast wave will be discussed in detail for each of the helmet geometry configurations.

9.2.1 Overall Trends

The results of the parametric study for the models are separated for the sagittal and transverse models for the two load cases. Table 9.4 and Figure 9.4 summarize the results for the sagittal model with the 4 m standoff distance load case.

Table 9.4: Parametric study results for sagittal model at 4 m standoff

Configuration			ICP (Pa)		Negative ICP (Pa)		Head Acceleration (1000 m/s²)	
Visor	*Foam*	*Kevlar*	*5% Max*	*% Reduction*	*5% Max*	*% Reduction*	*Peak*	*% Reduction*
Unprotected			174500		34700		1.44	
Full	HDPE	K1	85500	51.0	58000	-67.1	0.318	77.9
Full	HDPE	K2	86800	50.3	55300	-59.4	0.311	78.4
Full	LDPE	K1	80500	53.9	40200	-15.9	0.279	80.6
Full	LDPE	K2	83500	52.1	32800	5.5	0.276	80.8
Full	None	K1	62500	64.2	100	99.7	0.193	86.6
Full	None	K2	69800	60.0	2100	93.9	0.204	85.8
Half	HDPE	K1	108300	37.9	25000	28.0	0.652	54.7
Half	HDPE	K2	110800	36.5	26500	23.6	0.647	55.1
Half	LDPE	K1	109000	37.5	25000	28.0	0.641	55.5
Half	LDPE	K2	127500	26.9	12800	63.1	0.704	51.1
Half	None	K1	122300	29.9	100	99.7	0.681	52.7
Half	None	K2	131000	24.9	3300	90.5	0.742	48.5
None	HDPE	K1	134300	23.0	19500	43.8	1.006	30.1
None	HDPE	K2	135500	22.3	25000	28.0	1.006	30.1
None	LDPE	K1	133000	23.8	19800	42.9	0.996	30.8
None	LDPE	K2	137000	21.5	25800	25.6	1.026	28.8
None	None	K1	128800	26.2	100	99.7	0.969	32.7
None	None	K2	131000	24.9	5400	84.4	1.009	29.9

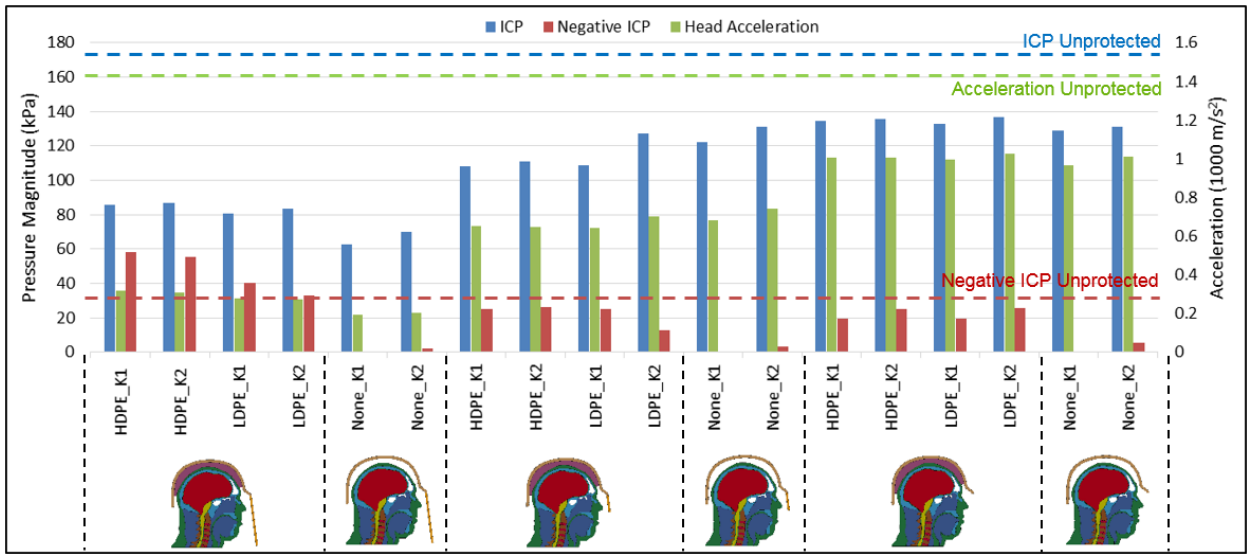

Figure 9.4: Parametric study results for sagittal model at 4 m standoff

Looking at results from the sagittal model at the 4 m load case, it is clear that the helmet configuration can have a significant effect on the intracranial pressures and head accelerations predicted by the model. In terms of acceleration, there is a clear difference between the full-visor, half-visor, and no-visor cases, which resulted in average accelerations of 263, 678, and 1002 m/s^2 respectively. This result makes sense intuitively, as the visor serves to protect the head from the pressure wave. It also makes sense kinematically, since the additional visor provides extra mass to the head-helmet system, which would result in reduced acceleration from the same inputted load. Within each visored case, there is not a significant difference in accelerations, except for the full-visor where the no foam configuration resulted in slightly lower accelerations. This is due to the decoupling of the helmet and head in combination with the large protection provided from the full-visor.

In terms of intracranial pressures, all of the helmeted cases resulted in reduced positive intracranial pressures compared to the unprotected case. The full-visor configuration average positive ICP was 78.1 kPa, significantly lower than the half-visor (118.2 kPa) and no-visor (133.3 kPa). This is due to the deflection of the pressure wave that results with the presence of the visor. Looking at Figure 9.4, qualitatively there is no obvious effect of the foam or Kevlar material on the positive ICP response.

In terms of negative ICP, the full-visor case actually resulted in increased values of negative pressure. There is also a clear difference between the foam materials in this case, where the low density foam results in lower pressures, because the face of the visor carries more of the energy of the blast wave and therefore the foam material at the forehead sees a greater compressive load. The no foam configuration resulted in greatly reduced negative pressures

for all cases, due to the decoupling from the head which prevents the wave reflection in the helmet from reaching the brain material.

The results for the sagittal model at the 3 m standoff distance are largely similar to the results for the 4 m standoff with regards to the trends (Table 9.5, Figure 9.5). However the negative pressure response was generally greater relative to the positive pressure.

Table 9.5: Parametric study results for sagittal model at 3 m standoff

Configuration			**ICP (Pa)**		**Negative ICP (Pa)**		**Head Acceleration (1000 m/s^2)**	
Visor	*Foam*	*Kevlar*	*5% Max*	*% Reduction*	*5% Max*	*% Reduction*	*Peak*	*% Reduction*
Unprotected			469500		103000		4.55	
Full	HDPE	K1	159500	66.0	165000	-60.2	0.636	86.0
Full	HDPE	K2	159000	66.1	150000	-45.6	0.595	86.9
Full	LDPE	K1	119500	74.5	108500	-5.3	0.536	88.2
Full	LDPE	K2	124000	73.6	84000	18.4	0.575	87.4
Full	None	K1	114000	75.7	8600	91.7	0.52	88.6
Full	None	K2	139300	70.3	19000	81.6	0.544	88.0
Half	HDPE	K1	257000	45.3	128500	-24.8	1.902	58.2
Half	HDPE	K2	263500	43.9	127000	-23.3	1.888	58.5
Half	LDPE	K1	259000	44.8	97000	5.8	1.819	60.0
Half	LDPE	K2	275500	41.3	52500	49.0	1.959	56.9
Half	None	K1	312000	33.5	18000	82.5	2.218	51.3
Half	None	K2	327400	30.3	22700	78.0	2.311	49.2
None	HDPE	K1	389000	17.1	108000	-4.9	3.127	31.3
None	HDPE	K2	392000	16.5	117000	-13.6	3.126	31.3
None	LDPE	K1	384000	18.2	92500	10.2	3.075	32.4
None	LDPE	K2	388000	17.4	75000	27.2	3.037	33.3
None	None	K1	372000	20.8	8800	91.5	3.006	33.9
None	None	K2	382000	18.6	23400	77.3	3.002	34.0

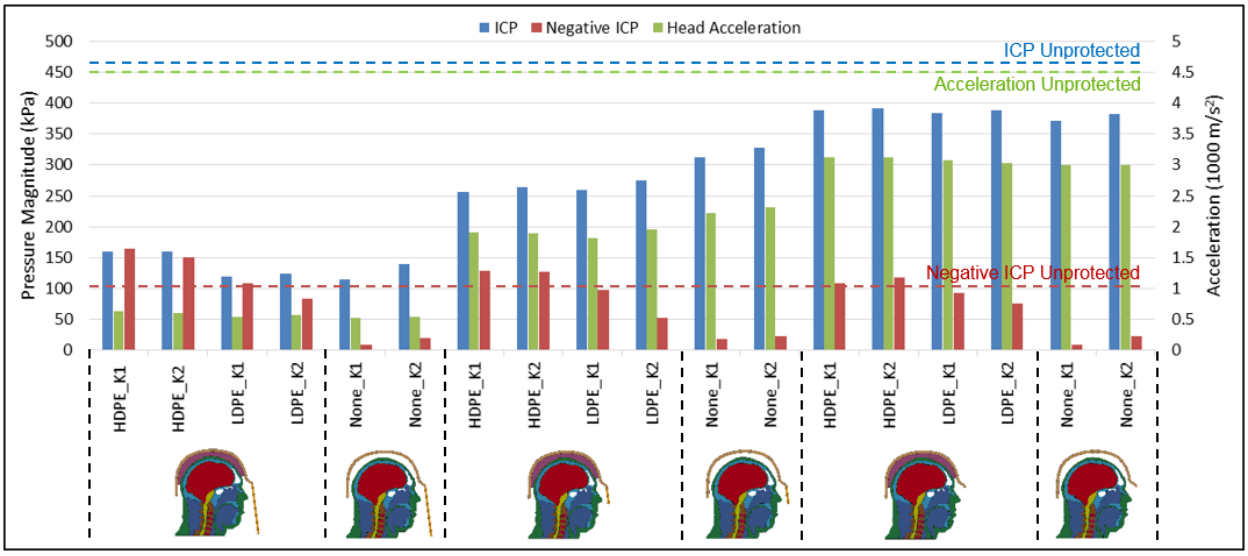

Figure 9.5: Parametric study results for sagittal model at 3 m standoff

The parametric study results for the transverse model at the 4 m standoff are shown in Table 9.6 and Figure 9.6.

Table 9.6: Parametric study results for transverse model at 4 m standoff

Configuration			ICP (Pa)		Negative ICP (Pa)		Head Acceleration (1000 m/s²)	
Visor	*Foam*	*Kevlar*	*5% Max*	*% Reduction*	*5% Max*	*% Reduction*	*Peak*	*% Reduction*
Unprotected			148500		28200		1.82	
Full	HDPE	K1	8200	94.5	136000	-382.3	1.28	29.7
Full	HDPE	K2	10200	93.1	151800	-438.3	1.335	26.6
Full	LDPE	K1	22000	85.2	90500	-220.9	1.038	43.0
Full	LDPE	K2	14600	90.2	99000	-251.1	0.967	46.9
Full	None	K1	3120	97.9	4050	85.6	0.763	58.1
Full	None	K2	2510	98.3	4250	84.9	0.811	55.4
None	HDPE	K1	178000	-19.9	24900	11.7	1.825	-0.3
None	HDPE	K2	171000	-15.2	33500	-18.8	1.918	-5.4
None	LDPE	K1	176000	-18.5	24000	14.9	1.831	-0.6
None	LDPE	K2	155000	-4.4	55500	-96.8	2.089	-14.8
None	None	K1	183500	-23.6	10500	62.8	1.674	8.0
None	None	K2	184500	-24.2	21800	22.7	1.82	0.0

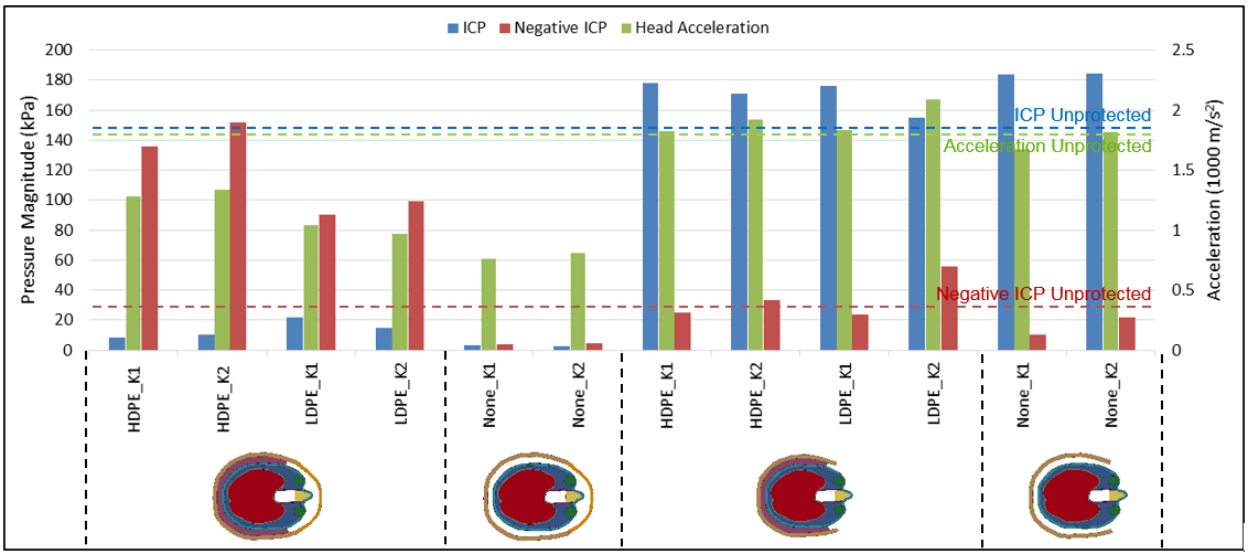

Figure 9.6: Parametric study results for transverse model at 4 m standoff

There are several important differences in the transverse model results due to the differences in geometry as compared to the sagittal model. The head acceleration follows the same trend, where the visored configuration results in reduced accelerations compared to the no-visor case. However, in contrast to the sagittal model results, the un-visored configuration resulted in slightly increased acceleration compared to the unprotected case for most configurations. This is likely due to the shape of the helmet on the head, which effectively captures more of the area of the incident blast wave and thus increases the amount of momentum transfer to the head.

With regards to positive intracranial pressure, there is a significant reduction in pressures for the visored cases, and a slight increase in pressures for the un-visored cases. This is in contrast to the sagittal model results, where all of the protected cases resulted in reduced positive pressures. The reason for this difference in the transverse model is due to the shape of the

helmet in the transverse plane. In the visored cases, the helmet provides a complete shield against the incident compressive blast wave, and so the positive pressures are expectedly mitigated. However, in the un-visored cases, the U-shape of the helmet serves to capture more of the wave and direct it into the head model, which increases the compressive pressures experienced by the brain tissue.

In terms of negative intracranial pressures, similar to the sagittal model results, the cases with the full-visor and foam lining resulted in significantly greater negative pressures than the unprotected case. Furthermore, the low density foam resulted in a clear reduction for the full-visored cases compared to the high density foam, a difference that is not clear in the non-visored cases. Also in agreement with the sagittal model results, the full-visor case with no foam resulted in reduced negative pressures, due to the decoupling of the head and the helmet.

The results of the transverse model at the 3 m standoff distance are shown in Table 9.7 and Figure 9.7. The increased blast load overpressure did not qualitatively change the patterns that are noticeable in the parametric study, so the results are similar in the overall trends of acceleration and intracranial pressure.

Table 9.7: Parametric study results for transverse model at 3 m standoff

Configuration			ICP (Pa)		Negative ICP (Pa)		Head Acceleration (1000 m/s^2)	
Visor	*Foam*	*Kevlar*	*5% Max*	*% Reduction*	*5% Max*	*% Reduction*	*Peak*	*% Reduction*
Unprotected			430000		83500		5.19	
Full	HDPE	K1	2500	99.4	321000	-284.4	3.156	39.2
Full	HDPE	K2	8500	98.0	389000	-365.9	2.837	45.3
Full	LDPE	K1	18500	95.7	192500	-130.5	2.018	61.1
Full	LDPE	K2	4000	99.1	181000	-116.8	1.696	67.3
Full	None	K1	8300	98.1	14900	82.2	1.194	77.0
Full	None	K2	27000	93.7	6700	92.0	0.853	83.6
None	HDPE	K1	508000	-18.1	76200	8.7	5.201	-0.2
None	HDPE	K2	508000	-18.1	124000	-48.5	5.335	-2.8
None	LDPE	K1	505000	-17.4	75500	9.6	5.222	-0.6
None	LDPE	K2	460000	-7.0	159500	-91.0	5.737	-10.5
None	None	K1	508000	-18.1	19000	77.2	4.671	10.0
None	None	K2	443000	-3.0	72000	13.8	4.998	3.7

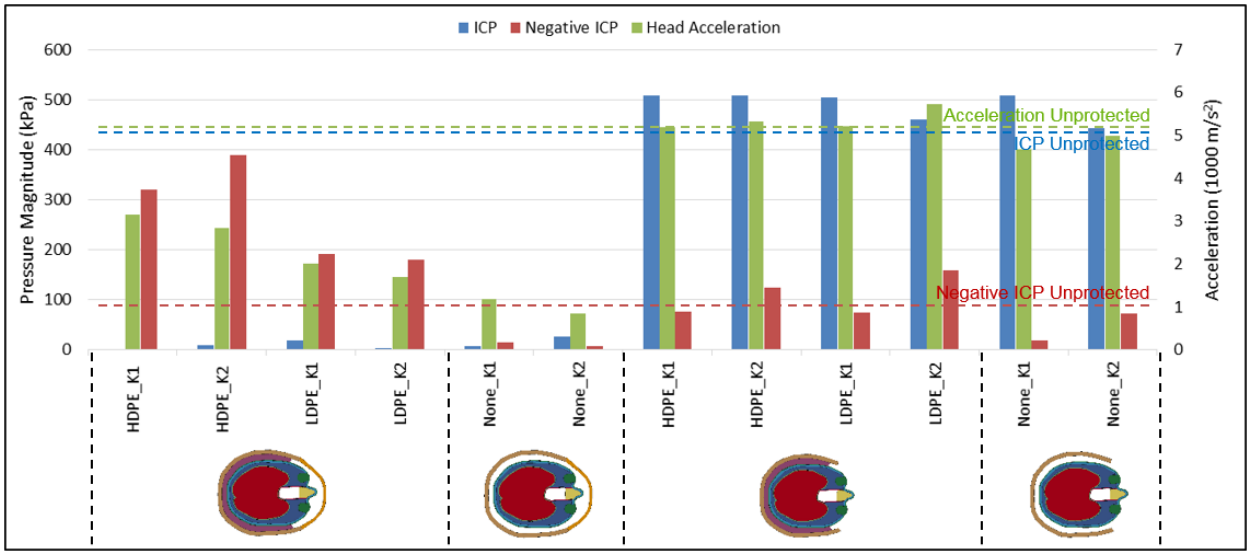

Figure 9.7: Parametric study results for transverse model at 3 m standoff

9.2.2 Parameter Effects

To better interpret and quantify the effects of the different parameters investigated in the parametric study, the averages of intracranial pressure and acceleration were calculated for each variable for both models at the two load cases (Table 9.8). This allows for a quantitative comparison of the effects of each variable on the pressure and acceleration response of the models. The 5% maximum volume fraction values of intracranial pressure were used in this analysis to provide better estimates of pressure response.

Table 9.8: Average model values for 5% maximum volume fraction ICP and head acceleration, for the parameters in the helmet parametric study at 4 m and 3 m standoffs

	Configuration		Intracranial Pressure (kPa)	Neg. Intracranial Pressure (kPa)	Peak Head Acceleration (1000 m/s^2)
Sagittal at 4 m standoff	Visor	Full	78.1	31.4	0.263
		Half	118.2	15.5	0.678
		None	133.3	15.9	1.002
	Foam	HDPE	110.2	34.9	0.657
		LDPE	111.8	26.1	0.654
		None	107.6	1.9	0.633
	Kevlar	K1	107.1	20.9	0.637
		K2	112.5	21.0	0.658
Sagittal at 3 m standoff	Visor	Full	135.9	89.2	0.568
		Half	282.4	74.3	2.016
		None	384.5	70.8	3.062
	Foam	HDPE	270.0	132.6	1.879
		LDPE	258.3	84.9	1.834
		None	274.5	16.8	1.934
	Kevlar	K1	262.9	81.7	1.871
		K2	272.3	74.5	1.893
Transverse at 4 m standoff	Visor	Full	10.1	80.9	1.032
		None	174.7	28.4	1.860
	Foam	HDPE	91.9	86.6	1.590
		LDPE	91.9	67.3	1.481
		None	93.4	10.2	1.267
	Kevlar	K1	95.1	48.3	1.402
		K2	89.6	61.0	1.490
Transverse at 3 m standoff	Visor	Full	11.5	184.2	1.959
		None	488.7	87.7	5.194
	Foam	HDPE	256.8	227.6	4.132
		LDPE	246.9	152.1	3.668
		None	246.6	28.2	2.929
	Kevlar	K1	258.4	116.5	3.577
		K2	241.8	155.4	3.576

The average parameter effects were plotted to provide a visual comparison of how the helmet configuration can affect the brain response. The visor configuration clearly has a large effect on both ICP predictions and head acceleration (Figure 9.8). There is clear reduction in positive intracranial pressure as the visor size increases, a trend that is evident in both the sagittal and transverse models. In contrast, the negative intracranial pressure demonstrates the opposite trend, where the full-visor resulted in the greatest negative pressures for both models. In terms of head acceleration, the peak values were significantly reduced with the presence of a visor in both models.

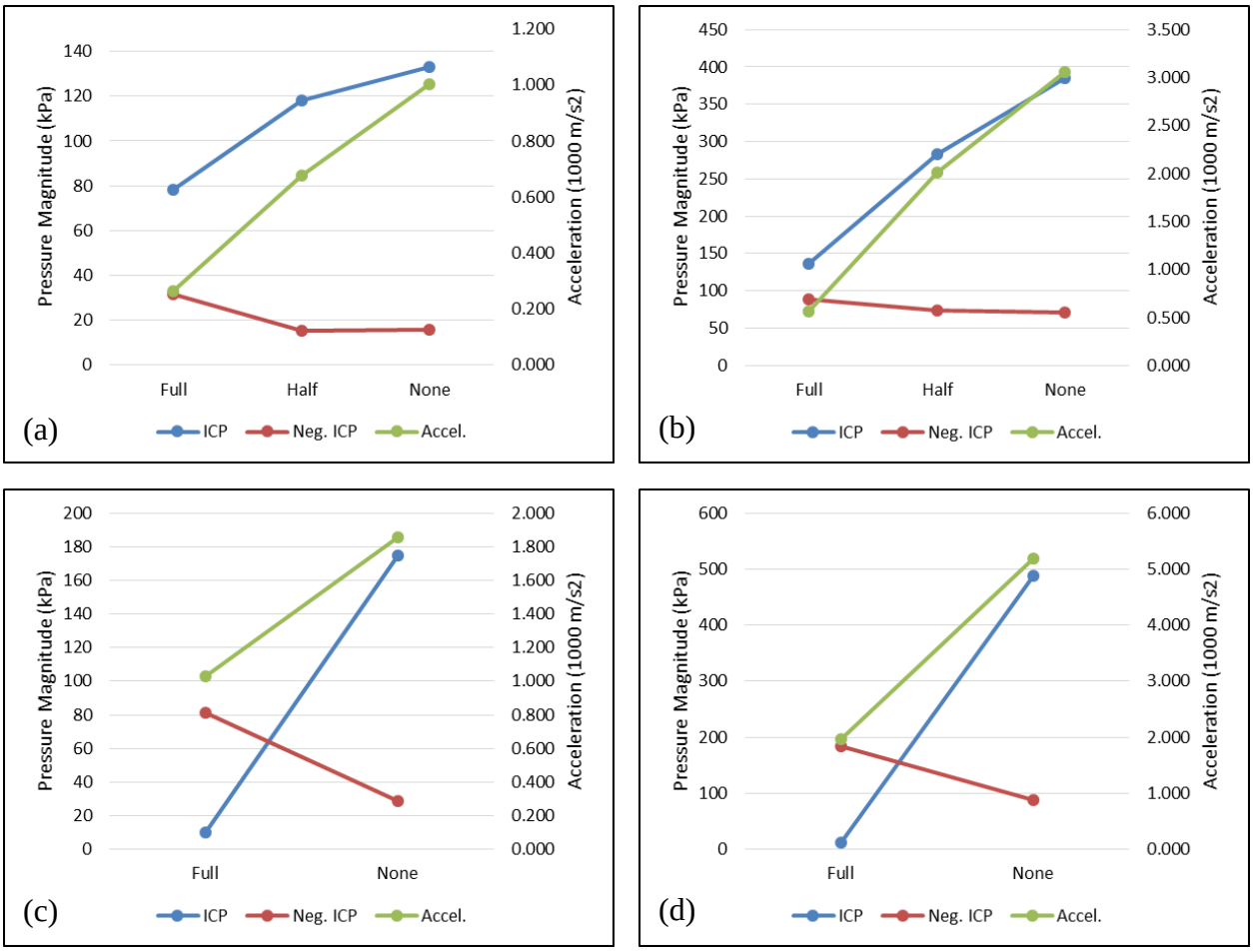

Figure 9.8: Visor configuration averages for (a) sagittal model at 4 m, (b) sagittal model at 3 m, (c) transverse model at 4 m, and (d) transverse model at 3 m

The foam material results also demonstrate some important trends (Figure 9.9). The positive intracranial pressure did not demonstrate any clear dependence on foam material in either model, however one important change can be observed in the sagittal model between the 4 m and 3 m standoff load cases (Figure 9.9a, b). In the 4 m case, the no foam case resulted in slightly lower ICPs than the foam cases, whereas in the 3 m case, the no foam case resulted in higher ICPs than the foam cases. This may be due to the higher load case, which has a greater incident overpressure, resulting in increased reflected pressures in the gap between the head and the helmet which create greater pressures in the brain. Nevertheless, this effect on the positive intracranial pressure was small compared to the effects of the foam material on negative pressures.

The negative pressures were greatest in the high density foam case for both models, followed by the low density, with the no foam case resulting in the lowest negative pressures. This difference is because the greatest positive pressures are generally at the anterior sections of the brain, which are more exposed to the incident wave directly, whereas the greatest negative pressures are at the occipital region of the brain, where the foam material has more of an influence on the wave behaviour. The no foam case results in the lowest negative pressures because the portion of the wave that transmits to the helmet shell is decoupled from the head, so its contribution to the loading on the brain tissue is eliminated. Moreover, the low density foam reduces negative pressures compared to the high density foam because of the increased impedance mismatch between the helmet material and the foam for the low density foam, which blocks a larger percentage of the wave from being transmitted into the foam material in comparison to the high density foam.

The head acceleration did not depend significantly on foam material in the sagittal model; although the same trend was observed where the higher overpressure 3 m load case resulted in the no foam case reported greater accelerations compared to the 4 m case. In the transverse model, the no foam case resulted in the lowest accelerations, followed by the low density foam and then the high density.

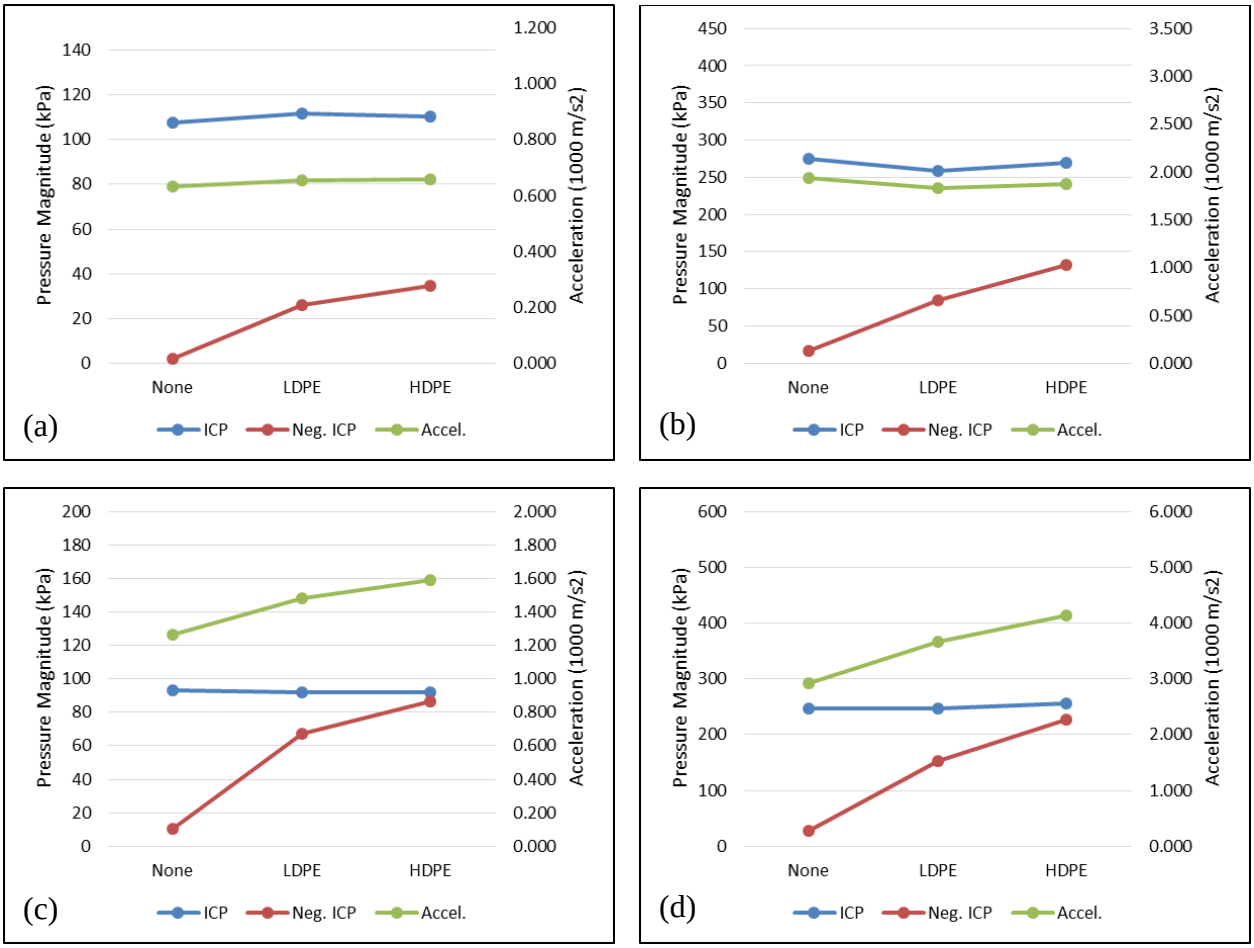

Figure 9.9: Foam material averages for (a) sagittal model at 4 m, (b) sagittal model at 3 m, (c) transverse model at 4 m, and (d) transverse model at 3 m

With regards to the effects of helmet modulus, neither model demonstrated any clear trends (Figure 9.10). There are some slight differences in the average values for each Kevlar material,

more so in the transverse model, but overall the helmet material does not have a significant effect on the model response.

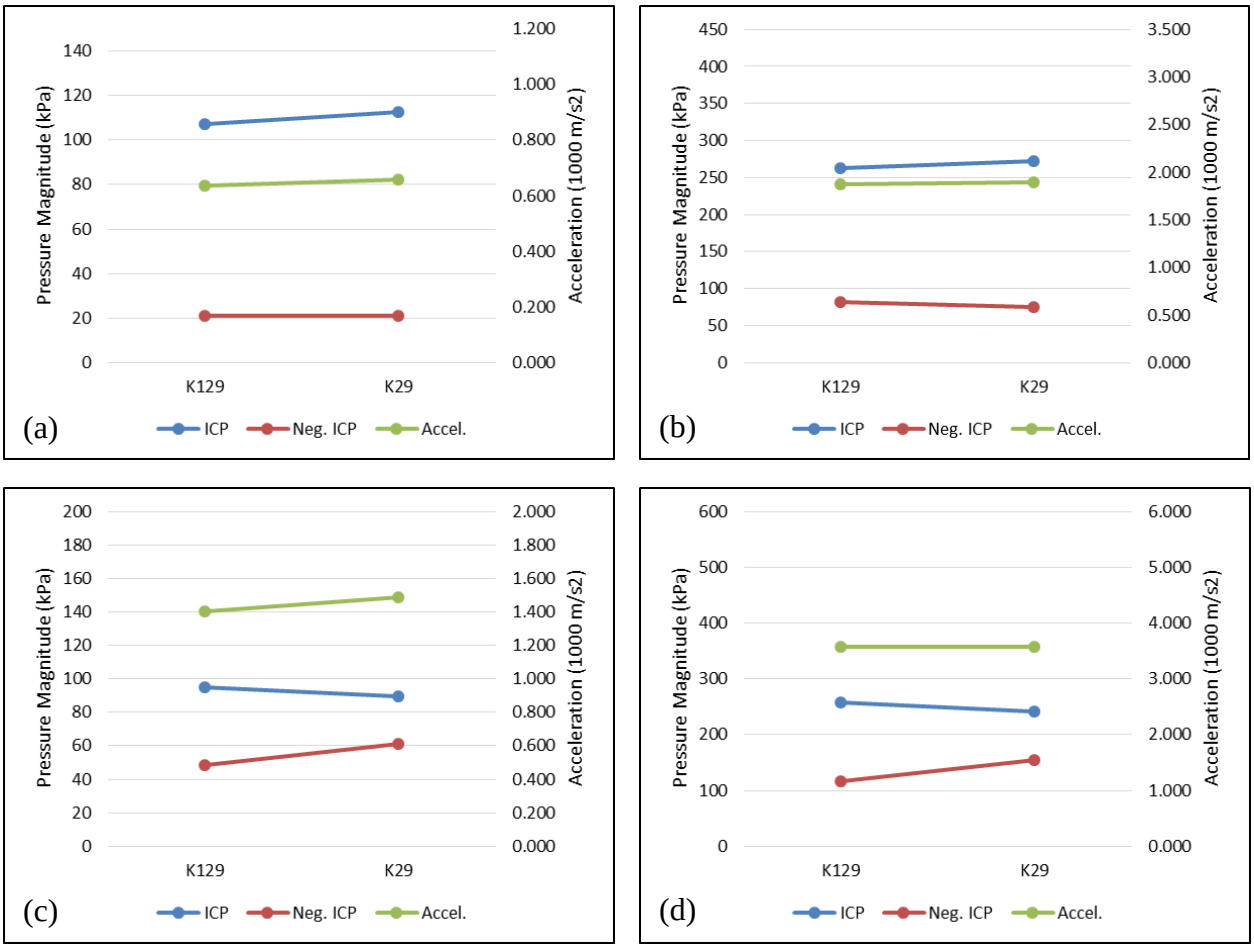

Figure 9.10: Kevlar material averages for (a) sagittal model at 4 m, (b) sagittal model at 3 m, (c) transverse model at 4 m, and (d) transverse model at 3 m

9.2.3 Pathways of Loading

The pathways of loading of the brain tissue for each of the helmet configurations are different, and were investigated in detail to understand how the helmet can affect the brain tissue response in primary blast.

In the sagittal model with a full-visor with a foam lining, the incident wave first impacts the face of the visor and propagates around the lip of the visor while simultaneously loading the helmet shell material near the forehead (Figure 9.11a). The brain tissue sees the first pressure loading from the pathway near the forehead, where the stress wave travels through the foam, and into the brain via the skull material. The wave also has a secondary pathway through the facial tissues as it wraps under the visor (Figure 9.11b). Once the pressure wave travels through the head and reflects off the back of the head in tension, it creates a negative pressure zone at the occipital region (Figure 9.11c, d).

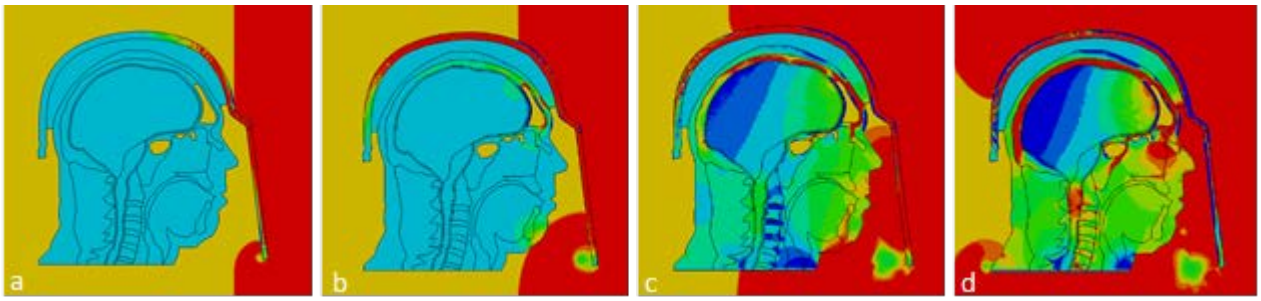

Figure 9.11: Contours of pressure (red is positive, blue is negative) of sagittal model with full-visor and foam lining at a) 0.56 ms, b) 0.67 ms, c) 0.91 ms, and d) 1.17 ms

In the sagittal model with a full-visor and no foam lining, the pathway from the helmet and foam near the forehead is absent, so the primary pathway of loading to the brain is through the facial tissues underneath the visor (Figure 9.12a). As the wave passes through the head and reflects off the back of the head, it produces a negative pressure zone at the occipital region of the brain, although the magnitude of negative pressure is significantly lower than in the case with the foam lining (Figure 9.12c). Additionally, the incident blast wave is able to propagate in the gap between the helmet and the head (Figure 9.12c, d).

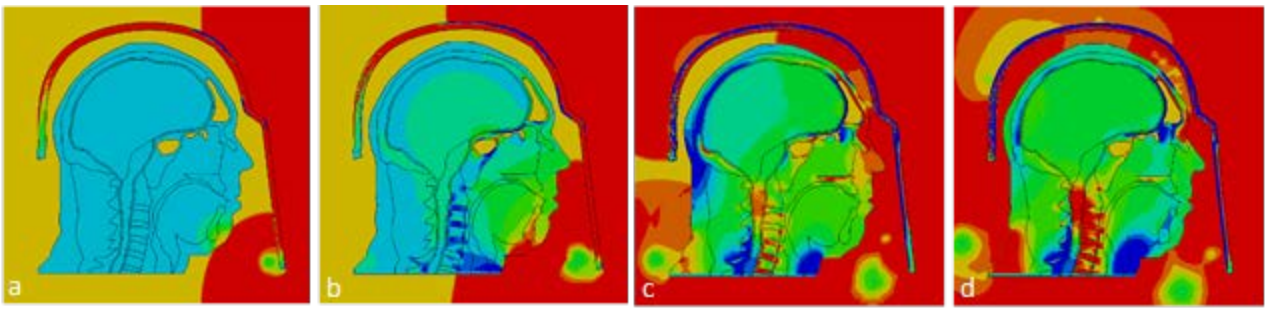

Figure 9.12: Contours of pressure (red is positive, blue is negative) of sagittal model with full-visor and no foam lining at a) 0.67 ms, b) 0.82 ms, c) 1.38 ms, and d) 1.71 ms

In the sagittal model with the half-visor with a foam lining, the pathways of loading are similar to the full-visor, but the pathway through the facial tissues under the visor is significantly more prominent (Figure 9.13b). The negative pressure at the occipital region of the brain can be seen in this configuration as well caused by the tensile reflection of the wave in the head (Figure 9.13c, d).

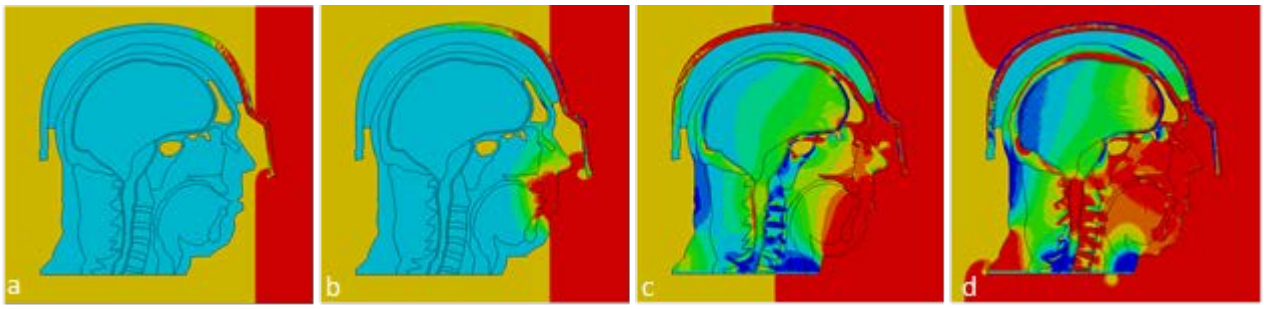

Figure 9.13: Contours of pressure (red is positive, blue is negative) of sagittal model with half-visor and foam lining at a) 0.54 ms, b) 0.60 ms, c) 0.82 ms, and d) 1.10 ms

In the sagittal model with the half-visor and no foam lining, the primary pathway of loading to the brain is through the facial tissues under the half-visor (Figure 9.14a). Again, the occipital region experiences negative pressure after the wave reflection at the back of the head (Figure 9.14b), and the blast wave is able to propagate in the gap between the head and the helmet (Figure 9.14c). In contrast to the full-visor case, the reflected pressures in the gap create

observable increases in the pressure at the parietal and occipital locations (Figure 9.14c, d). This is because the magnitude of the reflected pressure in the gap is greater in the half-visor case since the distance that the reflections have to travel is significantly reduced without the presence of the full-visor.

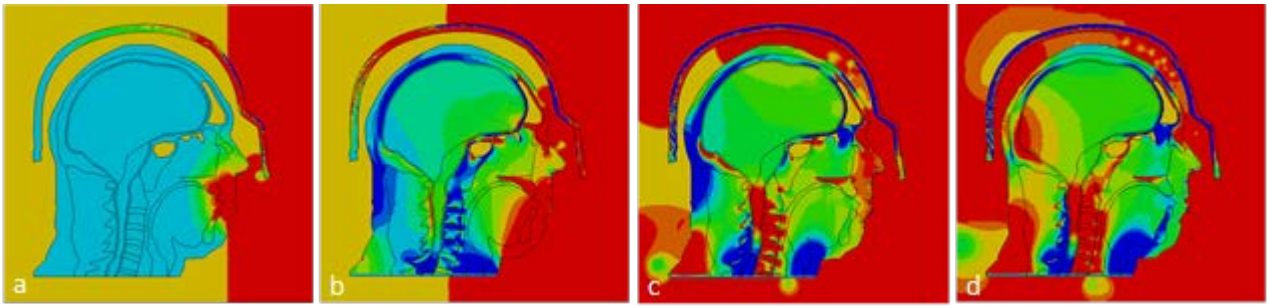

Figure 9.14: Contours of pressure (red is positive, blue is negative) of sagittal model with half-visor and no foam lining at a) 0.60 ms, b) 0.82 ms, c) 1.28 ms, and d) 1.61 ms

In the sagittal model with no visor and with a foam lining, there are two pathways of loading of the stress wave to the brain tissue, through the facial tissues and through the helmet foam (Figure 9.15a), however these are quickly combined due to the close proximity caused by the lack of a visor (Figure 9.15b). The greatest positive pressures in the brain tissue are found closer to the sinuses in this case (Figure 9.15c), as opposed to the cases with the visors, where the greatest positive pressures occur closer to the forehead (Figure 9.11d, Figure 9.13d). This is caused by the interaction of two pathways of loading with each other, which is delayed in the visored cases by the barrier created by the visors.

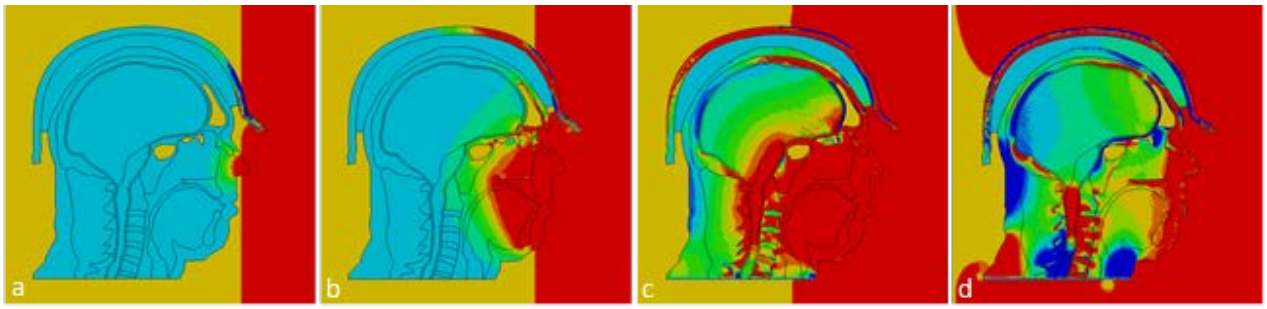

Figure 9.15: Contours of pressure (red is positive, blue is negative) of sagittal model with no visor and foam lining at a) 0.57 ms, b) 0.62 ms, c) 0.76 ms, and d) 1.11 ms

In the sagittal model with no visor and no foam lining, the primary pathway of loading is through the facial tissues and into the brain (Figure 9.16a). Similar to the other no foam cases, the blast wave is able to propagate in the gap between the helmet and head, and results in increased pressures along the parietal and occipital regions of the brain (Figure 9.16c, d).

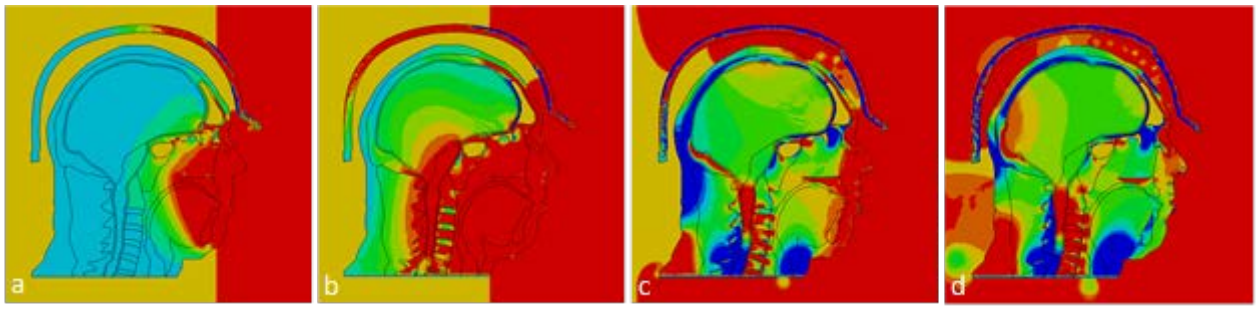

Figure 9.16: Contours of pressure (red is positive, blue is negative) of sagittal model with no visor and no foam lining at a) 0.62 ms, b) 0.76 ms, c) 1.10 ms, and d) 1.38 ms

In the transverse model with a visor and a foam lining, the front of the head is insulated from the blast wave by the visor, so the pathway of loading to the brain tissue is through the helmet material (Figure 9.17a). This creates a mild compressive load on the temporal tissues of the head (Figure 9.17b), which propagates through the head and then reflects in tension and creates a negative pressure loading in the brain tissue (Figure 9.17c, d).

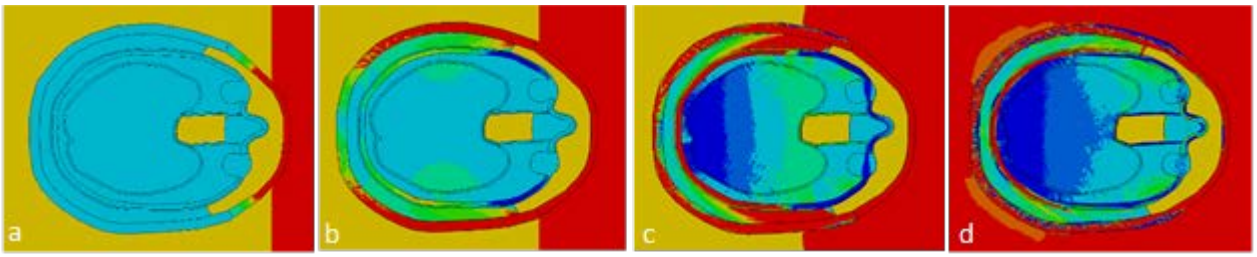

Figure 9.17: Contours of pressure (red is positive, blue is negative) of transverse model with full-visor and foam lining at a) 0.55 ms, b) 0.62 ms, c) 0.71 ms, and d) 1.30 ms

In the transverse model with a visor and no foam lining, the geometry is such that the head model is completely decoupled from the helmet (Figure 9.18). So the only pressure wave that is transmitted to the head has to pass through air gap, which is a very small percentage of the wave due to the high impedance mismatch between the helmet material and the air.

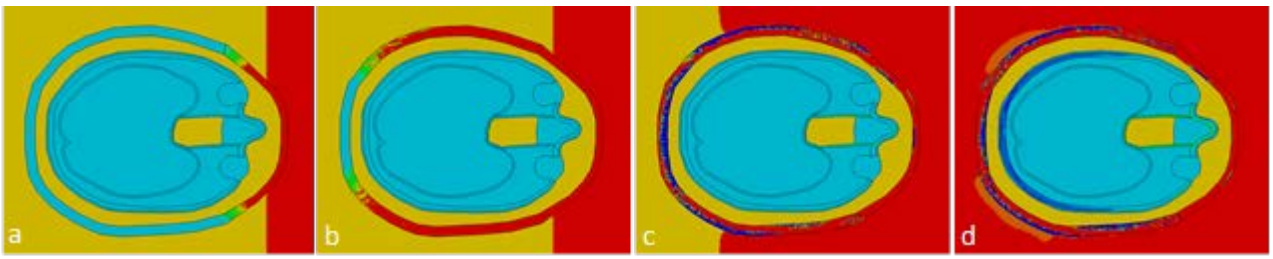

Figure 9.18: Contours of pressure (red is positive, blue is negative) of transverse model with full-visor and no foam lining at a) 0.55 ms, b) 0.61 ms, c) 0.87 ms, and d) 1.29 ms

In the transverse model with no visor and with a foam lining, the incident blast wave is able to transmit directly into the head, which provides the pathway of loading to the brain tissue (Figure 9.19a). The brain tissue sees a compressive pressure zone near the sinus cavity (Figure 9.19b). Later in time, the occipital region experiences a negative pressure zone from the tensile reflection of the wave, similar to the results observed in the sagittal model (Figure 9.19c, d).

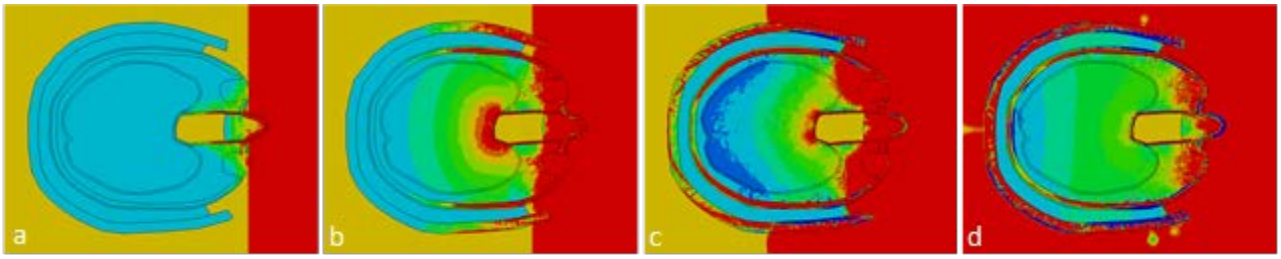

Figure 9.19: Contours of pressure (red is positive, blue is negative) of transverse model with no visor and foam lining at a) 0.58 ms, b) 0.65 ms, c) 0.80 ms, and d) 1.17 ms

In the transverse model with no visor and no foam, the primary pathway of loading is directly into the front of the head since there is no visor (Figure 9.20a), similar to the previous case. Furthermore, the negative pressure zone caused by the reflection can also be observed (Figure 9.20c). However, in this case, the air gap between the helmet and the head is exposed to the incident wave, which results in a significant compressive pressure zone at the occipital region later in time (Figure 9.20d).

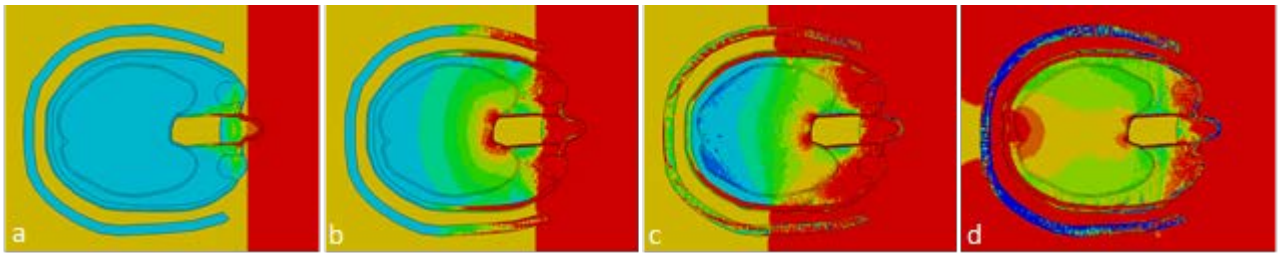

Figure 9.20: Contours of pressure (red is positive, blue is negative) of transverse model with no visor and no foam lining at a) 0.58 ms, b) 0.65 ms, c) 0.80 ms, and d) 1.13 ms

In summary, the pathways of loading of the blast wave to the brain tissue can be significantly affected by the helmet configuration. In general, the presence of a visor significantly hampers the ability of the wave to transmit directly into the brain tissue, although the wave is able to wrap under the visor and load the brain tissue later in time through the facial tissues. While this does lead to some superposition effects in the tissues, the significant wave dispersion through the facial tissues mitigates much of this effect on the brain tissue. Furthermore, the

lack of a foam lining provides an air gap between the helmet and the head, where the blast wave can propagate and in some cases the resulting reflected pressures can generate significant compressive pressures in the parietal and occipital regions of the brain, although the magnitude of these pressures are generally less than the magnitudes of the initial compressive pressures at the frontal regions of the brain. The tensile reflection of the initial compressive wave from the back of the head is generally more significant in cases with a foam lining, due to the portion of the incident blast wave that is transferred to the head through the foam, which causes a greater reflection later in time. This effect is greater in the full-visor case because the remainder of the incident compressive wave is blocked by the visor, and is dispersed by the facial tissues. In contrast, the no-visor case allows the incident compressive wave to transmit through the brain tissue with less obstruction, which mitigates some of the tensile loading caused by the reflection.

9.5 Comparison with Experimental Data

The peak accelerations of the sagittal and transverse models were compared to experimental data provided by Med-Eng for a forward facing mannequin test case [Med-Eng, personal communication] (Figure 9.21). The experiments utilized helmets with a foam lining system, as well as a no foam strap system, and compared peak head accelerations for various incident pressures. The no-visor configuration for the numerical models was used for this comparison

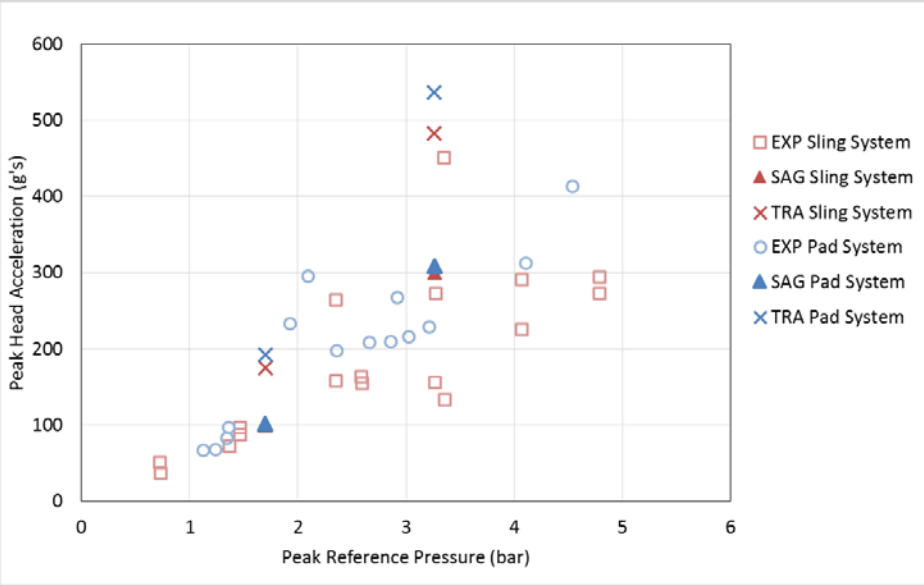

Figure 9.21: Comparison of peak accelerations for sagittal and transverse models (solid symbols) to experimental data (open symbols) for helmeted cases with both sling (no foam) and pad (with foam lining) systems

The experimental data showed no significant difference in peak head accelerations between the strap system and the pad system, although a marginally steeper trend line could be drawn for the pad system. The models also show a similar result, with a minor difference between the strap system and foam configurations, with the foam system resulting in slightly higher accelerations.

In general, the predicted head accelerations of the models were in good agreement with the experimental data, although the transverse model predicted slightly higher accelerations, more so at higher pressures. Interestingly, the scatter in the experimental data is greater at greater incident pressures, in agreement with the experimental scatter observed with the experimental validation data on head acceleration presented in Section 7.4.1, which is likely due to fireball and other non-linear effects that become significant with greater intensity blast loadings.

10. Discussion

This study used two finite element blast head models in the sagittal and transverse planes to investigate the nature of primary blast injury to the head and brain, and possible mitigation strategies using different helmet configurations. The discussion of the results is separated in the following sections for the general brain tissue response from primary blast, and the effects of helmets on brain tissue response.

10.1 Brain Tissue Response Discussion

The sagittal and transverse models were investigated in terms of both global and local tissue response metrics for three representative blast load cases corresponding to experimental tests conducted at DRDC Valcartier. The models were validated in terms of head acceleration and HIC_{15} using experimental data on Hybrid III headforms conducted by DRDC Valcartier. The peak head acceleration values predicted by the models were in good agreement with the experimental data, and followed the expected trends of increasing response with decreasing standoff distance. The HIC_{15} results of the models were in reasonable agreement with the experimental data, although not as sensitive to changing blast load severity as the experimental data indicated. Specifically, the models moderately overpredicted the HIC_{15} values for the 3.5 and 4 m standoffs, while underpredicting the response for the 3 m standoff. The large amount of scatter in the data for the lower standoff distance (attributed to close range fireball effects) may account for some of this difference.

The models were able to accurately predict head kinematics resulting from primary blast effects. Since the blast pressure wave is well approximated as a planar wave, the bulk of the loading on the head will be translational, and the acceleration response is primarily linear, as shown in previous studies utilizing full body models in blast [Cronin et al. 2008, Lockhart et al. 2012, Haladuick et al. 2011, Haladuick et al. 2012]. The density of the tissues, as defined by the constitutive models, as well as the pressure force applied by the blast wave, are as accurate in the sagittal and transverse models as in a three-dimensional model. Since the kinematic response is determined by mass and force, these models can correctly simulate the kinematic response expected in the head/brain assembly during the initial wave interaction. Furthermore, the time scale of the blast events modeled was on order of milliseconds, prior to significant bulk motion of head where the boundary conditions of the models may not be applicable.

In the context of blast injury and the current study, HIC_{15} is primarily used as a comparative measure to evaluate the head kinematics resulting from primary blast via the automotive threshold. The usefulness of HIC in predicting injury from blast has not been validated. Since HIC was developed specifically for head injuries from automotive impacts, it is limited with regards to blast injury prediction in a number of ways. Mainly, the durations of loading in typical automotive impacts are significantly greater than primary blast, and since the HIC value was calculated from a time integral of the acceleration curve, it was sensitive to loading duration. Furthermore, the mechanism of injury from primary blast loading to the head is quite different than automotive impact related head injuries, so the relationship between kinematics and injury may be different in the two loading types. Therefore, the HIC_{15} values reported in the current study should be treated as comparative benchmarks, and not as injury predictors.

In addition, the intracranial pressure response of the models was validated using experimental data on shock tube tests performed using post mortem human subject heads. Although the mode of loading was relevant to the current study, the pressure magnitude was lower and duration longer compared to the blast cases investigated. This is common for shock tube testing. The models provided good agreement with the experimental intracranial pressure traces at the frontal, parietal, and temporal locations, although were not able to capture three dimensional wave effects that affect the pressures at the occipital region of the brain. Overall, the sagittal and transverse models were able to accurately predict peak pressures and accelerations experienced in primary blast.

The wide range of viscoelastic material properties available for brain tissue in the literature prompted an investigation into the effects of the different parameters on the model response. This investigation revealed that varying the viscoelastic parameters of the brain tissue significantly affected the predicted strains, but did not affect the strain rates or intracranial pressures. This makes sense considering the consistency of the bulk modulus for brain tissue in the literature, which defines the bulk (hydrostatic) behaviour of the models that determines the pressures.

In terms of local tissue response, the models were investigated in terms of first principal strain and intracranial pressures for the three blast load cases. The sagittal and transverse models report peak principal strains of 0.035 to 0.062 and 0.053 to 0.087 respectively. Furthermore, strains near these magnitudes were only experienced by about 10% of the brain volume, with the remainder experiencing significantly smaller values. In comparison to the available threshold values of principal strain in the literature, the strains predicted by the models are generally low. The existing principal strain injury criteria, albeit not developed for blast, range between 0.19 to 0.40 (Section 4.3.2), significantly greater than the maximum strains seen in the models even in the most severe

blast load case considered. These low values of strain are expected in primary blast due to the short duration of loading, which does not provide enough time for significant motion of the tissues.

While the strains reported by the models in primary blast are small, the strain rates are significantly greater than those seen in typical automotive or blunt impact scenarios. The sagittal and transverse models reported peak effective strain rates in the brain tissue of between 226 and 571 s^{-1} for the three load cases considered. In contrast, typical strain rates in automotive impacts can vary from 10 – 100 s^{-1} [Deck 2008, Danelson et al. 2008]. Large strain rates are expected in primary blast scenarios where the loading is rapidly applied and durations are short, and are in agreement with the literature [Sista 2011, Shafieian et al. 2011].

The models report that significant levels of intracranial pressure, on the order of several atmospheres, can be generated in the brain tissue during primary blast exposure. The peak pressures in the brain tissue for both models typically exceeded the existing injury thresholds for intracranial that are available in the literature. However, these existing criteria were generally developed for automotive crash scenarios, so may not be suitable for the injury mechanisms relevant to blast. In addition, it remains unclear what contribution the amount of brain tissue exposed to high levels of pressure has on the potential for injury. The sagittal and transverse models demonstrate that the highest levels of pressure are experienced by a relatively small percentage of the brain, with the majority experiencing significantly lower values.

A significant observation in the models is the reflection of the incident compressive wave from the back of the head which generates negative, or tensile, pressures in the brain tissue. The presence of large magnitudes of negative pressure near the brain tissue has been hypothesized to cause injury through cavitation of the cerebrospinal fluid [Wardlaw 2010, Goeller et al. 2012].

The sagittal and transverse models suggest that cavitation is certainly a possibility in primary blast, as the peak negative pressures reached magnitudes on the order of several atmospheres, although the cavitation pressure of CSF has not been measured and there is no direct empirical evidence of cavitation induced injury in the literature.

In evaluating the trends reported by the models for various tissue response metrics, intracranial pressure demonstrated a greater sensitivity to changes in the applied blast load. The magnitudes of ICP increased significantly with increasing blast load severity, while changes in principal strain were relatively small, and peak strains were low in all three load cases. Although strain has been used as an injury predictor in the literature [Kleiven 2008, Deck 2008, Mao 2011], existing thresholds have been generally developed for lower rate applications such as automotive crash. However, blast loads are inherently high rate, so any strain-based injury criteria needs to take into account strain rate to be fully representative of the loading. In contrast, intracranial pressure is a direct measure of the transient waves within the head, and therefore may be a more appropriate injury response metric for blast injury.

Notwithstanding the appropriateness of intracranial pressure as a response injury metric, the lack of well-defined brain injury criteria for blast is a major limitation of the literature. The current study focused on relating external loading (kg C4 and standoff distance) to head kinematics and internal tissue response, and compared the model response at each load case. This provided a benchmark model response, upon which helmet protection configurations could be evaluated. An attempt was made to avoid explicitly relating model response to injury, as the lack of injury criteria for blast mTBI prevents such conclusions.

The main limitation of the models presented in this study is the lack of three dimensional effects captured by the models. The effects of this were investigated with the three dimensional ellipsoid model in Section 7.5. Another limitation of the models is that the results are valid only for the time and loading regimes relevant to primary blast injury. In the field, blast waves are usually complex waves, and exposure is often compounded by secondary or tertiary effects, which can affect the loadings on the head and subsequent likelihood of injury. The sagittal and transverse models presented in this work are only valid for the interaction of the primary blast wave with the head, and cannot capture secondary or tertiary effects that occur later in time and are influenced by bulk motion of the head.

10.2 Helmet Protection Discussion

The sagittal and transverse models were outfitted with various helmet configurations and materials to investigate the influence of helmet visors, foam lining presence and density, and Kevlar material stiffness on the protective properties of the helmet. The peak head accelerations and intracranial pressures were compared for a low and high intensity blast load. The sagittal model demonstrated a reduction in head acceleration with a helmet, and further reductions with the visored cases, whereas the transverse model demonstrated a reduction in head acceleration only for the visored case. The head acceleration was reduced in the sagittal model because the geometry of the helmet generally followed the curvature of the head and did not significantly change the incident wave propagation, while adding additional mass to the system which kinematically reduced the acceleration. In the transverse model with a helmet and no visor, the geometry of the helmet was such that it captured more of the incident wave, which actually increased the peak acceleration. Differences between the sagittal and transverse models were expected, and were indicative of the significant differences in the geometry of head in the two orthogonal planes. The reduction of

head acceleration with the presence of the helmet is generally in agreement with previous studies that have considered this issue [Dionne et al. 2002, Panzer et al. 2010, Lockhart et al. 2014].

The sagittal model reported reduced positive intracranial pressures for the helmeted cases, and additional reduction for the visored cases, in agreement with findings from previous studies [Jason 2010, Nyein et al. 2010]. In contrast, the transverse model demonstrated a significant reduction is positive ICP for the visored cases, and a slight increase in ICP for the non-visored cases, attributed again to the geometry of the non-visored helmet in the transverse plane. Interestingly, the full-visor case with foam lining increased the negative intracranial pressures for both the sagittal and transverse models. This was attributed to the fact that the full-visor with a foam lining still allowed for direct wave transmission of a portion of the incident blast wave into the head through the foam lining, which reflected in tension causing negative pressures. However, the presence of the visor obstructed the remainder of the incident wave from transmitting into the brain tissue and mitigating some of the tensile reflection through superposition, as was the case for the half-visor and no-visor cases. This effect was not present in the cases with no foam lining, because the air gap between the helmet and the head prevented any significant wave transmission between the helmet and the head.

The effects of the foam lining material were not as significant to the model response as the helmet visor configurations, but did demonstrate some important trends. The sagittal model predicted that the configuration with no foam resulted in a slight reduction in positive ICP for the lower intensity blast load, but identified a slight increase in ICP for the higher intensity blast load. This suggests that reflections in the air gap between the helmet and head may be more significant in amplifying intracranial pressures at higher blast overpressures. Grujicic et al. [Grujicic et al. 2011] similarly

concluded that the influence of the foam material is greater for higher intensity loads. The greatest influence of the foam material was on the negative intracranial pressure response of the models, where the no foam case resulted in significantly reduced negative ICPs, followed by the low density foam and the high density foam. This is because the greatest negative pressures are at the occipital regions of the brain, which are more influenced by the foam material impedance properties than the frontal regions, where the compressive (positive) ICPs are greatest. The no foam case corresponded to the greatest reduction in negative ICP because the portion of the incident wave that was transmitted to the helmet was decoupled from the head, so the contribution to the tensile reflection from the back of the head was eliminated. The effects of the helmet Kevlar material stiffness were not significant in any of the cases.

The sagittal and transverse models demonstrate the 'underwash' effect in the case with no foam lining between the helmet and the head, where the pressure is increased in the air gap due to pressure wave reflections. These reflections caused a noticeable increase in the pressures experienced by the adjacent brain tissue. However, these increased pressures were generally lower than or of similar magnitude to the peak compressive pressures at the anterior of the brain during initial blast wave impact. These findings were consistent with the conclusions of Moss et al., who reported that the underwash effect can amplify the pressures in the air gap under the helmet, although they did not specifically report on the effects of this on the resulting intracranial pressures [Moss et al. 2009].

11. Conclusions

The primary conclusions from this work are presented here. It is important to note that the conclusions presented below are within the scope of the current work and within the limitations of the models presented herein. Specifically, they are limited to primary blast interaction with the head in free-field blast load conditions. In reality, combat helmet designers have more factors to consider including ballistic protection, blunt impact protection, ergonomics, and compatibility, among others.

1. Fully coupled Lagrangian-ALE sagittal and transverse finite element models with element sizes sufficient to accurately model wave dynamic in the tissues of the head and brain, are capable of predicting kinematic and intracranial pressures in primary blast loading. This is demonstrated by the good agreement with experimental data (Section 7.4), and the three dimensional ellipsoid verification study (Section 7.5).

2. The intracranial strains predicted by the models depend strongly on the shear modulus of the brain tissue constitutive parameters, which vary widely in the literature. In contrast, neither the strain rate nor the intracranial pressures vary significantly with varying mechanical properties.

3. The models have established that strains experienced in the brain tissue in primary blast are generally one order of magnitude lower, whereas strain rates are one order of magnitude higher, than traditional automotive or impact cases.

4. Significant positive (compressive) and negative (tensile) pressures can be generated in the brain tissue during primary blast. The greatest positive pressures are at the frontal regions where the incident blast wave makes contact with the head. The greatest negative pressures are at the occipital regions where the compressive wave is reflected off the back of the head in tension.

5. All response metrics follow the trend of increasing response with increased blast load severity. However, intracranial pressure demonstrates the greatest sensitivity to loading, as compared with HIC or strain, suggesting that intracranial pressure is a more appropriate injury response metric in primary blast.

6. The presence of a helmet visor significantly reduces both the peak head acceleration and the positive intracranial pressures, although can increase the negative pressures at the occipital region of the brain in cases where there is foam lining.

7. A lower density foam performs better than higher density foam in reducing acceleration and intracranial pressures for high intensity blast loads, while no foam lining performs marginally better in reducing positive ICP for lower intensity loads.

8. The helmet shell Kevlar material stiffness has no significant effect on mitigation.

9. In cases where there is no foam lining, pressure wave reflections in the air gap between the helmet and head can cause greater intracranial pressures in adjacent brain tissue, although the magnitudes of these increased pressures are generally lower than or of similar magnitude to the incident compressive pressures caused by the initial wave impact.

12. Recommendations

The recommendations for further work in this field of study are listed as follows.

1. The effects of head orientation on model response should be investigated. Rear impact, side impact, top impact, and oblique impact blasts are common in the field, and may change the pathways of loading to the brain and the resultant tissue response. The current study only considered frontal impact blast loading.

2. The effects of complex blast waves and ground interaction should be investigated. Ground interaction with a height of burst can create a double peak profile in the incident blast wave depending on the height and standoff, which can affect the model response. Furthermore, the effects of the Mach stem at relevant standoffs should be investigated. The current study was limited to free-field blast wave profiles.

3. The current study and conclusions are relevant only for the first 2 ms that was deemed relevant for primary blast. However, it is possible that the longer duration response may also be important, so this should be investigated.

4. A parametric study was conducted to investigate various parameters of helmet configuration on model response. This should be continued to investigate parameter optimization, to determine specifically which configuration results in the highest degree of protection.

5. A very important next step in this work and related work is to relate model response with injury. This is dependent on available and well-defined injury criteria, which are currently

unclear for blast related brain injury. However, this is a very active field of research, which may provide new data on primary blast injury in the near future.

References

Abolfathi N, Naik A, Chafi MS, et al. (2009) “A micromechanical procedure for modeling the anisotropic mechanical properties of brain white matter”, *Computer Methods in Biomech and Biomed Eng*; **12(3)**:249–262, DOI: 10.1080/10255840802430587.

Abolfathi N et al. (2008) “Diffuse axonal injury and degradation in mechanical characteristics of brain white matter” *Proceedings of the ASME 2008 Summer Bioengineering Conference*, Marco Island FL, USA, 2008.

Abney TM, Feng YA, Pless R, et al. (2010) “Principal components of brain deformation in response to skull acceleration: the roles of sliding and tethering between the brain and skull”, *IFMBE Proceedings*, **32**:9-12.

Alley MD, Schimizze BR, Son SF. (2011) “Experimental modeling of explosive blast-related traumatic brain injuries”, *Neuroimage*, **54**:S45-S54.

ASME, American Society of Mechanical Engineers (2006) “Guide for Verification and Validation in Computational Solid Mechanics”, *Standards*, V V 10-2006.

Axelsson H, Yelverton JT. (1996) “Chest Wall Velocity as a Predictor of Nonauditory Blast Injury in a Complex Wave Environment”, *Journal of Trauma*, **40**:3.

Azevedo FAC, Carvalho LRB, Grinberg LT, et al. (2009) “Equal numbers of neuronal and nonneuronal cells make the human brain isometrically scaled-up primate brain”, *The Journal of Comparative Neurology*, **513**:532-541.

Bain AC, Meaney DF. (2000) “Tissue-level thresholds for axonal damage in an experimental model of central nervous system white matter injury”, *J Biomech Eng*, **16**:615-622.

Balakathiresan N, Bhomia M, Chandran R, et al. (2012) “MicroRNA Let-7i is a promising serum biomarker for blast-induced traumatic brain injury”, *J Neurotrauma*, **29**:1379-1387.

Bandak FA, vander Vorst MJ, Stuhmiller LM, et al. (1995) “An imaging-based computational and experimental study of skull fracture: Finite element model development”, *Journal of Neurotrauma*, **12**(4):679-688.

Bass CR, Rafaels KA, Salzar RS. (2008) “Pulmonary injury risk assessment for short-duration blasts” *The Journal of Trauma*, **65**(3):604-615.

Baumgartner D, Lamy M, Willinger R et al. (2009) “Finite element analysis of traumatic brain injuries mechanisms in the rat”, *IRCOBI Conference*, York (UK), September 2009.

Bayly PV, Cohen TS, Leister EP, Ajo D, et al. (2005) “Deformation of the human brain induced by mild acceleration”, *Journal of Neurotrauma,* **22**(8):845–56.

Belytschko T, Liu WK, Moran B. (2000) “Nonlinear Finite Elements for Continua and Structures”, West Sussex: John Wiley & Sons Ltd.

Bhattacharjee Y. (2008) “Shell shock revisited: solving the puzzle of blast trauma”, *Neuroscience*, **319**:406-408.

Bioux R, Viot P, Lataillade JL. (2009) “Polypropylene foam behaviour under dynamic loadings: strain rate, density, and microstructure effects”, *Int J Impact Engineering*, **36**:329-342.

Bir C. (2011) “Measuring Blast-Related Intracranial Pressure within the Human Head”, *U.S. Army Medical Research Award Number W81XWH-09-1-0498*.

Bolander R, Mathie B, Bir C et al. (2011) “Skull flexure as a contributing factor in the mechanism of injury in the rat when exposed to a shock wave”, *Annals of Biomedical Engineering* 2011; **39**(10):2550–9.

Bonet J, Burton AJ. (1998) “A simple average nodal pressure tetrahedral element for incompressible and nearly incompressible dynamic explicit applications”, *Communications in Numerical Methods in Engineering*, **14**(5):437-449.

Bowen IG, Fletcher ER, Richmond DR. (1968) “Estimate of man’s tolerance to the direct effects of air blast,” *Headquarters Defense Atomic Support Agency*, Washington DC.

Brainmind (online). “Head Injuries – Stroke – Neuroscience”. Date accessed: Nov 11, 2014. < http://brainmind.net/BrainLecture11.html>.

Bulson PS. (1997) “Explosive Loading of Engineering Structures”, New York: Taylor & Francis.

Canadian Forces Combat Helmet User Manual 8470-21-912-7719 (online). Date accessed: Nov 11, 2014. <http://www.mats-helmets.se/Manuals/ca-cg634/ca-cg634.html>.

Cernak I, Merkle AC, Koliatsos VE, et al. (2011) “The pathobiology of blast injuries and blast-induced neurotrauma as identified using a new experimental model of injury in mice”, *Neurobiology of Disease*, **41**:538-551.

Cesari D, Compigne S, Scherer R, et al. (2001) “WorldSID Prototype Dummy Biomechanical Responses”, *Stapp Car Crash Journal*, **45**:285-318.

Chafi MS, Karami G, Ziejewski M. (2010) “Biomechanical assessment of brain dynamic responses due to blast pressure waves”, *Annals of Biomedical Engineering*, **38**(2):490–504.

Chafi MS, Ganpule S, Gu L, et al. (2011) “Dynamic response of brain subjected to blast loadings: Influence of frequency ranges”, *International Journal of Applied Mechanics*, **3**(4): 803–823.

Chase, K. (2003) “Firearms: A Global History to 1700”. Cambridge University Press.

Christ AF, Franze K, Gautier H, et al. (2010) “Mechanical difference between white and gray matter in the rat cerebellum measured by scanning force microscopy”, *J Biomechanics*, **43**:2986-2992.

Christensen RM. (1982) “Theory of Viscoelasticity, Second Edition”, Mineola, NY, USA: Dover Publications.

Clemedson CJ. (1956) “Blast injury” *Physiological Reviews*, **36**(3):336-354.

CMP (online). “Canadian Forces Military Police Branch – Helmets”. Date accessed: Nov. 11, 2014. <http://www.mpmuseum.org/securhelmet.html>.

Coleman AJ, Kodoma T, Choi MJ, et al. (1995) “The cavitation threshold of human tissue exposed to 0.2-MHz pulsed ultrasound: preliminary measurements based on a study of clinical lithotripsy”, *Ultrasound in Med. & Biol*, **21**(3):405-417.

Connolly TJM, Clutter JK. (2010) “Criteria to determine likelihood of brain injury during explosive events”, *Safety Science*, **48**(10):1387-1392.

Cooper GJ, Dudley HAF, Gann DS, et al. (1997) “The Scientific Foundations of Trauma”, Oxford, UK: Butterworth-Heineman.

Cronin DS, Salisbury C, Binette JS, et al. (2008) “Numerical modeling of blast loading to the head”, *Proc. PASS*, Brussels, Belgium, 2008, 84-93.

Cronin DS. University of Waterloo ME720 Course Notes.

Danelson KA, Geer CP, Stitzel JD, et al. (2008) “Age and gender based biomechanical shape and size analysis of the pediatric brain”, *Stapp Car Crash Journal*, **52**(Nov):59–81.

Deck C, Willinger R. (2008) “Improved head injury criteria based on head FE model”, *International Journal of Crashworthiness*, **13**(6):667–678.

Dionne JP, Nerenberg J, Makris A. (2002) “Reduction of Blast-Induced Concussive Injury Potential and Correlation with Predicted Blast Impulse”, *Med-Eng Sys. Inc*, Ottawa, Canada.

Effgen GB, Vogel E, Lynch KA, et al. (2013) “In vitro primary blast injury induces cell death in the hippocampus”, *IRCOBI Conference*, IRC-13-65.

El Sayed T, Mota A, Fraternali F, et al. (2008) “Biomechanics of traumatic brain injury”, *Comput Methods Appl Mech Engrg*, **197**:4692-4701.

Elder GA, Cristian A. (2009) “Blast-related mild traumatic brain injury: mechanisms of injury and impact on clinical care”, *Mount Sinai Journal of Medicine*, 76:111-118.

Elkin BS, Morrison B. (2007) “Region-specific tolerance criteria for the living brain”, *Stapp Car Crash Journal*, **51**(October).

Elkin BS, Ilankova A, Morrison B. (2011) “Dynamic, regional mechanical properties of the porcine brain: indentation in the coronal plane”, *J Biomechanical Engineering*, **133**(July).

“Enhanced Combat Helmet (ECH)” *Navy Programs*, <http://operationhelmet.org /documents/2012ech.pdf>.

Feng YA, Abney TM, Okamoto RJ, et al. (2010) “Relative brain displacement and deformation during constrained mild frontal head impact”, *Journal of the Royal Society, Interface*, **7**(53):1677–88.

Finan JD, Elkin BS, Pearson EM, et al. (2012) “Viscoelastic properties of the rat brain in the sagittal plane: Effects of anatomical structure and age”, *Annals of Biomedical Engineering*, **40**(1):70-78.

Folgar F, Scott BR, Walsh SM, et al. (2007) “Thermoplastic matrix combat helmet with graphite-epoxy skin”, *23rd International Symposium on Ballistics*, Tarragona, Spain, April 2007.

Freund J, Brandmaier AM, Lewejohann L, et al. (2013) “Emergence of individuality in genetically identical mice”, *Science*, **340**:756-759.

Gadd CW. (1966) “Use of a weighted-impulse criterion for estimating injury hazard”, *SAE Technical Paper 660793*.

Galarneau MR, Woodruff SI, Dye JL, et al. (2008) “Traumatic brain injury during Operation Iraqi Freedom: findings from the United States Navy-Marine Corps Combat Trauma Registry”, *J Neurosurg*, **108**:950-957.

Ganpule S, Gu L, Cao G, et al. (2009) “The effect of shock wave on a human head”, *Proceedings of IMECE2009*, Lake Buena Vista, Florida, USA, November 2009.

Ganpule S, Gu L, Alai A, et al. (2012) “Role of helmet in the mechanics of shock wave propagation under blast loading conditions” *Computer Meth Biomech and Biomed Eng*, **15**(11):1233-1244.

Ganpule SG. (2013) “Mechanics of blast loading on post-mortem human and surrogate heads in the study of traumatic brain injury (TBI) using experimental and computational approaches”, *PhD Dissertation*, University of Nebraska.

Gayzik FS, Moreno DP, Vavalle NA, et al. (2012) “Development of the Global Human Body Models Consortium mid-sized male full body model”, *Injury Biomechanics Research, Proceedings of the 39th International Workshop*.

Gehre C, Gades H, Wernicke P. (2009) “Objective rating of signals using test and simulation responses”, *In: Enhanced Safety of Vehicles*, Stuttgart, Germany.

Gekhman D. (2006) “Mass of a Human Head”, *The Physics Factbook*, <http://hypertext-book.com/facts/2006/DmitriyGekhman.shtm>.

Gennarelli TA, Pintar FA, Yoganandan N. (2003) “Biomechanial Tolerances for Diffuse Brain Injury and a Hypothesis for Genotypic Variability in Response to Trauma”, *Annu. Proc. Assoc. Avd. Automot. Med*, **4**:624–628.

Gibson LJ, Ashby MF. (1997) “Cellular Solids: Structure and Properties, Second Edition”, Cambridge University Press.

Goel R. (2011) “Study of an advanced helmet liner concept to reduce TBI: experiments & simulation using sandwich structures”, *MASc. Thesis*, Massachusetts Institute of Technology.

Goeller J, Wardlaw A, Treichler D, et al. (2012) “Investigation of cavitation as a possible damage mechanism in blast-induced traumatic brain injury”, *J Neurotrauma*, **29**(10):1970-1981.

Gogineni S, Gao XL, David NV, et al. (2012) “Ballistic impact of Twaron CT709® plain weave fabrics”, *Mech Adv Mater Struct*, **19**(6):441-452.

Gower HL, Cronin DS, Plumtree A. (2008) “Ballistic impact response of laminated composite panels”, *Int J Impact Engineering*, **35**:1000-1008.

Green MA, Bilston LE, van Houten E, et al. (2008) “In vivo brain viscoelastic properties measured by magnetic resonance elastography”, *NMR in Biomedicine*, **21**(7):755-764.

Greer AD. (2006) Numerical Modeling for the Prediction of Primary Blast Injury to the Lung. *MASc Thesis*, University of Waterloo, Waterloo, Canada.

Grujicic M, Bell WC, Pandurangan B, et al. (2010a) "Blast-wave impact-mitigation capability of polyurea when used as helmet suspension-pad material", *Materials and Design*, **31**:4050-4065.

Grujicic M, Arakere G, He T. (2010b) "Material-modeling and structural-mechanics aspects of the traumatic brain injury problem", *Multidiscipline Mod Mat Struct*, **6**(3):335-363.

Grujicic M, Bell WC, Pandurangan B, et al. (2011) "Fluid/Structure interaction computational investigation of blast-wave mitigation efficacy of the advanced combat helmet", *Journal of Materials Engineering and Performance*, **20**(6):877-893.

Haladuick TN, Lockhart PA, Singh D, Cronin DS. (2011) "Modeling of global head kinematics resulting from realistic blast loading", *IASTED Biomech*, Pittsburgh, PA, November 2011.

Haladuick TN, Lockhart PA, Singh D, Cronin DS. (2012) "Head Kinematics Resulting from Simulated Blast Loading Scenarios", *Proc. PASS*, Nuremberg, Germany, 2012.

Hallquist JO. (2006) "LS-DYNA Theory Manual", *Livermore Software Technology Corporation*, Livermore, CA. ISBN 0-9778540-0-0.

Hamhaber U, Sack I, Papazoglou S, et al. (2007) "Three dimensional analysis of shear wave propagation observed by in vivo magnetic resonance elastography of the brain", *Acta Biomaterialia*, **3**(1):127-137.

Hartmann P, Ramseier A, Gudat F, et al. (1994) "Normal weight of the brain in adults in relation to age, sex, body height and weight", *Patholoģe*, **15**(3):165-170.

Herbert E, Balibar S, Caupin F. (2006) "Cavitation pressure in water", *Phys Rev E Stat Nonlin Soft Matter Phys*, **74**(4):1–22. DOI: 10.1103/PhysRevE.74.041603.

Hooker DR. (1924) "Physiological effects of air concussion" *American Journal of Physiology*, **67**(2):219-274.

Hole JW. (1984) "Human Anatomy and Physiology, 3rd Edition", Dubuque: Wm. C. Brown Publishers. ISBN 0-697-04790-3.

Hori H, Moretti G, Rebora A, et al. (1972) "The thickness of the human scalp: Normal and bald", *The Journal of Investigative Dermatology*, **58**(6):396-399.

Houff CW, Delaney JP. (1973) "Historical documentation of the infantry helmet research and development", *US Army Human Engineering Laboratory Technical Memorandum 4-73*.

Hutchinson J. (1998) “The Head Injury Criterion (HIC) functional”, *Applied Mathematics and Computation*, **96**(1):1-16.

Hrapko M, van Dommelen JA, Peters GW et al. (2008) “The influence of test conditions on characterization of the mechanical properties of brain tissue”, *J Biomech Eng*, **130**(3).

Ipek H, Mayer C, Deck C, et al. (2009) “Coupling of Strasbourg University Head Model to THUMS Human Body FE Model: Validation and Application to Automotive Safety”, *21st Inter. Tech. Conf. on the Enhanced Safety of Vehicles*, Stuttgart, Germany.

Jean A, Nyein MK, Zheng JQ, et al. (2014) “An animal-to-human scaling law for blast-induced traumatic brain injury risk assessment”, *Proceedings of the National Academy of Sciences*, **111**(43).

Jin X, Zhu F, Mao H, et al. (2013) “A comprehensive experimental study on material properties of human brain tissue”, *J Biomechanics*, **36**:2795-2801.

Kaster T, Sack I, Samani A. (2011) “Measurement of the hyperelastic properties of ex vivo brain tissue slices”, *J Biomechanics*, **44**:1158-1163.

Kay T, Harrington DE, Adams R, et al. (1993) “Definition of mild traumatic brain injury”, *J Head Trauma Rehabil*, **8**(3):86-87.

Kingery CN, Bulmash G. (1984) “Airblast parameters from TNT spherical air burst & hemispherical surface burst”, *Tech Report ARBRL-TR-02555*.

Klatt D, Hamhaber U, Asbach P, et al. (2006) “Noninvasive assessment of the rheological behaviour of human organs using multifrequency mr elastography: a study of brain and liver viscoelasticity”, *Physics in Medicine and Biology*, **52**(24):72-81.

Kleiven S. (2008) “Biomechanics and thresholds for MTBI in humans”, *MTBI Pre-Congress Symposium, IBIA Congress*, Lisbon, Portugal.

Kulkarni SG, Gao XL, Horner SE, et al. (2013) “Ballistic helmets – their design, materials, and performance against traumatic brain injury”, *Composite Structures*, **101**:313-331.

Kumaresan S, Radhakrishnan S. (1996) “Importance of partitioning membranes of the brain and the influence of the neck in head injury modeling”, *Medical & Biological Engineering and Computing*, **34**:27-32.

Lee MC, Haut RC. (1989) “Insensitivity of tensile failure properties of human bridging veins to strain rate: implications in biomechanics of subdural hematoma”, *J Biomech*, **22**(6/7):537-542.

Lee KYK, Nyein MK, Moore DF, et al. (2011) “Blast-induced electromagnetic fields in the brain from bone piezoelectricity”, *Neuroimage*, **54**:S30-S36.

Lee SJ, King MA, Sun J, et al. (2014) “Measurement of viscoelastic properties in multiple anatomical regions of acute rat brain tissue slices”, *J Mech Behaviour of Biomed Materials*, **29**:213-224.

Leonardi ADC, Bir C, Ritzel DV, et al. (2011) “Intracranial pressure increases during exposure to a shock wave”, *Journal of Neurotrauma*, **28**:85–94

Lockhart PA. (2010) “Primary blast injury of the head: Numerical prediction and evaluation of protection”, *MASc Thesis*, University of Waterloo, Waterloo, Canada.

Lockhart PA, Cronin DS, Williams K, et al. (2011) “Investigation of head response to blast loading”, *The Journal of Trauma*, **70**(2):E29–36.

Lockhart PA, Cronin DS. (2014) “Helmet liner evaluation to mitigate head response from primary blast exposure”, *Comput Methods Biomech Biomed Engineering*, DOI:10.1080/10255842.2013.829460

Loth F, Yardimci M, Alperin N. (2001) “Hydrodynamic modeling of cerebrospinal fluid motion within the spinal cavity”, *J Biomechanical Engineering*, **123**:71-79.

Lovenheim P. (1974) “Strain tolerance of the Vv. Cerebri Sup. (bridging veins) calculated from head-on collision tests with cadavers”, *Z. Rechtsmedizin*, **75**(2):131-144.

LS-DYNA Keyword User’s Manual, Version R7.0, *Livermore Software Technology Corporation*, February 2013.

Lucca JJD, Chavko M, Dubrick MA, et al. (2012) “Blast-induced moderate neurotrauma (BINT) elicits early complement activation and tumor necrosis factor alpha (TNFa) release in a rat brain”, *J Neurological Sciences*, **318**:146-154.

Mahinda HAM, Murty OP. (2009) “Variability in thickness of human skull bones and sternum – An autopsy experience”, *Journal of Forensic Medicine and Toxicology*, **26**(2).

Makris A, Nerenberg J, Dionne JP, et al. (2000) “Reduction of Blast Induced Head Acceleration in the Field of Anti-Personnel Mine Clearance”, *Med-Eng Sys. Inc*, Ottawa, Canada.

Mao H. (2009) “Computational Analysis of In Vivo Brain Trauma”, *PhD Thesis*, Wayne State University, Detroit, USA.

Mao H, Guan F, Han X, Yang KH. (2011) “Strain based regional traumatic brain injury intensity in controlled cortical impact: A systematic numerical analysis”, *Journal of Neurotrauma*, **28**:2263–2276.

McGuire (online). “McGuire Army Navy”. Date accessed: Nov 11, 2014. <http://www.mcguirearmynavy.com/images/P/US-GI-PASGT-Kevlar-Ballistic-Helmet-OD.jpg>.

McKinley M, O’Loughlin V. (2008) “Human Anatomy, 2nd Edition”, New York, USA: McGraw-Hill. ISBN 978-0-07-296549-0.

MDheath (online). “Lobes of the Brain”. Date accessed: Nov 11, 2014. < http://www.md-health.com/Lobes-Of-The-Brain.html>.

Med-Eng, Personal communication via email, June 30, 2014.

Meyers MA. (1994) “Dynamic Behaviour of Materials”, New York, USA: John Wiley & Sons.

Monson (2003) “Axial mechanical properties of fresh human cerebral blood vessels”, *J Biomech Eng*, **125**(2):288-294.

Moore DF, Jérusalem A, Nyein M, et al. (2009) “Computational biology - modeling of primary blast effects on the central nervous system”, *NeuroImage*, **47**(2):T10–20.

Moore DF, Radovitzky RA, Shupenko L, et al. (2008) “Blast physics and central nervous system injury”, *Future Neurology*, **3**(3):243. DOI: 10.2217/14796708.3.3.243.

Moore KL, Dalley AF. (1999) “Clinically Orientated Anatomy, 4th Edition”, Baltimore: Lippincott Williams & Wilkins. ISBN 0-683-06141-0.

Moss WC, King MJ, Blackman EG. (2009) “Skull flexure from blast waves: a mechanism for brain injury with implications for helmet design”, *Physical Review Letters, LLNL-JRNL-412717.*

Nahum A, Smith R. (1976) “An experimental model for closed head impact”, *Proc 20th Stapp Car Crash Conf*, SAE 760825.

Nahum A, Smith R, Ward C. (1977) “Intracranial pressure dynamics during head impact”, *Stapp Car Crash Journal*, 1977, 339-366.

Needham, CE. (2010) “Blast Waves: Shock Wave and High Pressure Phenomena”, *Berlin Heidelberg: Springer*, 9-15. DOI: 10.1007/978-3-642-05288-0_3.

Needham, CE. (2009) “Airblast short course”, *Advanced Technologies and New Frontiers in Injury Biomechanics with Military and Aerospace Applications*, Arlington VA, August 2009.

Nelson, GE. (1982) “Fundamental Concepts of Biology”, New York: Wiley.

Nelson TJ, Wall DB, Stedje-Larsen ET, et al. (2006) “Predictors of mortality in close proximity blast injuries during Operation Iraqi Freedom”, *Journal of the American College of Surgeons*, **202**(3):418–22.

Newman JA, Shewchenko N, Welbourne E. (2000) “A proposed new biomechanical head injury assessment function - the maximum power index”, *Stapp Car Crash Journal*, **44**:215–47.

NIH (2012) “Brain Basics: Know Your Brain”, *National Institute of Neurological Disorders and Stroke*. Date accessed: Nov 11, 2014. < http://www.ninds.nih.gov/disorders/brain_basics/know_your_brain.htm>.

Nyein MK, Jason AM, Yu L, et al. (2010) “In silico investigation of intracranial blast mitigation with relevance to military traumatic brain injury”, *Proceedings of the National Academy of Sciences*, **107**(48):20703-20708.

Ono K, Kikuchi A, Nakamura M, et al. (1980) “Human head tolerance to sagittal impact: reliable estimation deduced from experimental head injury using subhuman primates and human cadaver skulls”, *Proceedings of 24th Stapp Car Crash Conference, SAE 801302*.

Ouellet S, Cronin D, Worswick M. (2006) “Compressive response of polymeric foams under quasi-static, medium and high strain rate conditions”, *Polymer Testing*, **25**:731-743.

Owens BD, Kragh JK, Wenke JC, et al. (2008) “Combat wounds in Operation Iraqi Freedom and Operation Enduring Freedom”, *J Trauma*, **62**(2):295-299.

Panzer MB, Bass CR, Myers BS. (2010) “Numerical study on the role of helmet protection in blast brain injury”, *Personal Armour Systems Symposium*, 2010.

Panzer MB, Bass CR, Rafaels K, et al. (2011a) “Primary blast survival and injury risk assessment for repeated blast exposures”, *J Trauma Acute Care Surg*, **72**(2):454-66.

Panzer MB, Myers BS, Bass CR. (2011b) “Mesh considerations for finite element blast modeling in biomechanics”, *Computer Methods in Biomechanics and Biomedical Engineering*. DOI:10.1080/10255842.2011.629615

Panzer MB, Myers BS, Capehart BP et al. (2012) “Development of a Finite Element Model for Blast Brain Injury and the Effects of CSF Cavitation”, *Annals of Biomedical Engineering*, **40**(7):1530–1544.

Parsons FG. (1929) “The Thickness of the Living Scalp”, *Journal of Anatomy*, **63**(4):427-429.

Pervin F, Chen WW. (2009) “Dynamic mechanical response of bovine gray matter and white matter brain tissues under compression”, *J Biomechanics*, **42**:731-735.

Pervin F, Chen WW. (2011) “Effect of inter-species, gender, and breeding on the mechanical behavior of brain tissue”, *Neuroimage*, **54**:S98-S102.

Pouyssegur P. (online) “Stele of Vultures”, *Department of Near Eastern Antiquities: Mesopotamia*, Louvre. Date accessed: Nov 11, 2014. <http://www.louvre.fr/en/oeuvre-notices/stele-vultures>.

Prange MT, Margulies SS. (2002) “Regional, directional, and age-dependent properties of the brain undergoing large deformation”, *Transactions of the ASME*, 124(April), 2002.

Prevost TP, Jin G, De Moya MA, et al. (2011) “Dynamic mechanical response of brain tissue in indentation in vivo, in situ, and in vitro”, *Acta Biomaterialia*, **7**(12):4090-4101.

Rafaels KA, Bass CR, Salzar RS, et al. (2011) “Survival risk assessment for primary blast exposures to the head”, *Journal of Neurotrauma*, **28**:2319-2328.

Rafaels KA, Bass CR, Panzer MB, et al. (2012) “Brain injury risk from primary blast”, *Journal of Trauma*, **73**(4):895-901.

Rashid B, Destrade M, Gilchrist MD. (2013) “Influence of preservation temperature on the measured mechanical properties of brain tissue”, *Journal of Biomechanics*, **46**(7):1276-1281.

Roache PJ. (1998) “Verification and validation in computational science and engineering”, Albuquerque NM: Hermosa Publishers. ISBN 0-913478-08-3.

Roberts JC, Harrigan TP, Ward EE, et al. (2012) “Human head-neck computational model for assessing blast injury”, *Journal of Biomechanics*, **45**:2899–2906.

Rosen ME. (2000) “Osteopathy in the cranial field”. Date accessed: Nov 11, 2014. <http://www.osteodoc.com/sutherland.htm>.

Ruan JS. (1994) “Impact biomechanics of head injury by mathematical modeling”, *PhD dissertation*, Wayne State University.

Ruan JS, Prasad P. (1996) “Study of biodynamic characteristics of the human head”, *Proceedings of the International IRCOBI Conference on the Biomechanics of Impacts*, 63-74.

Ruan JS, Prasad P. (2001) “The Effects of Skull Thickness Variations on Human Head Dynamic Impact Responses”, *Stapp Car Crash Journal*, **45**:395-414.

Sack I, Beierbach B, Wuerfel J, et al. (2009) “The impact of aging and gender on brain viscoelasticity”, *Neuroimage*, **46**:652-657.

Säljö A, Svensson B, Mayorga M. (2009) “Low-Level blasts raise intracranial pressure and impair cognitive function in rats”, *Journal of Neurotrauma*, **26**:1345–1352.

Säljö A, Arrhen F, Bolouri H. (2008) “Neuropathology and pressure in the pig brain resulting from low-impulse noise exposure”, *Journal of Neurotrauma*, **25**:1397–1406.

Saikat P. (2008) “Explicit Finite Element Modeling of Joint Mechanics, Figure 2.4” Ann Arbor MI: ProQuest.

Sayed T, Mota A, Fraternali F, et al. (2008) “Biomechanics of traumatic brain injury”, *Computer methods in applied mechanics and engineering*, **197**(51-52):4692-4701.

Sellier KG, Kneubuehl BP (1994). “Wound Ballistics and the Scientific Background”, Amsterdam, The Netherlands: Elsevier.

SFIP (online). “Types of Spray Foam Insulation”, *Spray Foam Insulation Pheonix*, Date accessed: Nov 11, 2014. <http://sprayfoaminsulationphoenix.net/types-of-spray-foam-insulation>.

Shafieian M, Bao J, Darvish K. (2011) “Mechanical Properties of Brain Tissue in Strain Rates of Blast Injury”, *37th Ann IEEE Bioengineering Conf*, Philadelphia, USA, 2011.

Shridharani JK, Wood GW, Panzer MB et al. (2012) “Porcine head response to blast”, *Frontiers in Neurology*, **3**(May):1-12. DOI: 10.3389/fneur.2012.00070.

Smith PD, Hetherington JG. (1994) “Blast and Ballistic Loading of Structures”, Oxford, UK: Butterworth-Heineman.

Singh D, Lockhart PA, Haladuick TN, Cronin DS. (2011) “Comparison of detailed sagittal and transverse finite element head models to evaluate blast load response”, *IASTED Biomech*, Pittsburgh, PA, November 2011.

Singh D, Cronin DS, Lockhart PA, et al. (2012) “Evaluation of head response to blast using sagittal and transverse finite element head models”, *Proc. PASS*, Nuremberg, Germany.

Singh D, Cronin DS, Haladuick TH. (2013) “Head and brain response to blast using sagittal and transverse finite element models”, *Int J Num Meth Biomed Eng*, **30**(4):470-489.

Singh D, Cronin DS. (2014) “Investigation of cavitation using a modified Hopkinson apparatus”, *Proceedings of SEM*, Greenville, NC, USA, June 2014.

Sista B, Vemaganti K. (2011) “Modeling and Simulation of the High Strain-Rate Response of Brain Tissue for Traumatic Brain Injury Applications”, *Ohio State University Injury Biomechanics Symposium*.

Souli M, Mahmadi K, Aquelet N. (2004) “ALE and Fluid Structure Interaction”, *Materials Science Forum*, **465**:143-150.

Spitzer V, Ackerman MJ, Scherzinger AL, et al. (1996) “The Visible Human Male: A Technical Report”, *Journal of the American Medical Informatics Association*, **3**(2).

Stuhmiller JH, Ho KHH, vander Vorst MJ, et al. (1996) “A model of blast overpressure injury to the lung”, *Biomechanics*, **26**(2).

Subhash G, Hong Y, Canchi S, et al. (2013) “Cavitation induced structural and neoronal damage in brain tissue: relevance to TBI”, *2013 TMS Annual Meeting & Exhibition*.

Svetlav SI, Prima V, Glushakova O, et al. (2012) “Neuro-glial and systemic mechanisms of pathological responses in rat models of primary blast overpressure compared to ‘composite’ blast”, *Frontiers in Neurology*, **3**(February):1-12.

Takhounts EG, Ridella SA, Hasija V, et al. (2008) “Investigation of traumatic brain injuries using the next generation of simulated injury monitor (SIMon) finite element head model”, *Stapp Car Crash Journal*, ***52***(Nov):1-31.

Tan P, Lee B, Tsangalis C. (2009) “FEA modeling prediction of the transmitted overpressure and particle acceleration within a frame subjected to shock tube blast loadings”, *18th World IMACS*, Cairns, Australia, 1657-1663.

Tanielian T, Jaycox LH. (2008) “Invisible wound of war: Psychological and cognitive injuries, their consequences, and services to assist recovery”, Los Angeles, CA, USA: RAND Corporation.

Taylor Z, Miller K. (2004) “Reassessment of brain elasticity for analysis of biomechanisms of hydrocephalus”, *J Biomechanics*, **37**:1263-1269.

Taylor PA, Ford CC. (2009) “Simulation of blast-induced early-time intracranial wave physics leading to traumatic brain injury”, *Journal of Biomechanical Engineering*, **131**(6).

Terrio H, Brenner LA, Ivins BJ, et al. (2009) “Traumatic brain injury screening: preliminary findings in a US Army Brigade Combat Team”, *J Head Trauma Rehabil*, **24**(1):14-23.

Thom, C. (2009) “Soft materials under air blast loading and their effect on primary blast injury”, *MASc. Thesis*, University of Waterloo.

Thunert C, “CORA Release 3.6 User’s Manual”, <http://www.pdb-org.com/de/information/18-cora-download.html>.

Tomkins R. (2014). “U.S. orders more enhanced combat helmets from 3M company”, *United Press International*, Date accessed: Nov 11, 2014. <http://www.upi.com/Business_News/Security-Industry/2014/10/16/US-orders-more-enhanced-combat-helmets-from-3M-company/4361413471492/>.

Tsaklis PV. (2010) “Presentation of acoustic waves propagation and their effects through human body tissues”, *Human Movement*, **11**(1):91-95.

TWCenter (online). “Various Arms & Armor – actual images”. Date accessed: Nov. 11, 2014. <http://img510.imageshack.us/img510/3247/bascinetwithvisoritalia.jpg>.

Valiyaveettil M, Alamneh Y, Oguntayo S, et al. (2012) “Regional specific alterations in brain acetylcholinesterase activity after repeated blast exposure in mice”, *Neuroscience Letters*, **506**:141-145.

van Dommelen JAW, van der Sande TPJ, Hrapko M, et al. (2010) “Mechanical properties of brain tissue by indentation: interregional variation”, *J Mech Behaviour of Biomed Materials*, **2**:158-166.

van Sligtenhorst C, Cronin DS, Brodland GW. (2006) “High strain rate compressive properties of bovine muscle tissue determined using a split Hopkinson bar apparatus”, *Journal of Biomechanics*, **39**(10):1852-1858.

VHP (online). “Visible Human Project” *US Nat. Library of Medicine, NIH*. Date accessed: Nov 14, 2014. <http://www.nlm.nih.gov/research/visible/visible_human.html>.

Vogel E, Villacorta J, Bass CR, et al. (2014) “Primary blast injury erases long term potentiation in rat brain organotypic hippocampal slices”, *IRCOBI Conference 2014*, IRC-14-89.

Ward C, Chan M, Nahum A. (1980) “Intracranial Pressure - A Brain Injury Criterion”, *SAE Technical Paper 801304*. DOI: 10.4271/801304.

Wardlaw A, Goeller J. (2010) “Cavitation as a possible traumatic brain injury (TBI) damage mechanism” *IFMBE Proceedings*, **32**:34-37.

Wightman JM, Gladish SL. (2001) “Explosions and blast injuries”, *Annals or Emergency Medicine*, **37**(6):664-678.

Wojcik BE, Stein CR, Bagg K, et al. (2010) “Traumatic brain injury hospitalizations of US Army soldiers deployed to Afghanistan and Iraq”, *Am J Prev Med*, **38**(1):S108-S116.

Wollaston RB. (Online) “Pre Admission Biology - The Skeletal System, Chapter 6”. Date Accessed: Nov. 11, 2014. < http://www.dmacc.edu/instructors/rbwollaston/Chapter_6_Skeletal_System.htm>.

Yelverton, JT. (1993) “Blast overpressure studies with animals and man: Final report – Biological response to complex blast waves”, *U.S. Army Medical Research and Development Command*, Fort Detrick.

Zhang L, Yang KH, King AI. (2001) “Comparison of brain responses between frontal and lateral impacts by finite element modeling”, *Journal of Neurotrauma*, **18**(1):21-30.

Zhang L, Yang KH, King AI. (2004) “A Proposed Injury Threshold for Mild Traumatic Brain Injury”, *Journal of Biomechanical Engineering*, **126**(2):226.

Zhang J, Yoganandan N, Pintar FA, et al. (2011a) “Effects of tissue preservation temperature on high strain rate material properties of brain”, *J Biomechanics*, **44**:391-396.

Zhang J, Green MA, Sinkus R, et al. (2011b) “Viscoelastic properties of human cerebellum using magnetic resonance elastography”, *J Biomechanics*, **44**:1909-1913.

Zhou C, Khalil TB, King AI, (1995) “A new model comparing responses of the homogeneous and inhomogenous human brain”, *Proceedings of the 39th Stapp Car Crash Conference*, SAE Paper 952714.

Zhu F, Jin X, Guan F, et al. (2010a) “Identifying the properties of ultra-soft materials using a new methodology of combined specimen-specific finite element model and optimization techniques”, *Materials & Design*, **31**(10):4704–4712.

Zhu F, Chou CC, Yang KH, et al. (2013a) “Some considerations on the threshold and inter-species scaling law for primary blast-induced traumatic brain injury: A semi-analytical approach”, *J Mech Med Biol*, **13**(4).

Zuckerman S. (1940) “Experimental study of blast injuries to the lungs” *The Lancet*, **236**(6104):219-224.

Appendix A: Mesh Convergence Study

A mesh convergence study was previously done by Lockhart [Lockhart 2010] on the sagittal model using head acceleration as the metric, and it was concluded that 1 mm mesh size is necessary to achieve good results. A similar convergence analysis was undertaken in the current work using intracranial pressure as the response metric. The sagittal model geometry was used to generate three meshes, with characteristic element lengths of 2 mm, 1 mm, and 0.5 mm. The intracranial pressure predictions of each mesh was compared using the Grid Convergence Index method to determine an appropriate mesh size. For this convergence study, the blast load case of 5 kg C4 at 4 m standoff was chosen to compare the meshes.

The 5% volume peak intracranial pressure of the models was extracted for the three difference element sizes to be used as the convergence metric (Table A.1). In order words, the maximum intracranial pressure that at least 5% of the brain tissue volume was exposed to. These results are plotted in Figure A.1, which demonstrates a clear exponential relationship between element size and model response, with the difference between the 0.5 mm and 1 mm meshes to be significantly less than the difference between the 1 mm and the 2 mm (Figure A.1).

Table A.1: Mesh convergence study results

Element Size	Number of Elements	5% Maximum ICP
2 mm	12 209	149000
1 mm	48 060	174500
0.5 mm	192 240	175500

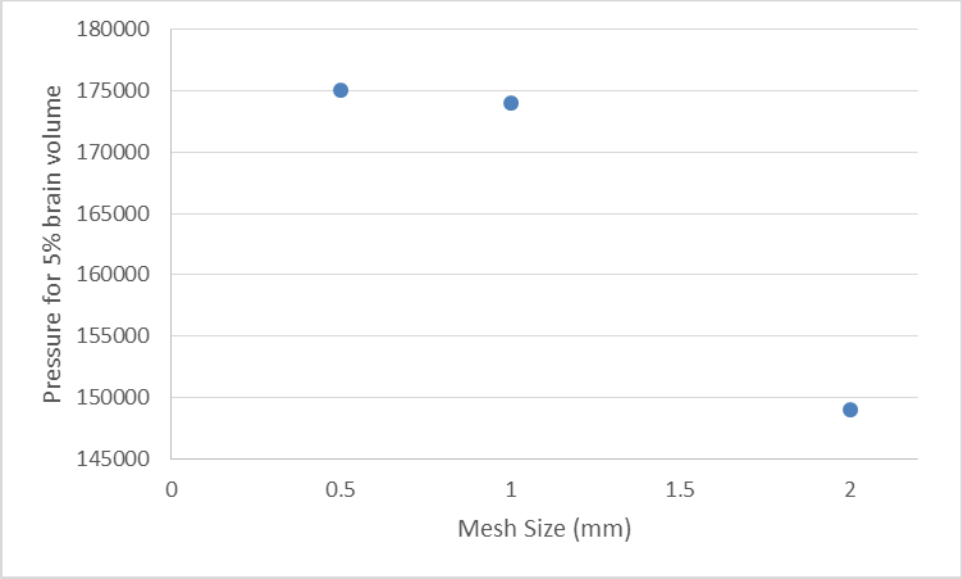

Figure A.1: Plot of mesh convergence study results

The results of the mesh convergence analysis is shown in Table A.2. This is using a factor of safety of 1.25, which is recommended for three mesh studies, as discussed in Section 6.3.

Table A.2: Grid Convergence Index calculations for mesh convergence study

Grid Refinement Ratio, *r*	2
Order of Convergence, *p*	4.672
Factor of Safety, F_s	1.25
$\boldsymbol{GCI_{12}}$	-0.0002907
$\boldsymbol{GCI_{23}}$	-0.007456
$\boldsymbol{r^p GCI_{12}}$	-0.007413

Looking at the results of the grid convergence indexes, it is clear that the values of GCI_{23} and r^pGCI_{12} are very close, thereby satisfying the asymptotic regime condition for mesh convergence. Therefore, a mesh size of 1 mm is sufficient in these models to predict intracranial pressures. To test this further, a pressure trace was taken at an element in the brain material in the anterior portion

of the brain near the forehead, and compared for each of the three mesh sizes (Figure A.2). It is clear that the pressures are significantly underpredicted in the 2 mm mesh, while the 1 mm and 0.5 mm meshes report almost identical curves.

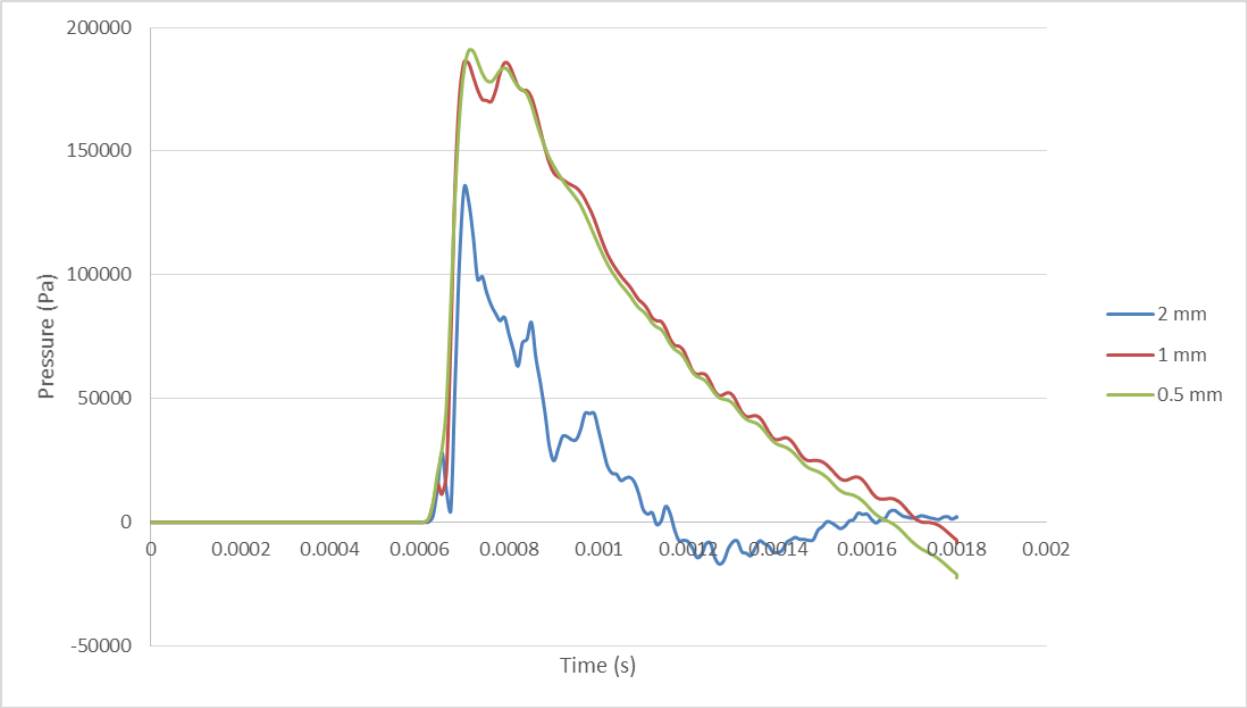

Figure A.2: Comparison of intracranial pressure traces for frontal region of brain at three mesh sizes

Appendix B: Comparison of Hexahedral and Tetrahedral Mesh

Several finite element blast head models in the literature generate three dimensional geometries using tetrahedral elements [El Sayed et al. 2008, Moore et al. 2009, Grujicic 2010b, Roberts et al. 2012]. One of great benefits of tetrahedral elements is that they can be used to create highly complex shapes very easily using meshing software, in contrast to hexahedral meshes which require manual inputs and careful planning of geometries. However, single integration point tetrahedral elements are well known to not be suited for applications with large hydrostatic components of loading [Hallquist 2006]. This is because they can exhibit hydrostatic locking, where the elements can achieve very large hydrostatic pressures without undergoing deformation. To investigate the effects of using single integration point tetrahedral elements for a blast head model, the sagittal model was converted to a tetrahedral mesh and the model response for intracranial pressure was compared with the hexahedral element mesh.

The generated tetrahedral element mesh used four-noded constant stress tetrahedral elements, by converting each hexahedral element in the original mesh to five tetrahedral elements. This maintained the characteristic length of the elements to be 1 mm, consistent with the original element size (Figure B.1).

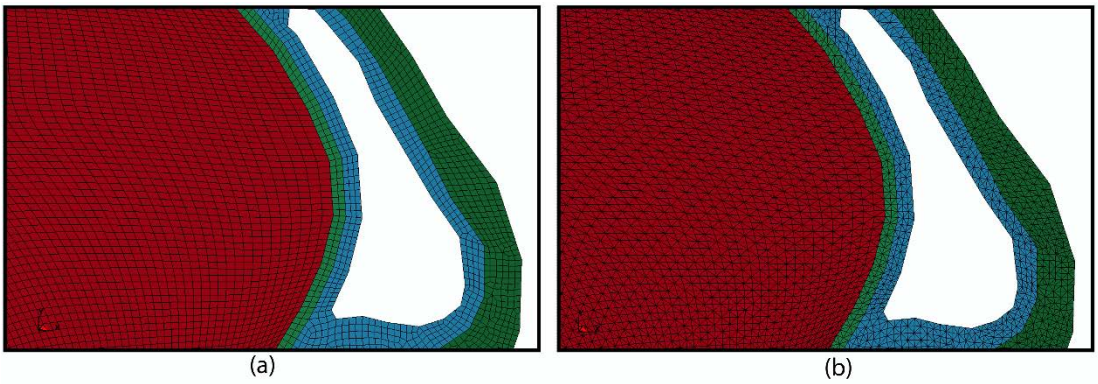

Figure B.1: Comparison of (a) hexahedral and (b) tetrahedral meshes

The original hexahedral as well as the tetrahedral meshes were run for the 5 kg C4 at 4 m standoff distance, using the method outlined in Section 7.2. The peak pressures at four corresponding locations at the frontal, parietal, and occipital locations were compared (Figure B.2). The tetrahedral elements reported peak intracranial pressures approximately 300% greater than the hexahedral mesh for all locations. Additionally, the tetrahedral mesh reported large amounts of pressure variation for adjacent elements, a characteristic not present in the hexahedral mesh. This is demonstrated in Figure B.3, which compares the pressure histories of adjacent elements at the same location of the brain between the hexahedral and tetrahedral meshes. The tetrahedral mesh reports pressures varying up to 250% in directly adjacent elements, whereas the hexahedral mesh reports very small variation, which is attributed to wave dispersion that would be expected according to the physics.

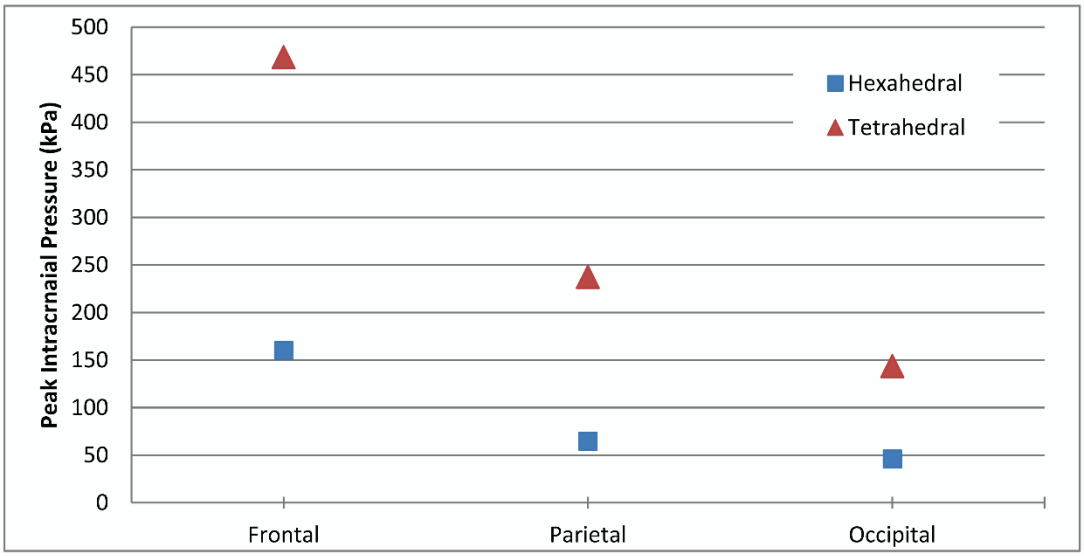

Figure B.2: Pressure comparison between hexahedral and tetrahedral elements

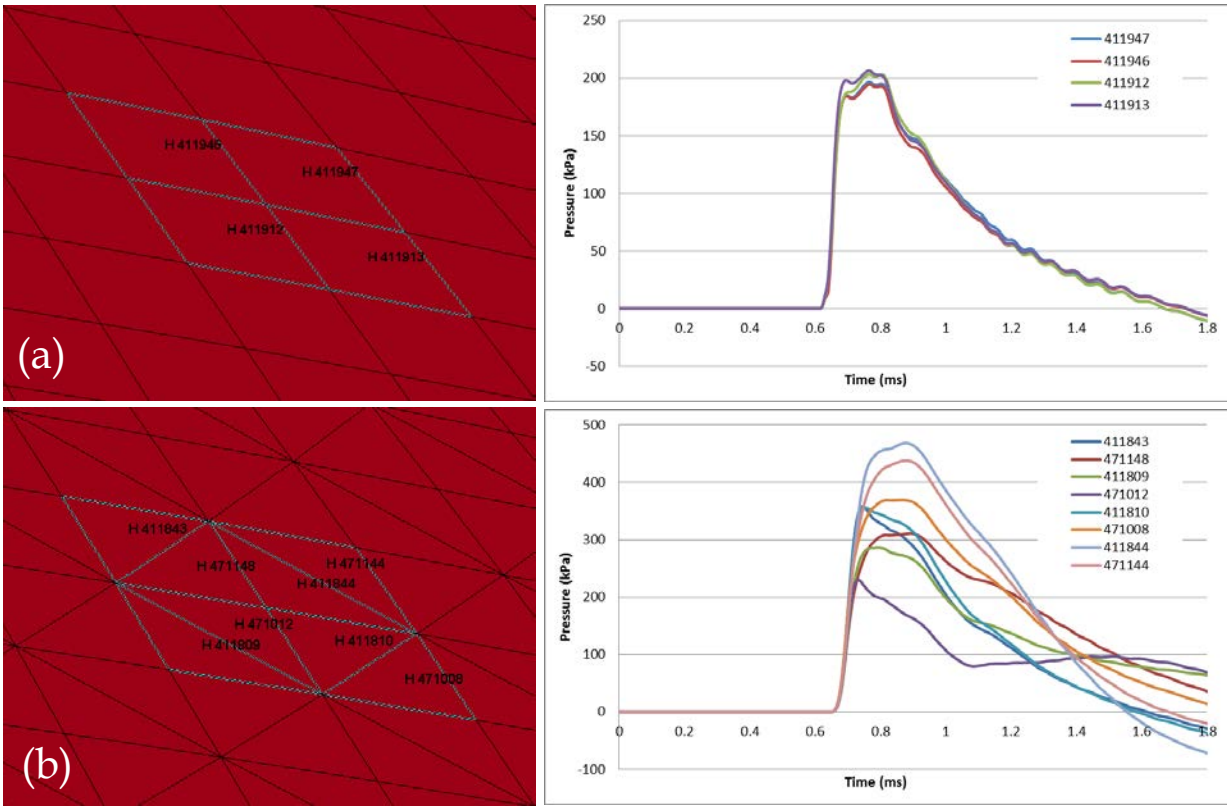

Figure B.3: Pressure variation for adjacent elements for the (a) hexahedral and (b) tetrahedral meshes

The significantly greater predicted intracranial pressures and the large degree of local variability in the tetrahedral mesh indicates that hydrostatic locking is occurring in these elements. Hydrostatic locking is a well-known phenomenon that can affect tetrahedral elements in applications with large hydrostatic components of loading, and the results of this comparison suggests that blast simulations fall into this category. Therefore, finite element blast models should avoid using tetrahedral elements which can result in misleading pressures. This emphasizes the importance of using hexahedral elements in blast simulations.

Appendix C: Blunt Impact Validation Study

It is often beneficial to use a wide variety of validation cases in different regimes of loading, to understand the capabilities and robustness of a numerical model. Consequently, the sagittal model was investigated in blunt impact loading, to match the experimental conditions in cadaver impact tests conducted by Nahum et al. [Nahum et al. 1977]. A rigid cylindrical blunt impact was investigated, with 5.23 kg mass at a velocity of 4.21 m/s, corresponding to one of the experiments (Figure C.1). The input force duration for this impact was approximately 10 ms, although the rise time for the peak load was about 4 ms, as opposed to blast loads which have sub 1 ms rise times. The experimental peak head acceleration reported by Nahum et al. was 1280 m/s^2, while the sagittal model reported a corresponding peak value of 1340 m/s^2, using a 300 kHz Butterworth filter to match the experimental methods [Nahum 1976]. Although the peak head acceleration demonstrated good agreement with the experimental data, the intracranial pressures were overpredicted by the model due to the focal nature of the impact and the geometry of the slice model, which resulted in higher compliance for aggressive localized blunt impact loads. However, since blast loads are distributed relatively evenly across the head, with smaller deformations of the tissues this was judged to be acceptable.

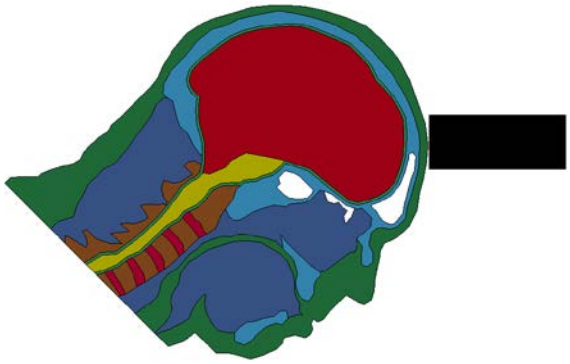

Figure C.1: Blunt impact validation with sagittal model

Appendix D: Intracranial Pressure Comparison with Experimental Data

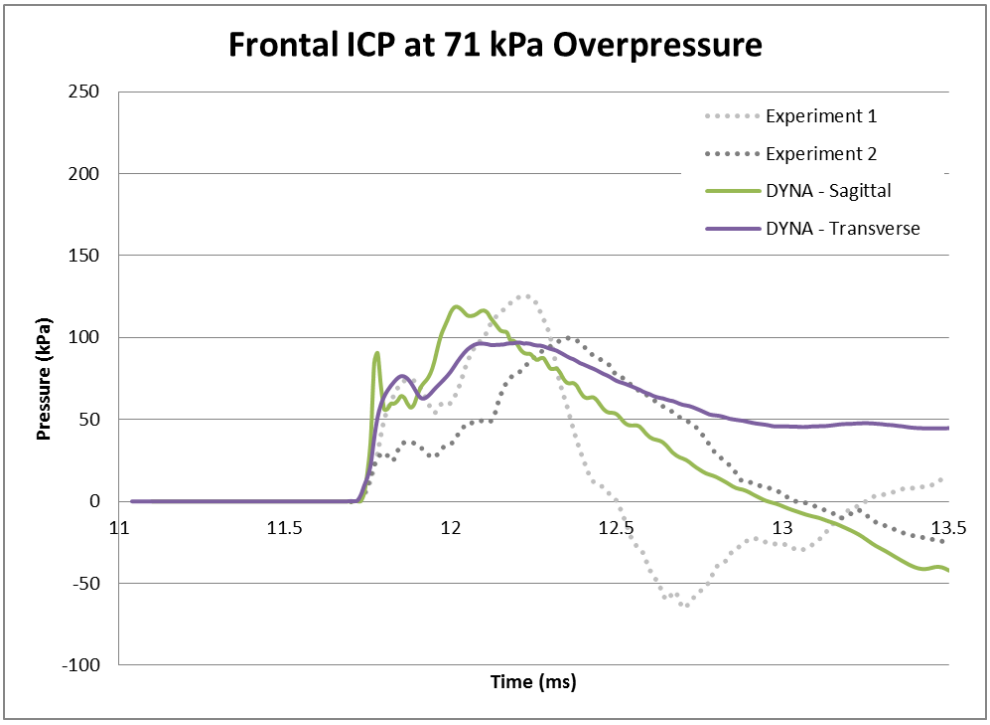

Figure C.1: Model ICP validation for frontal at 71 kPa overpressure

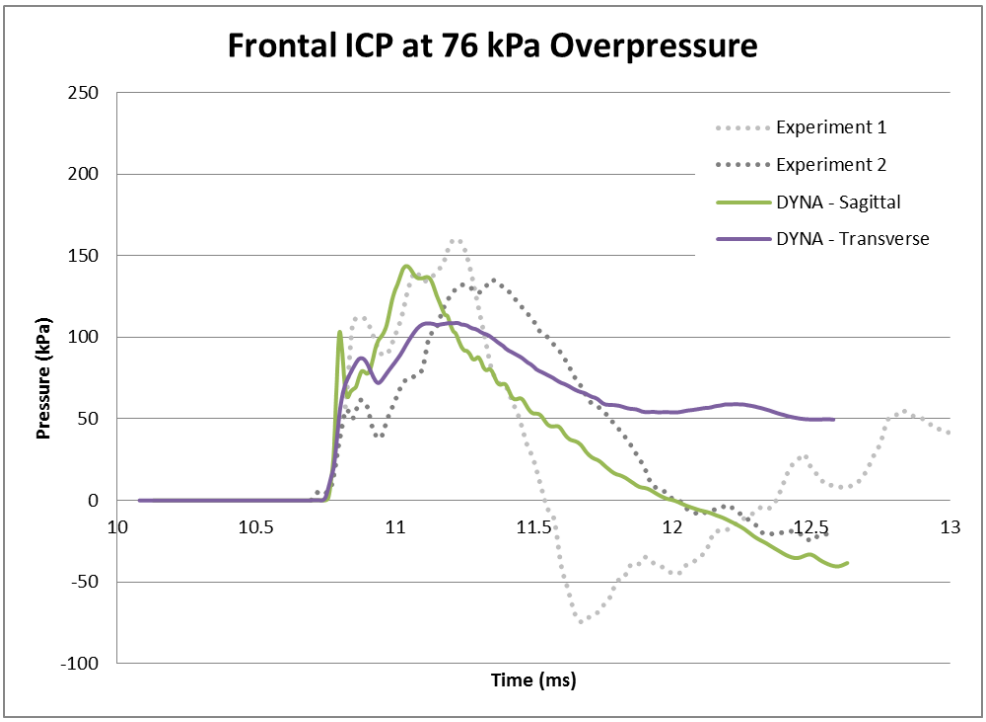

Figure C.2: Model ICP validation for frontal at 76 kPa overpressure

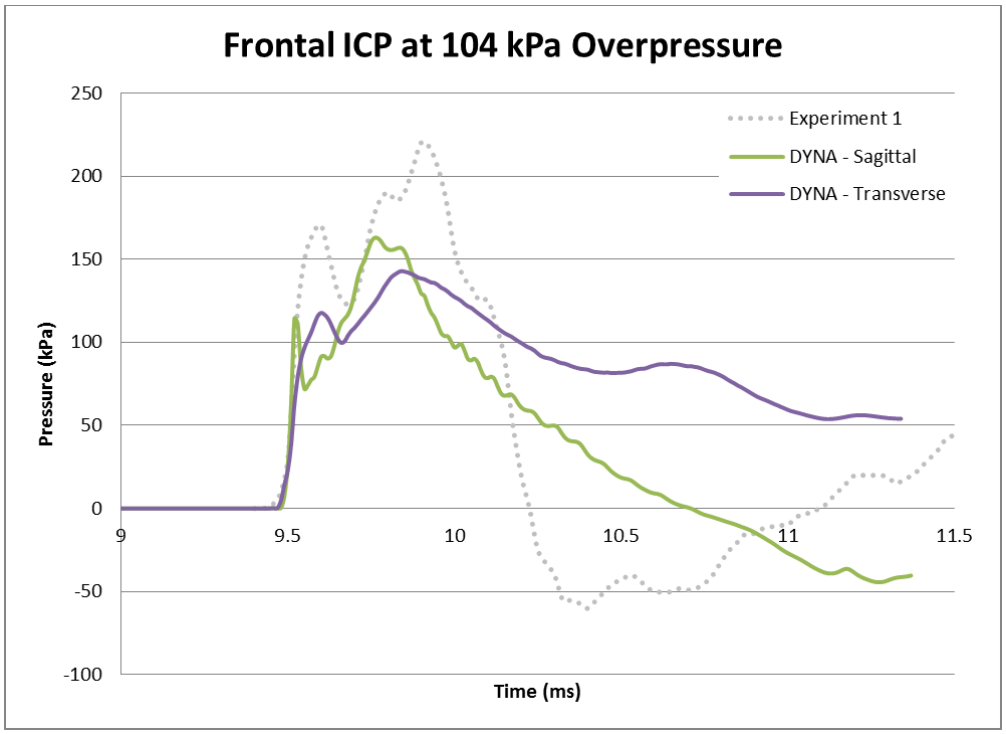

Figure C.3: Model ICP validation for frontal at 104 kPa overpressure

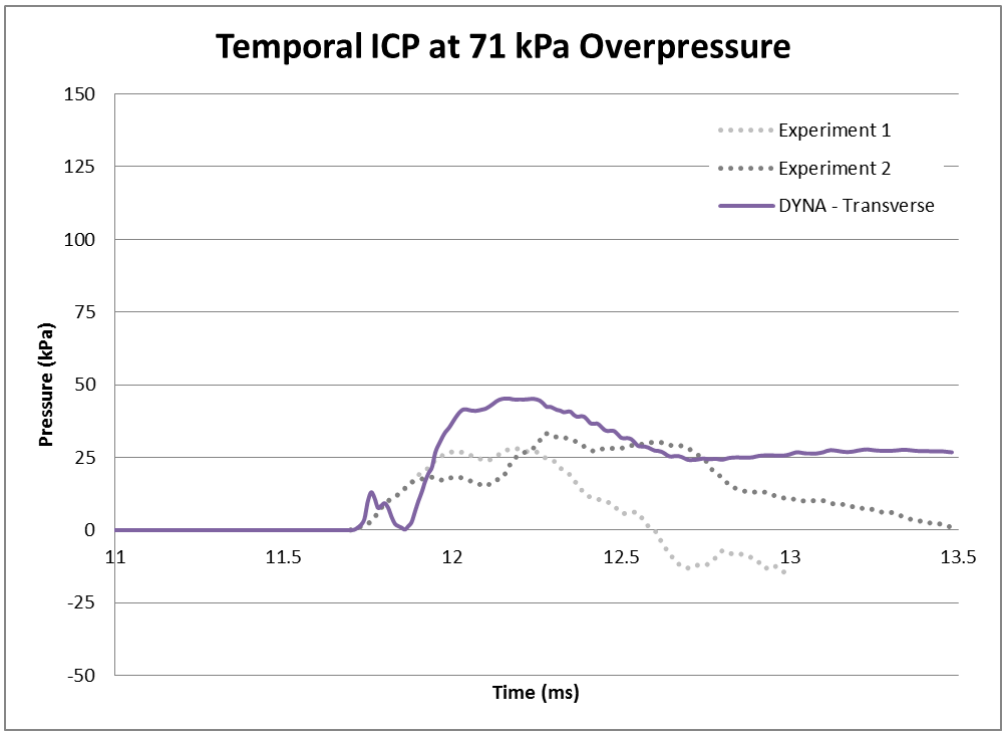

Figure C.4: Model ICP validation for temporal at 71 kPa overpressure

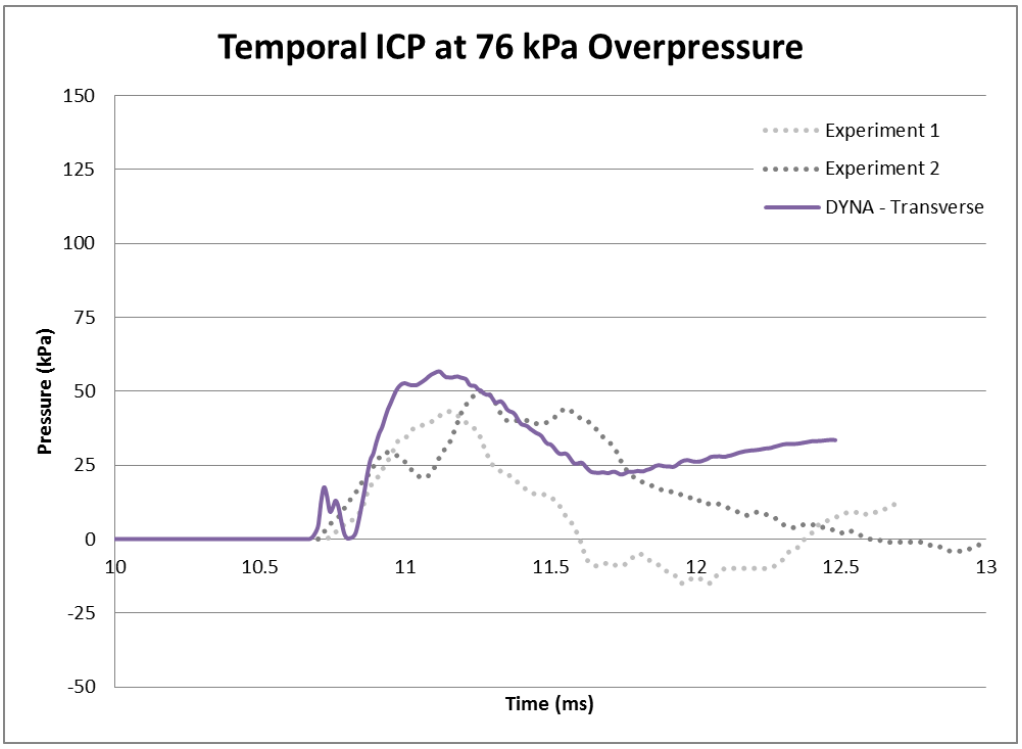

Figure C.5: Model ICP validation for temporal at 76 kPa overpressure

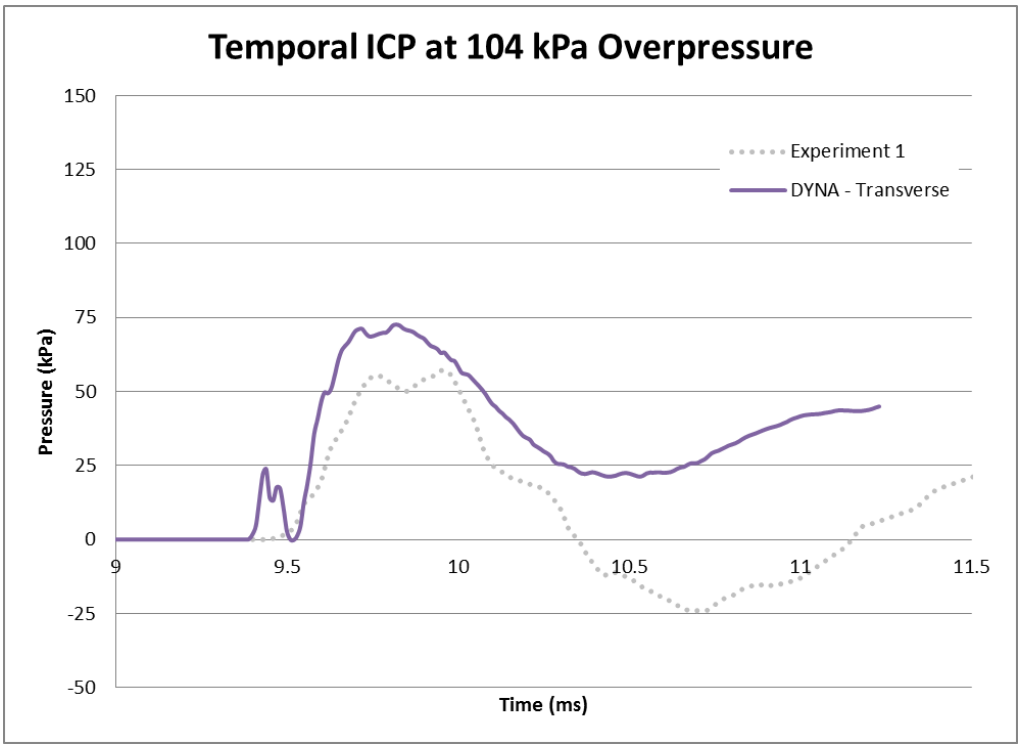

Figure C.6: Model ICP validation for temporal at 104 kPa overpressure

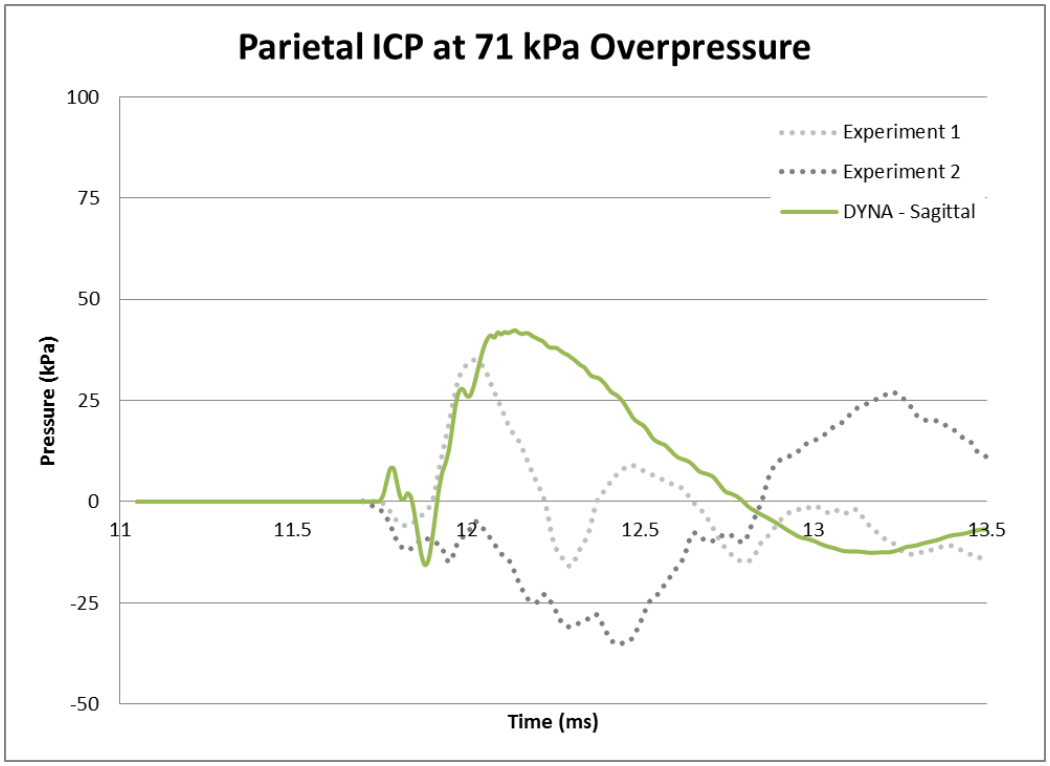

Figure C.7: Model ICP validation for parietal at 71 kPa overpressure

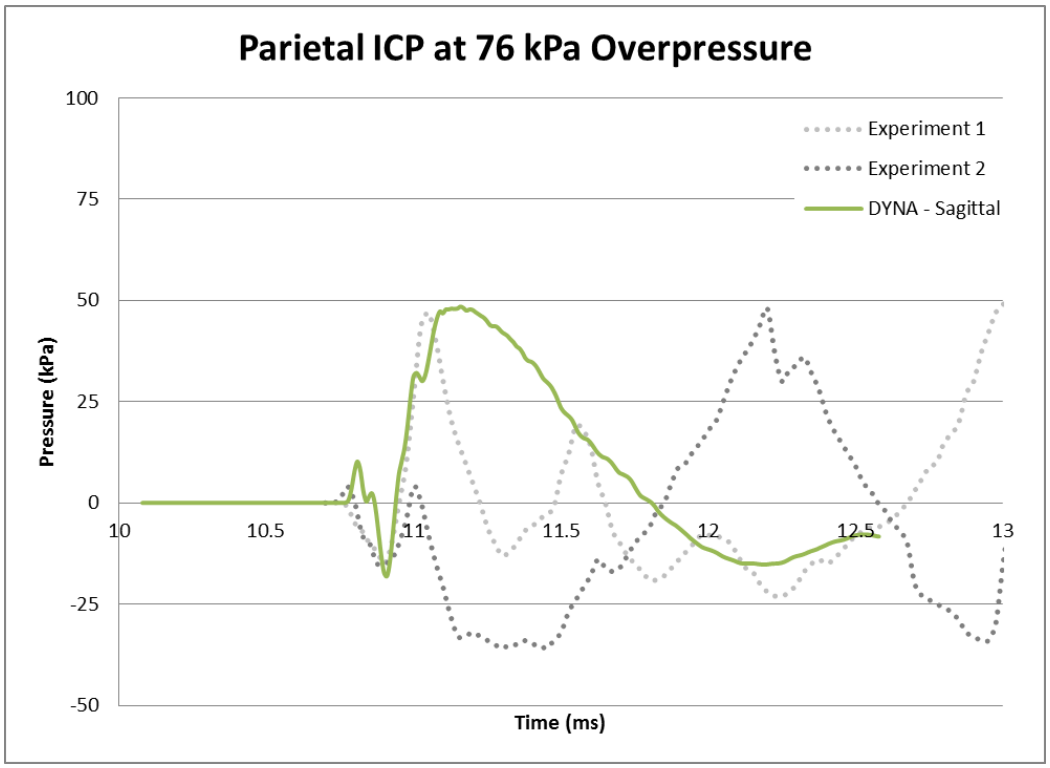

Figure C.8: Model ICP validation for parietal at 76 kPa overpressure

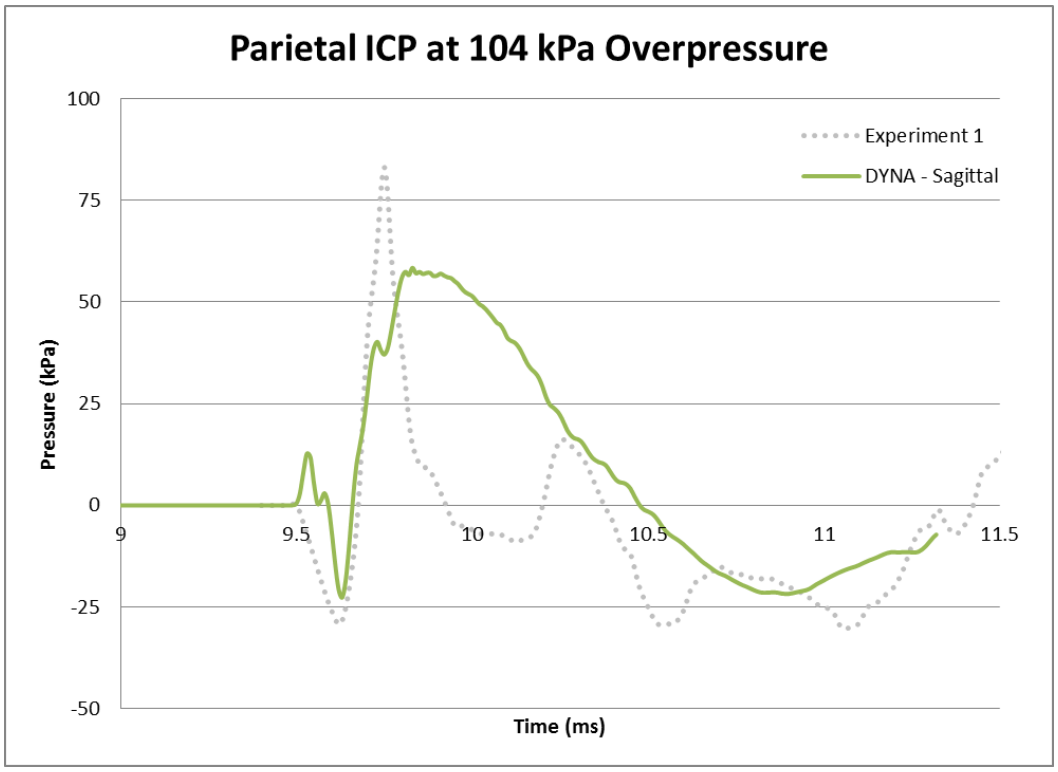

Figure C.9: Model ICP validation for parietal at 104 kPa overpressure

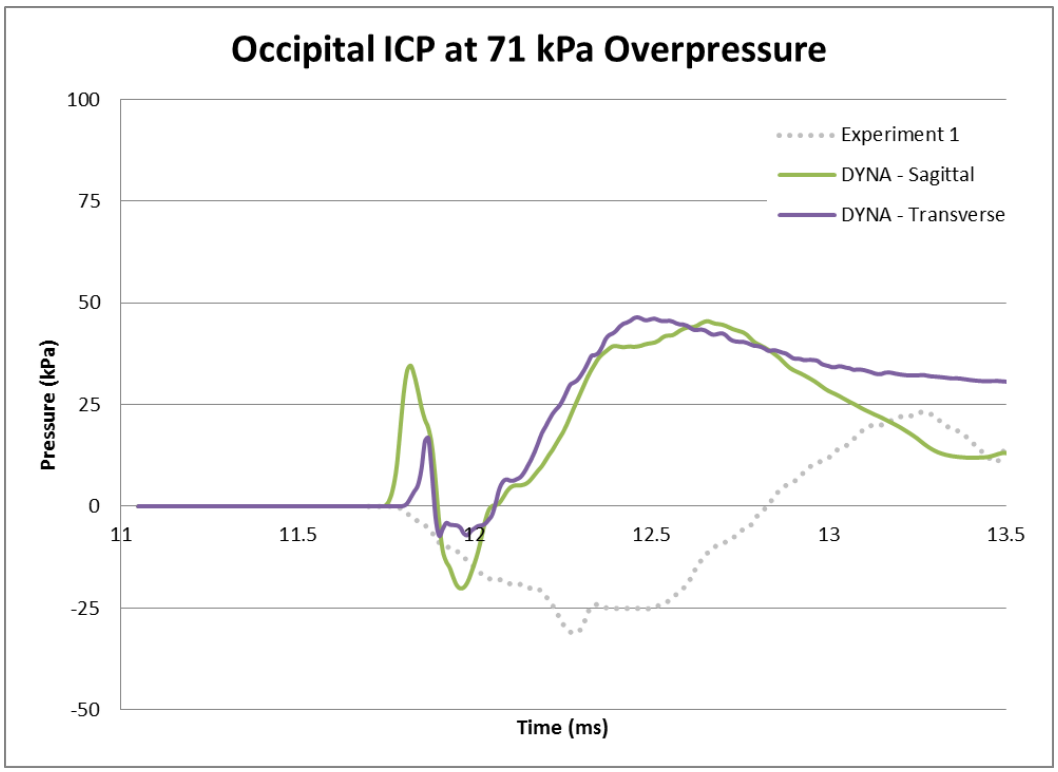

Figure C.10: Model ICP validation for occipital at 71 kPa overpressure

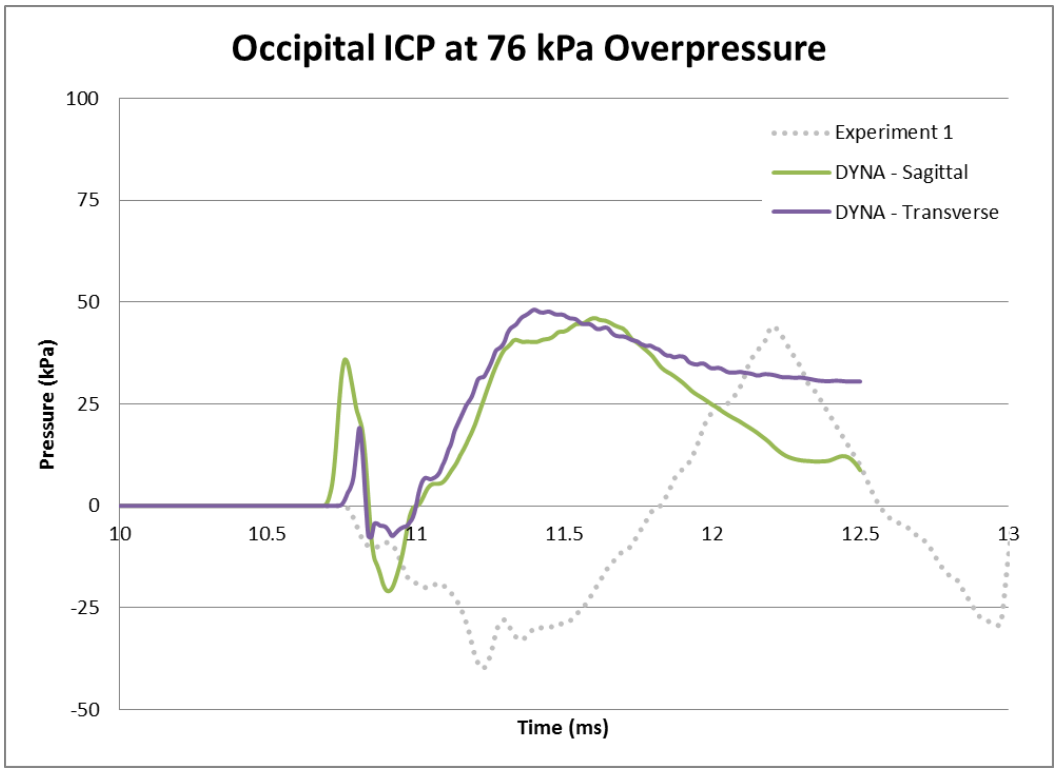

Figure C.11: Model ICP validation for occipital at 76 kPa overpressure

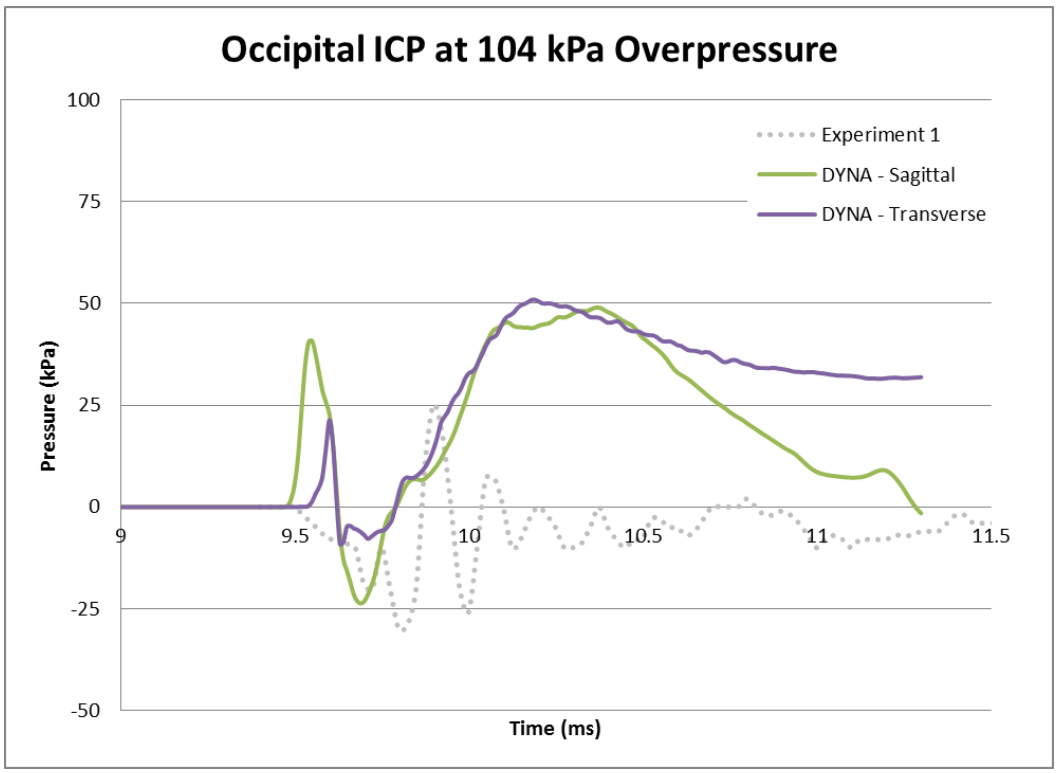

Figure C.12: Model ICP validation for occipital at 104 kPa overpressure

Appendix E: CORA Global Parameters for ICP Validation

```
################################################################################
#
#   CORA v3.0.0
#
################################################################################
#
################################################################################
#
#   Global Parameters
#
################################################################################
BEGIN GLOBAL_PARAMETERS
  DES_MOD             Validation of UW Blast FE models              ; Header of the evaluation
  DES_GLO             Comparison of UW sagittal and transverse with Bir (2011) cadaver tests
#
# Global settings to define the interval of evaluation
  A_THRES             0.5                 ; Threshold to set the start of the interval of evaluation [0,...,1]
  B_THRES             1                   ; Threshold to set the end of the interval of evaluation [0,...,1]
  A_EVAL              0.1                 ; Extension of the interval of evaluation [0,...,1]
  B_DELTA_END         0.9                 ; Additional parameter to shorten the interval of evaluation (width
of the corridor: A_DELTA_END*Y_NORM) 0 = disabled
  T_MIN/T_MAX         automatic     automatic               ; Manually defined start (time) and end (time) of
the interval of evaluation (automatic = calculated for each channel)
#
# Global settings of the corridor method
  K                   1                   ; Transition between ratings of 1 and 0 of the corridor method [-]
(1 = linear, 2 = quadratic ...)
  G_1                 0                   ; Weighting factor of the corridor method [-]
  a_0/b_0             0.001    0.002      ; Width of the inner and outer corridor [-]
  a_sigma/b_sigma     1        2          ; Multiples of the standard deviation to widen the inner and outer
corridor [-]
# Global settings of the cross correlation method
  D_MIN               0.025                ; delta_min as share of the interval of evaluation [0,...,1]
  D_MAX               0.25                ; delta_max as share of the interval of evaluation [0,...,1]
  INT_MIN             0.80                ; Minimum overlap of the interval [0,...,1]
  K_V                 1                   ; Transition between ratings of 1 and 0 of the progression rating
[-] (1 = linear, 2 = quadratic ...)
  K_G                 1                   ; Transition between ratings of 1 and 0 of the size rating [-] (1 =
linear, 2 = quadratic ...)
  K_P                 1                   ; Transition between ratings of 1 and 0 of the phase shift rating
[-] (1 = linear, 2 = quadratic ...)
  G_V                 0.34                ; Weighting factors of the progression rating [-]
  G_G                 0.33                ; Weighting factors of the size rating [-]
  G_P                 0.33                ; Weighting factors of the phase shift rating [-]
  G_2                 1                   ; Weighting factors of the cross correlation method [-]
# Normalisation of the weighting factors
  WF_NORM             YES                 ; Normalisation of the weighting factors [YES/NO]?
# Signal settings
  ISONAME_1-2/11-12   YES YES             ; Consideration of the position 1/2 (test object, seating position)
and 11/12 (fine location 3 - dummy) of the ISO code [YES/NO]
  MIN_NORM            0.00                ; Threshold (as fraction of the global absolute maximum amplitude)
to start special treatment of secondary axis [0,...,1]
  Y_NORM              extremum            ; Type of calculation of Y_NORM (extremum or value)
#
# Format settings of the html report
  OUTPUT_FORMAT       LSPOST           ; Export format (LSPOST, PAMVIEW or Hypergraph)
  OUTPUT_UNIT         m-Kg-s              ; Unit system
  OUTPUT_g            YES                 ; Use [g] [YES/NO]?
# Layout of the html report
  FONT_SMALL          12                  ; Size of the small font
  FONT_LARGE          14                  ; Size of the large font
  PreT_LC/PostT_LC    -1  -1              ; Expansion of the plotted interval of the curves (-1: complete
curve)
END GLOBAL_PARAMETERS
#
```